

AD-755 840

A STUDY OF WIND TUNNEL SIMULATION OF HIGH
ALTITUDE ROCKET PLUMES

James Stark Draper, et al

Aerodyne Research, Incorporated

Prepared for:

Air Force Rocket Propulsion Laboratory

February 1973

DISTRIBUTED BY:

NTIS

National Technical Information Service
U. S. DEPARTMENT OF COMMERCE
5285 Port Royal Road, Springfield Va. 22151



aerodyne research

AD755840

A STUDY OF WIND TUNNEL SIMULATION OF
HIGH ALTITUDE ROCKET PLUMES

by

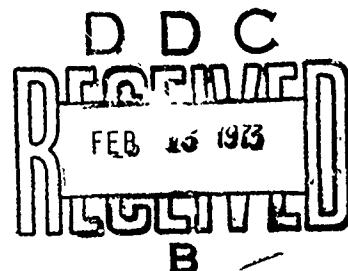
James Stark Draper

James P. Moran

AERODYNE RESEARCH INC.
BURLINGTON, MASSACHUSETTS 01803

Technical Report AFRPL-TR-72-111
February 1973

Approved for Public Release
Distribution Unlimited



Air Force Rocket Propulsion Laboratory
Director of Science and Technology
Air Force Systems Command
Edwards Air Force Base, California

Reproduced by
NATIONAL TECHNICAL
INFORMATION SERVICE
U S Department of Commerce
Springfield VA 22151

162

ACCESSION for	
CTIS	White Section <input checked="" type="checkbox"/>
CT	Buff Section <input type="checkbox"/>
UNA	CEB <input type="checkbox"/>
Distribution	
BY	
DISTRIBUTION/AVAILABILITY CODES	
Dist.	AvAIL. and/or SPECIAL
A	

"When U.S. Government drawings, specifications, or other data are used for any purpose other than a definitely related Government procurement operation, the Government thereby incurs no responsibility nor any obligation whatsoever, and the fact that the Government may have formulated, furnished, or in any way supplied the said drawings, specifications or other data, is not to be regarded by implication or otherwise, or in any manner licensing the holder or any other person or corporation, or conveying any rights or permission to manufacture, use, or sell any patented invention that may in any way be related thereto."

Security Classification

DOCUMENT CONTROL DATA - R & D

(Security classification of title, body of abstract and indexing annotation must be entered when the overall report is classified)

1. ORIGINATING ACTIVITY (Corporate author) AERODYNE RESEARCH, INC. Northwest Industrial Park Burlington, Massachusetts 01803		2a. REPORT SECURITY CLASSIFICATION (Unclassified)	
3. REPORT TITLE A Study of Wind Tunnel Simulation of High Altitude Rocket Plumes		2b. GROUP ---	
4. DESCRIPTIVE NOTES (Type of report and inclusive dates) Final Report, February 1973			
5. AUTHOR(S) (First name, middle initial, last name) James Stark Draper, James P. Moran			
6. REPORT DATE February 1973	7a. TOTAL NO. OF PAGES 168 162	7b. NO. OF REFS. 76	
8a. CONTRACT OR GRANT NO. F04611-72-C-0063	8b. ORIGINATOR'S REPORT NUMBER(S) ARI-RR 12		
8c. PROJECT NO.	9b. OTHER REPORT NO(S) (Any other numbers that may be assigned this report)		
10. DISTRIBUTION STATEMENT Approved for Public Release: Distribution Unlimited			
11. SUPPLEMENTARY NOTES		12. SPONSORING MILITARY ACTIVITY Air Force Rocket Propulsion Laboratory Director of Science and Technology AFSC, Edwards AFB, California	
13. ABSTRACT <p>A review of several simple, inviscid, high-altitude rocket plume models shows that the Jarvinen-Hill model is the most accurate such representation. This model offers a compact use of the important scaling parameters, particularly the hypersonic plume scale, $L = \sqrt{\text{rocket thrust/freestream dynamic pressure}}$. The HAPRAP wind-tunnel plume measurements have been used to verify the Jarvinen-Hill model and to study the plume viscous mixing layers which simulated flight conditions by matching wind tunnel and flight plume Knudsen numbers, $Kn_L = \text{freestream mean free path}/L$. The HAPRAP data simulate typical ICBM sustainer flight in the 120 to 320 km altitude range.</p> <p>The viscous mixing layer location was characterized by the surface along which the jet and freestream species are equal. These surfaces, when normalized by L, collapsed toward a single surface, which displayed Jarvinen-Hill inviscid model behavior. In addition, viscous influences on surface locations and particle concentrations along equal concentration surfaces were identified. Data at a single point showed the pressure at this surface to be approximated by the Newtonian pressure formula. Plume outer shock locations, when normalized by L, showed poor correlation due to a variety of factors. These shock structures became quite weak in the higher altitude simulations as Kn_L approached 10^{-1}. The inner shock data showed that the internal scaling of the Jarvinen-Hill Model must be improved.</p> <p>Deviations of the small-scale details of the plume mixing-layer structure from continuum behavior are used for infer the appearance of rarefaction effects. For the most rarefied HAPRAP data, $Kn_L = 10^{-1}$ at $M_\infty = 8$, the small-scale flow is substantially rarefied, however, the large-scale plume dimensions are well approximated by continuum calculations and the plume flow is in the transitional density regime.</p> <p>The Jarvinen-Hill continuum model is useful for estimating large-scale plume dimensions for $Kn_L < 10^{-1}$. A nomograph designed for quick calculations of these plume dimensions is accordingly included. Departure of local plume properties from continuum conditions should be considered for $Kn_L > 10^{-2}$. Based on the data examined, the development of a simple plume model describing both the mean thermodynamic and structural features of the mixing layer in the high-altitude continuum and transitional rocket plume appears feasible.</p>			

14. KEY WORDS	LINK A		LINK B		LINK C	
	ROLE	WT	ROLE	WT	ROLE	WT
High Altitude Rocket						
Exhaust Plumes						
Hypersonic Flow						
Radiation						
Electron Beam						
Wind Tunnel Test						
Shock Waves						
Shear Layer						
Aerodynamic						
Rarefied Gases						

**A STUDY OF WIND TUNNEL SIMULATION OF
HIGH ALTITUDE ROCKET PLUMES**

by
**James Stark Drpaer
James P. Moran**

**Final Report
Contract No. FO4611-72-C-0063**

February 1973

**Approved for Public Release
Distribution Unlimited**

**Air Force Rocket Propulsion Laboratory
Director of Science and Technology
Air Force System Command
Edwards Air Force Base, California**

FOREWORD

AFRPL-TR-72-111

ARI-RR12

**A STUDY OF WIND TUNNEL SIMULATION OF
HIGH ALTITUDE ROCKET PLUMES**

by

**James Stark Draper
James P. Moran**

**AERODYNE RESEARCH INC.
TECH/OPS BUILDING
NORTHWEST INDUSTRIAL PARK
BURLINGTON, MASSACHUSETTS 01803**

**Contract No.: FP4611-72-C-0063
System Project No.: 5730
Task No.: 573009**

**Final Report
February 1973**

**Period Covered: February 18, 1972 through October 31, 1972
Contract Monitor: Capt. Samuel B. Thompson, AFRPL/DYSP**

**Approved for Public Release
Distribution Unlimited**

**Prepared for
Air Force Rocket Propulsion Laboratory
Director of Science and Technology
Air Force Systems Command
Edwards Air Force Base, California**

This Technical Report has been Reviewed and is Approved

**Paul J. Daily, Lt. Colonel, USAF
Chief, Technology Division**

TABLE OF CONTENTS

<u>Section</u>	<u>Page</u>
FOREWORD	ii
ABSTRACT	v
NOMENCLATURE	xiii
I THE SIMPLE PLUME MODEL: ITS UTILITY AND NATURE	1
1.1 DEVELOPMENT OF HIGH ALTITUDE INVISCID PLUME MODELS	3
1.1.1 Early Work	3
1.1.2 The Hypersonic Plume Scale: \bar{L}	6
1.1.3 The Nozzle Efficiency	10
1.2 LIMITATIONS OF THE HYPERSONIC, INVISCID PLUME	16
1.2.1 Inviscid Flow	16
1.3 AREAS FOR IMPROVEMENT IN THE PLUME MODEL	28
II VALIDATION OF THE MEASUREMENTS	31
2.1 THE HAPRAP MEASUREMENTS: PURPOSE, TYPE, SCOPE	31
2.2 GASDYNAMIC EFFECTS	33
2.3 ELECTRON BEAM CONCENTRATION MEASUREMENTS	42
2.3.1 Flow Field Concentration Measurements by Electron Beams	43
2.3.2 Validity of the Concentration Measurements . . .	44
2.3.3 Flow Visualization Image Slip	57
2.4 SUMMARY OF THE MEASUREMENTS VALIDATION	61

TABLE OF CONTENTS (Cont.)

<u>Section</u>	<u>Page</u>
III AERODYNAMIC SIMULATION OF FULL SCALE PLUMES	63
3.1 THE SIMULATION PARAMETERS	63
3.2 RANGE OF SIMULATION PARAMETERS	64
3.3 SUMMARY OF THE AERODYNAMIC SIMULATION	78
IV PLUME MIXING LAYER FLOW FIELD ANALYSIS	81
4.1 THE PLUME OUTER SHOCK	81
4.2 THE MACH DISC	88
4.3 THE MIXING LAYER	90
4.4 SUMMARY OF FLOWFIELD ANALYSIS	101
V RAREFACTION PHENOMENA IN PLUME FLOW	105
5.1 PREVIOUS WORK	105
5.2 SCALING AND NONTHERMAL EFFECTS OF RAREFACTION	111
5.2.1 Continuum-Transitional Flow Regime Boundary Based Upon Dimensional Scaling Considerations	111
5.2.2 Continuum-Transitional Flow Regime Boundary Based Upon Nonthermal Considerations	117
5.3 RAREFACTION IN HIGH ALTITUDE ROCKET PLUMES	120
5.4 RAREFACTION EFFECTS: SUMMARY	125
VI SUMMARY AND RECOMMENDATIONS	129
6.1 SUMMARY	129
6.1.1 Plume Parameters and the Jarvinen-Hill Plume Model	129
6.1.2 Applicability of the Jarvinen-Hill Model	130
6.1.3 The HAPRAP Flow-Interaction Measurements ..	131
6.1.4 Simulation of High Altitude Plumes	131

TABLE OF CONTENTS (Cont.)

<u>Section</u>	<u>Page</u>
VI (Cont.) 6.1.5 The Shock Data	132
6.1.6 The Mixing Layer Structure	132
6.1.7 The Transitional Flow Regime	133
6.2 RECOMMENDATIONS	135
6.2.1 A Plume Nomogram	135
6.2.2 The Evaluation of Rerefraction Effects for $Kn_{\bar{L}} > 1 \times 10^{-2}$	138
6.2.3 Further Development of a Simple High Altitude Mixing Layer Plume Model	138
REFERENCES	141
ACKNOWLEDGMENTS	149

LIST OF ILLUSTRATIONS

<u>Figure</u>		<u>Page</u>
1	Schematic View of the Plume Flowfield	2
2	Correlation of Blast Wave Theory with Observations	7
3	Inviscid Plume Model Contact Surfaces Compared with Numerical Solution of Boynton	8
4	The Nozzle Efficiency and Plume Drag-to-Thrust Ratio as a Function of Engine-Area Ratio and Ratio of Specific Heats	14
5	Shock Detachment Altitude	20
6	Correlation of Plume Nose Shape with $C_F/C_{F_{max}}$	21
7	Jet-Freestream Interaction Experiment Setup for the High Altitude Plume Radiation Program	32
8	Evaluation of Appearance of Macroscopic Condensation Effects in HAPRAP Jets	35
9	Shock Location Dependence Upon Nozzle Chamber Temperature	38
10	Pitot Probe Measurements Compared with Farfield Jet Calculations	40
11	Comparison of Calculated and Measured Electron Beam Densities	46
12	Electron Beam Density Measurements Compared to Farfield Jet Calculations	47
13	Jet Particle Fluxes Measured by Electron Beam	50
14	Helium Energy Level Diagram	51
15	Sketch of N_2 Shock "Flow Slip"	58
16	Plume Outer Shock Location by Three Techniques	60
17	Typical Missile Mach Number Altitude Histories	65
18	Typical Missile Velocity Altitude Histories	65
19	Full Scale and HAPRAP Plume Shape Parameters	66
20	Full Scale and HAPRAP Reynolds Number	70
21	Scale and HAPRAP Plume Knudsen Numbers	71

LIST OF ILLUSTRATIONS (cont.)

<u>Figure</u>		<u>Page</u>
22	Kundsen Number Based on Nozzle Exit Conditions for Full Scale Vehicles and HAPRAP Tests	73
23	Ratio of Vehicle Body Length to Plume Characteristic Length	77
24	Electron Beam Flow Visualization Photographs for ASC(10V) Cases No. 3,4,6	82
25	Electron Beam Flow Visualization Photographs for ASC(10V) Case No. 5 and Tunnel M Case IB	83
26	Viscous Layer Influence on Outer Shock Layer Location	85
27	Dependence of Mach Disk Location on Plume Drag-to-Thrust Ratio	89
28	Typical Electron Beam Surveys	91
29	Separated Flow Region-Medium Altitude Plume (80-100 km Altitude)	92
30	Surfaces of Equal Concentration for Fixed D/T, m_{∞}/m_j	95
31	Surfaces of Equal Concentrations for Varying m_{∞}/m_j , Fixed D/T	96
32	Surfaces of Equal Concentrations for Varying D/T, Fixed m_{∞}/m_j	97
33	Concentrations Along Surfaces to Equal Concentrations	98
34	Normalized Concentrations Along the Concentration Surfaces	99
35	Rarefaction Diagram Showing Simons' Results for Continuum Transitional Boundary and Muntz's for Scattering Regime Boundary	108
36	HAPRAP Plume Small Scale Structures Normalized by the Ambient Mean Free Path vs the Plume Knudsen Number to Show Transitional Scaling of the Small Scale Structures	112
37	Rarefaction Diagram Showing Density Regime Boundaries and Range of Simulation of ICBM Flight Achieved in HAPRAP Flow Interaction Study	121
38	Rarefaction Diagram Showing Velocity Dependence for Small Scale Structure Rarefaction Processes	122

LIST OF ILLUSTRATIONS (cont.)

<u>Figure</u>		<u>Page</u>
39	Rarefaction Diagram Showing the Approximate Location for Rarefaction for the Large Scale Plume Structures	123
40	Flow Visualization Photographs of Plume in Continuum and Transitional Flow Regimes	124
41	Nomogram for Plume Structures	136

NOMENCLATURES

a_c	=	model rocket chamber speed of sound
A_e	=	engine exit area
A^*	=	engine throat area = πr^{*2}
A_e/A^*	=	engine nozzle area ratio
C_D	=	drag coefficient
C_F	=	engine vacuum thrust coefficient
$C_{F_{max}}$	=	engine vacuum thrust coefficient for infinite area ratio
C_p	=	modified Newtonian pressure coefficient
\bar{c}_∞	=	freestream mean thermal speed
D	=	plume drag
d^*	=	engine throat diameter
E_{act}	=	activation energy
$f(\theta)$	=	angular mass flow distribution
g	=	escape factor
gI_{sp}	=	c_{eff} , effective engine speed
H_c	=	model rocket chamber enthalpy
I	=	emission per unit volume
I_0	=	downstream asymptotic limit of steady state emission as spread out by convection of the radiating states
J	=	nucleation rate or nuclei formed per unit volume per unit time
j	=	electron beam current density
k	=	Boltzmann constant
k_b	=	bimolecular hard sphere rate constant

NOMENCLATURE (Continued)

k_d	=	collisional deactivation rate constant
k_q	=	quenching rate constant
k_o	=	maximum absorption coefficient
Kn_e	=	engine exit plane Knudsen number = λ_e/d_e
$Kn_{\bar{L}}$	=	plume Knudsen number = λ_∞/\bar{L}
K_{NP}	=	plume Knudsen number (Muntz) = $r_{1/e}/r_p$
\bar{L}	=	hypersonic-plume scale = $(T/q_\infty)^{1/2}$
L_{MD}	=	Mach disk axial position
ℓ	=	degeneracy of ground level
ℓ^*	=	degeneracy of excited level
ℓ_m	=	missile length
M	=	molecular weight
M_e	=	engine nozzle exit Mach number
M_n	=	Mach number at the outer edge of the boundary layer
M_∞	=	freestream Mach number
\dot{m}	=	engine mass flow
m_c	=	model rocket chamber particle mass
m_j	=	jet species molecular mass
m_μ	=	reduced mass of freestream and jet gas
m_∞	=	ambient or freestream molecular mass
\bar{n}	=	normalized concentration along surfaces of equal concentrations
n_j	=	concentration of species j

NOMENCLATURE (Continued)

N_s	=	total collisions of ambient particles in plume nose cap region
\dot{N}_j	=	model rocket jet total number flux
p	=	gas pressure
p_c	=	model rocket chamber pressure
p_L	=	vapor pressure over-drop
p_∞	=	freestream static pressure
p_v	=	flat firm vapor pressure of liquid
q_j	=	jet core dynamic pressure
q_∞	=	freestream dynamic pressure
R	=	effective radius of gas sample
R_b	=	the body nose radius
Re_L	=	Reynolds No. based on plume scale
R_N	=	nose radius
R_{NP}	=	plume nose radius
R_s	=	plume outer shock nose radius
r	=	radial distance from jet exit
r_j	=	radius of species j
r'	=	critical drop size for growth
r^*	=	engine throat radius
s	=	length of boundary layer development along nozzle wall
t	=	viscous layer thickness
T	=	engine vacuum thrust

NOMENCLATURE (Continued)

u_{lim}	=	exhaust gas limiting speed
u_{∞}	=	freestream speed
W	=	full half width of Gaussian shaped electron beam
x	=	distance along jet axis from jet exit
y	=	transverse distance from jet axis
\bar{x}	=	x/\bar{L}
\bar{y}	=	y/\bar{L}
\hat{x}	=	\bar{x}
\hat{y}	=	$\bar{y} \cdot (D/T)^{-1/4}$
\tilde{x}	=	$\bar{x} M_e^{-1}$
\tilde{y}	=	\bar{y}
$[y]$	=	freestream species concentration
$[z]$	=	jet species concentration
γ_j	=	jet ratio of specific heats
γ_{∞}	=	ambient or freestream ratio of specific heats
δ	=	shear layer thickness or boundary layer thickness
Δ	=	distance from shear layer to outer shock
ϵ	=	$(\gamma_{\infty} - 1)/(\gamma_{\infty} + 1)$
Θ_c	=	model rocket chamber temperature
Θ	=	temperature
Θ_L	=	droplet temperature
Θ_o	=	wind tunnel stagnation temperature

NOMENCLATURE (Continued)

θ_t	=	translational temperature
θ_s	=	temperature behind a normal shock
θ_∞	=	ambient or freestream temperature
θ	=	radial flow angle measured from jet axis
θ_e	=	nozzle exit angle measured from jet axis
λ	=	wavelength
λ_c	=	reservoir mean free path
λ_n	=	mean free path at outer edge of nozzle boundary layer
λ_e	=	engine exit mean free path
λ_∞	=	freestream mean free path
μ	=	viscosity
μ_∞	=	freestream viscosity
μ_c	=	model rocket chamber viscosity
ν	=	kinematic viscosity
ρ	=	farfield flow density
$\bar{\rho}$	=	inner shock layer density normalized by Jarvinen-Hill method
ρ_c	=	model rocket chamber density
$\rho_{\theta=0}$	=	density at $\theta = 0$
ρ_L	=	liquid density
ρ_s	=	density behind a normal shock
ρ_{sl}	=	inner shock layer density
ρ_∞	=	freestream density

NOMENCLATURE (Concluded)

σ	=	surface tension
σ_{exc}	=	electron excitation cross section
σ_j	=	hard body cross-section of species j
σ_{∞}	=	local plume contact surface inclination to the freestream
τ	=	plume slenderness = $y_{\text{max}} / x_{\text{max}}$
τ_{rad}	=	lifetime for all radiation transitions from an excited state
τ_{eff}	=	effective lifetime for He (1s3p) state
τ_{col}	=	collisional quenching lifetime
τ_{λ}	=	lifetime of observed radiation
[]	=	species concentration

Section 1

THE SIMPLE PLUME MODEL: ITS UTILITY AND NATURE

The boost-phase radiation signatures of high-altitude strategic missiles and the possibility of design modifications varying these signatures play a key role in the development of satellite warning systems. A wide variety of experimental, theoretical, and field-measurement programs have been directed toward the study of the radiation phenomenology of rocket-exhaust flow fields. These programs have resulted in a fairly clear understanding of the nature of plume radiation below 70 kilometers. The detailed nature of high altitude plume radiation, however, is not presently understood, partly due to the difficulty of obtaining numerical solutions for the highly-underexpanded rocket plumes characteristic of rockets at high altitudes. This problem is further complicated by the occurrence of significant gas-transport and transitional-low effects and by the difficulty of ground-based simulation of some of the relevant, collision-limited, long-lived radiation processes.

Greatly simplified inviscid plume models have been constructed to describe the important features of high altitude rocket exhausting into coparallel streams. These simple models describe, for instance, the location of shocks and contact surfaces. The phrase, plume model, as used here, pertains to simple techniques rather than to very complex descriptions based upon numerical analyses. Simplified models are intended to aid in the analysis of field measurements and wind tunnel simulations and to provide physical insight into the fundamental behavior of plume flowfields. At sufficiently high altitudes the viscous mixing layer between jet and ambient gases is no longer thin so the concept of an inviscid contact surface becomes inappropriate. At still higher altitudes, relevant mean-free-paths become comparable to plume dimensions, thus the flowfield cannot be wholly described by continuum concepts. Consequently, inviscid plume models become of limited value as missile altitude increases. In comparing experimental measurements with such models it is important, therefore, that consideration be given to their limits of applicability.

In 1970 the Air Force Rocket Propulsion Laboratory, in conjunction with the Aerospace Corporation, formulated the High Altitude Plume Radiation Program (HAPRAP) to provide laboratory data to aid in the understanding of high altitude plume radiation phenomenology. At the Arnold Engineering Development Center (AEDC), of Tullahoma, Tenn., flowfield studies were conducted with engines exhausting into a near vacuum in the Mark I chamber, and for model rockets exhausting into supersonic or hypersonic flowing streams in the M and D wind tunnels and in Aerospace Chamber 10V at the von Karman Facility. The model rocket studies were conducted with the rocket nozzle axis coparallel with, perpendicular to, and opposed to the freestream. In the present work only the coparallel studies in a flowing stream are studied. The utility, applicability, and possibility of improvement of existing plume models with the aid of the HAPRAP data is of major concern in the present work, with particular emphasis placed on the validity of the Jarvinen-Hill plume model.

Characteristic features of a continuum high-altitude rocket plume are sketched in Figure 1. Typically the missile is moving at supersonic speeds, therefore, the plume is preceded by a plume outer shock. Since the rocket exhaust is a supersonic, highly underexpanded axisymmetric flow, it overexpands and adjusts to the external flow by a reentrant, plume inner shock (sometimes termed the "barrel shock") surface converging at the "Mach disc." The flow immediately downstream of the Mach disc is subsonic. In the inviscid limit, freestream and exhaust gases would be separated by a contact surface. In reality, a relatively thin mixing layer forms wherein diffusive, viscous and other transport phenomena are important.

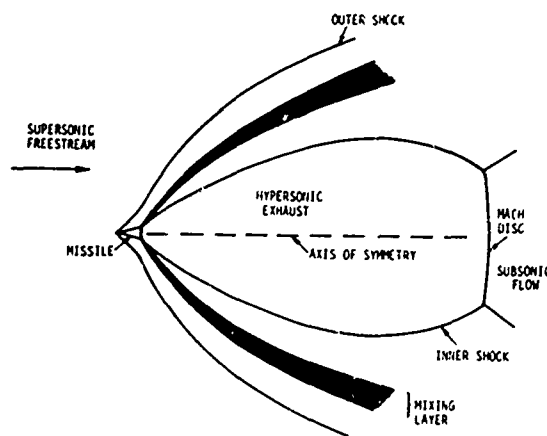


Figure 1 - Schematic View of the Plume Flowfield

Several "analytic models" have been proposed to describe the flowfields of high altitude rocket vehicle moving at supersonic speeds. "Model" denotes a simplified physical description translated into an approximate but easy to use computational technique. "Analytic" implies a series of closed form scaling laws which allow estimates of such major structural features of the plume as the inner and outer shocks, contact surface and Mach disc. These models are based partly upon numerical solutions to inviscid flows and partly upon field observations of high altitude missile plumes.

Common assumptions in the plume models are:

1. Axisymmetric, coparallel flow,
2. Highly underexpanded exhaust – so that: a) the rocket body structure does not significantly perturb the flow; and b) the undisturbed interior flow is radial moving at a speed approaching the gas limiting speed, based on engine conditions,
3. Hypersonic exterior flow – so that ambient static pressure does not affect plume structure,
4. Inviscid flow.

The last assumption is perhaps the most restrictive in modeling very high altitude plumes. The basic purpose of the HAPRAP mixing layer measurements is to study this specific aspect of plume flow.

1.1 DEVELOPMENT OF HIGH ALTITUDE INVISCID PLUME MODELS

1.1.1 Early Work

Early investigations of underexpanded engine exhausts consisted of experiments supplemented by applications of the method of characteristics (MOC) and shock expansion techniques.^(1, 2) Adamson and Nicholls,⁽³⁾ Latvala,⁽⁴⁾ and Love, Grigsby, and Lee⁽⁵⁾ established the overall structure of highly underexpanded jets in still air. Experimental results were compared with MOC calculations and

approximate theoretical methods. It was determined that the dimensions of exhaust plumes in still air scale as the inverse square root of the ambient pressure.

While studies of exhaust plumes in still air continued,^(6, 7) photographs published by Rosenberg⁽⁸⁾ of the Air Force Cambridge Research Laboratories in the early 1960's showing the full scale ICBM mixing layer structures at high altitudes stimulated a strong interest in exhaust plumes in supersonic streams. From these photographs it is seen that one of the strongest radiation regions was associated with a parabolic structure in the forward plume region where the freestream dynamic pressure exerts the dominant influence on the aerodynamic structure. Successive theoretical descriptions of these observations were developed by Thompson and Harshbarger⁽⁹⁾ and later by Hill and Habert.⁽¹⁰⁾

Thompson and Harshbarger⁽⁹⁾ discussed the plume "drag" and presented maximum plume radii normalized by the square root of thrust divided by ambient pressure. These dimensionless radii displayed a largely inverse dependence on the freestream Mach number, M_∞ . They showed the behavior appropriate to plumes in hypersonic streams later expressed in compact form by Alden and Habert⁽¹³⁾ via the length,

$$\bar{L} = \left(\frac{T}{q_\infty} \right)^{1/2} \quad (1)$$

where T is the engine vacuum thrust and q_∞ is the freestream dynamic pressure.

In this work, it was also shown that a secondary scaling dependence exists in terms of the nozzle thermodynamic efficiency,¹ the ratio of engine thrust to the thermodynamically-maximum thrust,

¹The phrase "nozzle efficiency" usually refers to various nonisentropic nozzle flow losses (e.g., boundary layer losses). As used herein, it refers only to the nozzle thermodynamic efficiency obtained from Equation (2).

$$\frac{T}{\dot{m} u_{lim}} = \frac{C_F}{C_{F_{max}}} \quad (2)$$

where

- \dot{m} = engine mass flow
- u_{lim} = exhaust gas limiting speed
- C_F = engine vacuum thrust coefficient
- $C_{F_{max}}$ = engine vacuum thrust coefficient for infinite area ratio.

The plume size was shown to decrease as nozzle efficiency increased. These two scaling parameters appear in most subsequent high-altitude plume studies.

The theory of exhaust plumes viewed ad hypersonic bodies of revolution, characterized by drag and frontal area, was developed further by Hill and Habert.⁽¹⁰⁾ They argued, by use of overall plume momentum balance, that when the missile is operating at high altitudes (> 100 km) plume drag can be expressed in terms of engine characteristics independent of ambient pressure. Thus, they obtained

$$\frac{D}{T} = \frac{C_{F_{max}}}{C_F} - 1 \quad (3)$$

Their momentum balance formulation of the plume drag assumes that the limiting gas speed is preserved as the jet gas passes through the inner shock at large distances from the nozzle exit. Then the plume drag is simply maximum attainable thrust minus engine vacuum thrust, which leads immediately to Equation (3). However, since the right-hand side of Equation (3) is small for typical high altitude engines, even minor deviations from the above isentropic shock assumption will lead to substantial errors in D/T.

Assuming this view of the plume boundary as a body of revolution in hypersonic flight and that this body is slender, Hill and Habert applied the blast wave analogy of Lees⁽¹¹⁾ to obtain a parabolic plume outer shock radius, R_s , with constant parabola expressed in terms of plume drag as

$$R_s = 0.364 \left(\frac{D}{q_\infty} \right)^{1/2} \quad (4)$$

for freestream ratios of specific heats equal to 1.4.

Although the theory from which this parabolic outer shock is obtained is valid only where the plume is slender, Hill and Habert⁽¹⁰⁾ applied it to available field observations in the blunt plume nose region with favorable agreement for an ambient density range of an order of magnitude. Their comparison, shown here in Figure 2, constitutes the first validation of plume scaling by $(D/q_\infty)^{1/2}$ for full scale booster rockets. In this comparison $(D/q_\infty)^{1/2}$ is large ($\sim 10^3$ meters), and plume nose radii are much larger than missile dimensions, thus the outer shocks are not strongly disturbed by missile bodies. Jarvinen and Dynner⁽¹²⁾ later successfully applied this scaling of bow shock shapes at much smaller $(D/q_\infty)^{1/2}$ (~ 0.1 meter) for plume nose radii smaller than the body, as shown also in Figure 2.

1.1.2 The Hypersonic Plume Scale: \bar{L}

For fixed nozzle geometry and jet gas, plume drag is proportional to thrust (see Equation (3)). The bow shock radius, which was found by Hill and Habert to scale as (D/q_∞) therefore also scales with \bar{L} .

Alden and Habert⁽¹³⁾ derived a differential equation for the inviscid plume contact surface based upon Newtonian flow theory with a centrifugal correction. Contact surface coordinates, when normalized by the hypersonic plume scale, were found to depend only on nozzle geometry and jet gas specific heat ratio.

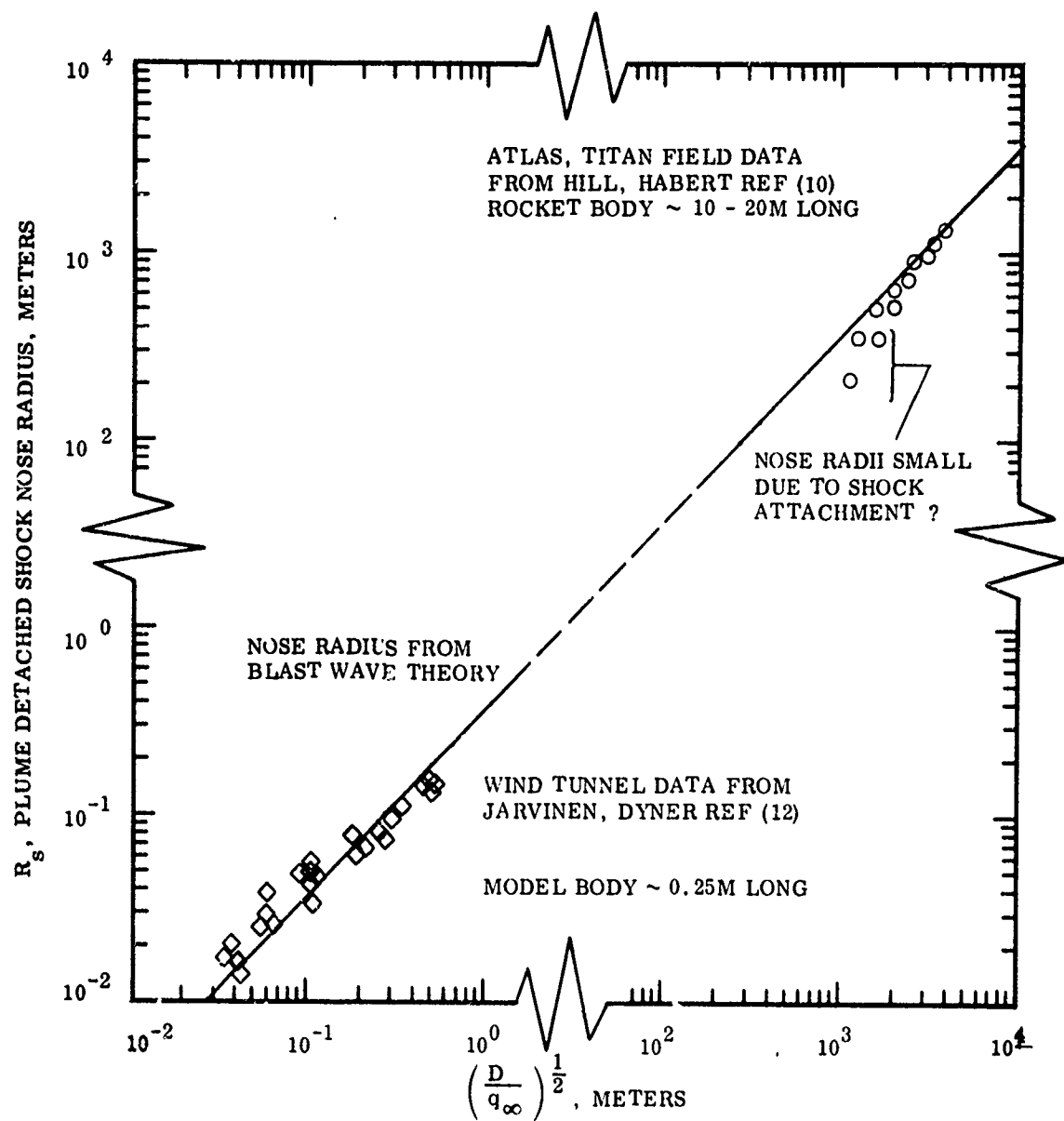


Figure 2 - Correlation of Blast Wave Theory with Observations

This is apparently the first plume model in which scaled contact surface shapes are predicted with parametric dependencies on nozzle characteristics. Their results are shown here in Figure 3 for one value of D/T , where contact surface coordinates are normalized by $(T/q_\infty)^{1/2}$.

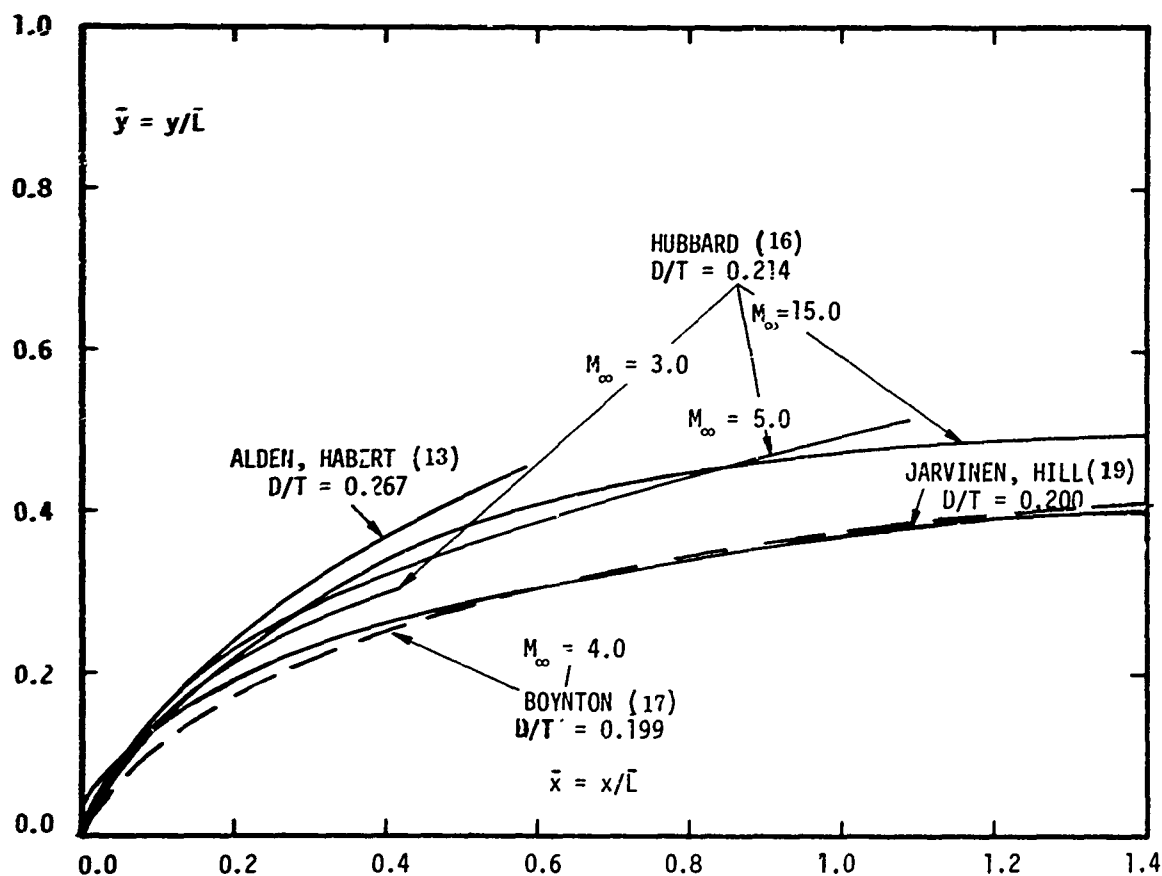


Figure 3 - Inviscid Plume Model Contact Surfaces Compared with Numerical Solution of Boynton

The works of both Hill and Habert and Alden and Habert indicate that both the outer shock nose region and that portion of the contact surface where strongly hypersonic external flow prevails scale as $(T/q_\infty)^{1/2}$. "Strongly

hypersonic flow" occurs when pressures along the contact surface are large compared to freestream static pressure. Moran⁽¹⁴⁾ subsequently demonstrated by purely dimensional arguments that the entire inviscid plume structure for highly underexpanded nozzles scales with $(T/q_\infty)^{1/2}$ when the external flow is strongly hypersonic, and as the square root of the thrust divided by the free-stream static pressure $(T/p_\infty)^{1/2}$, with M_∞ as an additional parameter when the external flow is not strongly hypersonic. In actual high-altitude plumes, the external flow is strongly hypersonic in the forward, blunter regions, but not in the aft, more-slender regions. Scaling by $(T/q_\infty)^{1/2}$ is, however, still suitable for these plumes when radiation signatures are considered, since one of the most important sources of radiation is in this forward region.⁽⁸⁾

Albini⁽¹⁵⁾ calculated the inviscid contact surface using the approximations of Alden and Habert. He further calculated the location of the inner shock by including a mass balance along the inner shock layer. Hubbard⁽¹⁶⁾ pointed out that neither Alden and Habert nor Albini conserved tangential momentum in the inner shock layer. He corrected this by adjusting the inner shock layer transverse properties according to the conditions under which streamlines enter the inner shock layer. Hubbard thus obtained more slender contact surfaces than those obtained by either Alder and Habert or Albini (refer to Figure 3). Note that since Alden and Havert, Albini, and Hubbard all neglect ambient static pressure, their models apply to strongly hypersonic external flows. At the time these calculations were made, no laboratory or field data were available for comparison.

Boynton⁽¹⁷⁾ made a definitive theoretical evaluation of these models by comparison with the results of a precise numerical computer program employing a finite difference technique. He showed that Hubbard's method of calculating the plume contact surface gives satisfactory results for a suitable form of flow in the undisturbed jet core, provided that the centrifugal correction is omitted in the outer shock layer. With these modifications, Hubbard's method yielded a contact surface which overlaid the numerical solution for one case considered (this is shown as the broken curve in Figure 3).

Boynton also demonstrated the level of development of computer techniques in plume calculations. A fairly general treatment of a broad range of plume phenomena is available from Thompson et al.⁽¹⁸⁾ in which this finite difference scheme for calculating plume structure is described and fairly extensive calculations are shown. Such computerized numerical treatments of complex problems related to booster rocket flowfields (e.g. aerodynamic noise, flow separation, etc.) have been highly developed by DOD laboratories, NASA, and aerospace and research consulting companies. Plume technology development based on computerized numerical techniques is not further discussed here.

The plume structure scaling used by Albini, Hubbard, and Boynton is essentially $(T/p_\infty)^{1/2}$ with other engine and freestream effects plotted parametrically. These results have been converted to $(T/q_\infty)^{1/2}$ scaling in Figure 3. Therefore, scaling the dimensions of the forward region of the plume structure with $(T/q_\infty)^{1/2}$ appears to be quite useful.

1.1.3 The Nozzle Efficiency

Recently, Jarvinen and Hill⁽¹⁹⁾ proposed a simple model incorporating both the hypersonic plume scale and the nozzle efficiency. Their approach utilizes the plume drag-to-thrust ratio to express the nozzle efficiency. As shown in Equation (3) above, D/T is related to $C_F/C_{F_{max}}$, which is the nozzle efficiency in realizing its full thermodynamic thrust potential. The contact surface predicted by the Jarvinen and Hill "universal" plume model is shown for $D/T = 0.200$ (close to Boynton's conditions) in Figure 3. The comparison with Boynton's numerical solution is quite satisfactory. However, this is expected since the universal model is ultimately based upon extensive numerical calculations for ICBM-type engines with nozzle efficiencies comparable to those in Boynton's solution.

The hypersonic plume scale determines the size of the plume structure which is modified by the nozzle efficiency. The dominant length scaling for the high-altitude (vanishingly small nozzle scale) plume with strongly hypersonic external flow is $(T/q_\infty)^{1/2}$. The weaker dependences of plume structure on the freestream and jet ratios of specific heats, the nozzle exit Mach number, and nozzle exit angle remain.

The freestream ratio of specific heats will have a significant effect on the air shock layer thickness, hence the outer shock position, and a lesser effect on the contact surface location through its effect on the modified Newtonian pressure coefficient, C_p . For inviscid high-altitude plumes, the air shock layer aerodynamics are virtually uncoupled from the shock layer chemistry. For high altitudes, where the ambient ratio of specific heats, γ_∞ , is between 1.40 and 1.67, the variation in the location of the contact surface ($\propto C_p^{1/2}$) may be at most about $\pm 1\%$. The contact surface location may be assumed to be independent of the freestream ratio of specific heats. The nozzle exit angle, if it is small, has a small effect on plume structure. Since this condition is usually satisfied, it will be omitted from further consideration.

The remaining parameters of jet specific heat ratio and exit Mach number may neither be neglected nor assumed constant. The question of whether these may be combined into a single engine-design parameter or must remain as separate independent parameters now arises. Since these parameters affect the plume structure through their influence on the undisturbed interior jet flow, consideration will be briefly given to models for jets exhausting into vacuum. In the far-field (for instance > 10 exit diameters downstream of the nozzle exit) pressure forces become very small compared to inertia forces so that the flow is radial with speeds very near the limiting speed. Therefore, the flow preserves its angular mass flow distribution, $f(\theta)$, with distance downstream from the jet exit. The farfield flow density, ρ , is given in polar coordinates in the notation of Sibulkin and Gallagher's⁽²⁰⁾ center-line decay parameter, B

$$\rho(r, \theta) = \frac{B d^{*2} \rho_c}{r^2} f(\theta) \quad (5)$$

where, r = distance from jet exit, θ = radial flow angle measured from jet axis, $B(\gamma_e, M_e) = (\rho_{\theta=0}/\rho_c) (r/d^*)^2$, ρ_c = engine chamber density, d^* = engine throat diameter $\rho_{\theta=0} = \rho_{\theta=0}(r)$ = density at $\theta = 0$.

Note that B does not depend on coordinates because $\rho_{\theta=0} \propto r^{-2}$ in the farfield. Hence, local farfield flow density is a function of radial position, engine design, and mass flux distribution. For single calculations, jet flow models of a form for $f(\theta)$ are chosen to closely approximate numerical calculations of farfield exhaust flow.

The choice of a suitable form for $f(\theta)$ is not considered here but rather the way in which γ_j and M_e may be combined as a single parameter in $f(\theta)$. This mass distribution function is constrained by overall conservation of mass and momentum in the plume. The total mass and axial momentum which cross a spherical surface centered at the nozzle exit must be independent of r and equal to nozzle mass flow \dot{m} and engine thrust T respectively. Then, from Equation (5),

$$\dot{m} = 2\pi B d^2 \rho_c u_{\text{lim}} \int_0^\pi f(\theta) \sin \theta \, d\theta \quad (6)$$

$$T = 2\pi B d^2 \rho_c u_{\text{lim}}^2 \int_0^\pi f(\theta) \cos \theta \sin \theta \, d\theta \quad (7)$$

Expressing the mass flow in terms of the maximum thermodynamically realizable thrust

$$T_{\text{max}} = \dot{m} u_{\text{lim}} \quad (8)$$

and transforming $f(\theta)$ into a function $F(p)$ of solid angle in polar coordinates, where $p = \cos \theta$, there results

$$\frac{C_F}{C_{F_{\text{max}}}} = \frac{\int_{-1}^1 F(x) \, dx}{\int_{-1}^1 F(x) \, dx} \quad (9)$$

Thus, nozzle efficiency is an important factor in the width of the mass distribution function. Less efficient nozzles yield fuller mass flow distributions (e.g., sonic nozzles) whereas more efficient nozzles (those with high area ratios) yield narrow mass flow distributions weighted by $x \approx 1$. Since $C_F/C_{F_{\max}}$ is a function of γ_j and M_e (or A_e/A^*), and since these parameters affect the farfield only in the fullness of the farfield flow distribution, it is plausible to represent the mass distribution function $f(\theta)$ solely in terms of the ratio, $C_F/C_{F_{\max}}$.

A suitable one-parameter family of curves $f(\theta; \beta)$ may be used in Equation (9) to express β in terms of $C_F/C_{F_{\max}}$ and then in Equation (7) to evaluate B. Then, in coordinates normalized by $(T/q_\infty)^{1/2}$, plume geometry depends upon the engine parameter $C_F/C_{F_{\max}}$. Consider, for example, the jet-to-freestream dynamic pressure ratio which, using \bar{L} , can be written as

$$\frac{q_j}{q_\infty} = \frac{1}{4\pi} = \frac{f(\theta; \beta)}{\int_0^\pi f(\theta; \beta) \sin\theta \cos\theta d\theta} \quad (10)$$

where q_j is the jet core dynamic ratio. This ratio, which occurs in the pressure balance across the contact surface, play a dominant role in locating this surface as can be shown by writing a differential equation for this surface.⁽¹⁴⁾ Therefore, the plume contact surface may be compactly expressed in terms of the two parameters \bar{L} and $C_F/C_{F_{\max}}$ (or D/T) as suggested by Jarvinen and Hill.

Preparatory to selection of the test conditions for the HAPRAP in wind tunnels M and D, Norman, Kinslow, and Lewis⁽²¹⁾ noted that engine efficiency has an important influence on the structure of the inviscid plume contact surface. While their discussion is based on a particular choice of a one-parameter function, $f(\theta; \beta)$, they concluded that this parameter plays an important role in the plume geometry and used it in designing the model rockets. The relation between $C_F/C_{F_{\max}}$, the engine area ratio, A_e/A^* , and the ratio of specific heats, γ_j , is shown in Figure 4. Generally, for larger A_e/A^* and γ_j , the engine efficiency is higher.

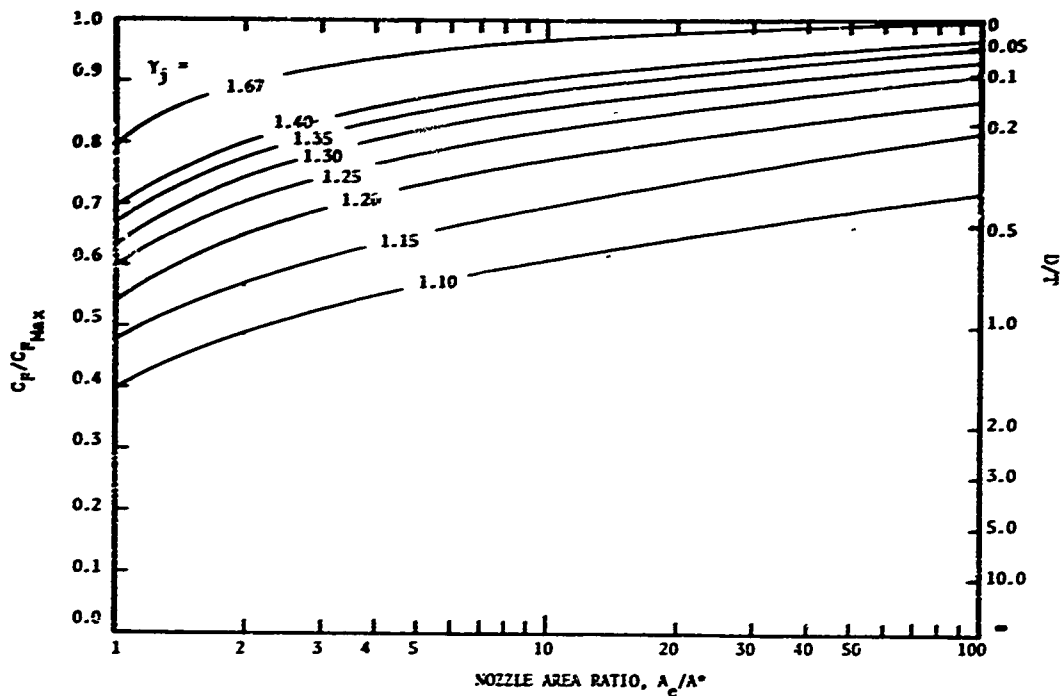


Figure 4 - The Nozzle Efficiency and Plume Drag-to-Thrust Ratio as a Function of Engine-Area Ratio and Ratic of Specific Heats

The particular dependence on D/T used in the universal model is determined from plume momentum balance considerations. It is assumed that plume dimensions are proportional to the products of scaling parameters raised to the proper exponents. It is further assumed that the plume contact surface has a maximum transverse dimension y_{\max} located at finite axial distance x_{\max} downstream of the nozzle exit. These dimensions are thus expressed as

$$y_{\max} = \text{constant} \left(\frac{D}{T} \right)^a \left(\frac{T}{q_{\infty}} \right)^b \quad (11)$$

$$x_{\max} = \text{constant} \left(\frac{D}{T} \right)^c \left(\frac{T}{q_{\infty}} \right)^d \quad (12)$$

The plume drag is written

$$D = C_D q_\infty \pi y_{\max}^2 \quad (13)$$

where C_D is the drag coefficient. For slender axisymmetric bodies in hypersonic flow

$$C_D \propto \tau^2 \quad (14)$$

where the plume slenderness, τ is

$$\tau = \frac{y_{\max}}{x_{\max}} \propto \left(\frac{D}{T}\right)^{a-c} \left(\frac{T}{q_\infty}\right)^{b-d} \quad (15)$$

Equations (11) through (15) then yield

$$D \propto \left(\frac{D}{T}\right)^{2(2a-c)} \left(\frac{T}{q_\infty}\right)^{2(2b-d)} q_\infty \quad (16)$$

Both sides of this equation are compatible only if

$$2(2b - d) = 1 \quad (17)$$

and

$$2(2a - c) = 1 \quad (18)$$

Equation (17) is consistent with the $(T/q_\infty)^{1/2}$ scaling already determined. On the basis of earlier work, Jarvinen and Hill assume that axial scaling is independent of D/T so that $c = 0$ and $a = 1/4$. Their universal model shock and interface shapes are then obtained from a numerical solution at one set of operating conditions

and reduced to universal curves by this scaling. Even with strongly hypersonic external flow, it is incorrect to exactly scale the outer shock using only these two parameters, however, this scaling appears to be quite useful and is the most compact and efficient scaling presently available.

Jarvinen and Hill⁽¹⁹⁾ also present plume densities and pressures within the contact surface which are based on numerical results by the method of characteristics. However, a number of other flow models are available for predicting these properties in the undisturbed jet core; furthermore, the development of these properties based on inviscid flow does not account for mixing in the shock layer. The introduction of transport phenomena constitutes a new phase in the development of simple, analytic high-altitude plume models, since the existing models are unable to provide realistic thermodynamic conditions in the viscous mixing layer.

1.2 LIMITATIONS OF THE HYPERSONIC, INVISCID PLUME

The strength of the Jarvinen-Hill model lies in its efficient use of scaling and the ultimate determination of curve shapes from numerical solutions. The weaknesses of this model result from the particular simplifications used.

1.2.1 Inviscid Flow

Spatial Extent of Strongly Hypersonic External Flow

Because Jarvinen and Hill assume strongly hypersonic external flow throughout the plume, application of their model must be limited to those regions of the plume where the inclination of the contact surface relative to the freestream is relatively large compared to M_∞^{-1} . This criterion may be examined by use of the Jarvinen-Hill model in specific calculations to establish a rough guideline for the spatial extent of the model validity. Consider the pressure distribution on the plume contact surface, as given by Newtonian theory, with the inclusion of both dynamic and static pressure terms

$$p_{\text{body}} = 2q_\infty \sin^2 \sigma + p_\infty \quad (19)$$

where σ = local plume contact surface inclination relative to the freestream flow. For a small σ the ratio of the freestream static pressure to the pressure along the contact surface is

$$\frac{p_{\infty}}{p_{\text{body}}} = [1 + (\gamma_{\infty} M_{\infty}^2 \sigma^2)]^{-1} \quad (20)$$

For a typical ICBM with $D/T = 1/6$, the Jarvinen-Hill model shows $\sigma \sim 11^\circ$ at $\bar{x} = 1$ (see Figure 2 of Reference 19). If the vehicle of interest is moving at 3 km/sec at 160 km ($M_{\infty} = 4.8$), then only about one half (57%) of the surface pressure at $\bar{x} = 1$ is due to the dynamic term. For a speed of 6 km/sec at 200 kilometers, the dynamic contribution to pressure is about 75%. Below 150 km, the dynamic contribution at $\bar{x} = 1$ tends to increase with decreasing altitude since the speed of sound decreases faster than the vehicle speed, down to 80 to 100 km. As a general rule, the Jarvinen-Hill plume model may introduce errors in estimates of the shock layer locations for typical trajectories at distances appreciably greater than one hypersonic scale length, $(T/q_{\infty})^{1/2}$, downstream from the missile.

Thus this model, as well as those of Albini and Hubbard applies only to the forward region of the plume. Fortunately this is the most important flow region from the standpoint of studying most plume radiation phenomena.

The Parabolic Nose

The plume models discussed here assume the contact surface has a blunt nose preceded by a strong detached shock. This implies that the missile body is sufficiently small to cause negligible disturbance to the plume outer shock and that nozzle exit pressure is very large compared to both dynamic and static freestream pressures. Both these requirements tend to form a lower altitude bound for the validity of the model in predicting shock structure.

Missile Body Shocks

When the missile body protrudes ahead of the detached outer shock produced by the plume, significant vehicle influence on the flow in the outer shock layer is expected. If we assume that the detached outer shock is not disturbed when the body length is equal to or less than the shock detachment distance, a rough criterion can be formed for evaluating this plume shock disturbance.

At high altitudes, the plume shock layer density is low and is characterized by relatively slow chemistry, yielding a moderate compression low ratios across the shock as $\gamma_\infty > 1.4$. This leads to a fairly-large shock standoff distance. Using Lighthill's⁽²²⁾ estimate of shock standoff distance for flow about spheres, as a function of shock compression ratio, it appears that typical missile plume standoff distances are ~10% of the detached shock nose radius given by Equation (4). Therefore, we assume that the plume outer shock is disturbed by the vehicle when the missile length, ℓ_m , is equal to the shock standoff distance,

$$\ell_m > 0.1 R_s \quad (21)$$

The freestream density altitude at which this condition is met is

$$\rho_\infty \approx 4 \times 10^{-3} \left\{ \frac{P_c}{u_\infty^2 (\ell/d^*)^2} \right\} \frac{D}{T} \quad (22)$$

where P_c = chamber pressure, u_∞ = freestream speed, and (ℓ_m/d^*) = missile-length-to-engine-throat-diameter ratio.

For an Atlas missile with $P_c = 5 \times 10^6 \text{ N/M}^2$ ($\approx 750 \text{ psia}$), $D/T \sim 1/6$, $u_\infty = 3 \text{ km/sec}$, and $\ell_m/d^* \sim 80$, the lower altitude limit for an undisturbed detached bow shock is $\sim 110 \text{ km}$ ($\rho_\infty \sim 6 \times 10^{-8} \text{ Kg/m}^3$) using the U.S. Standard Atmosphere⁽²³⁾. Jarvinen and Dynen⁽¹³⁾ reported wind tunnel studies in which

the bow-shock structures retained their blast wave geometry even in cases where the body was larger than the shock nose radius. However, on the basis of the present criterion, their statement that the Jarvinen-Hill plume model applies for altitudes as low as 30 km appears unwarranted. For example, a 10^5 lb thrust vehicle, with $D/T = 1/6$, moving at 2 km/second at 30 km would have a $(D/q_\infty)^{1/2}$ of 1.33 meters and an outer shock nose radius $R_s \sim 0.5$ meters. Not only is this shock nose radius smaller than the body length, but it is probably only a fraction of the body diameter. Therefore, when applying the Jarvinen-Hill plume model, it should be kept in mind that the missile body may have significant influence at altitudes below 100 km, and that below 40 to 50 km, the usefulness of such a model is in considerable doubt. Several studies of the outer shock layer structure have been conducted in which these altitude and flight conditions have been considered. A recent study by Erlich and Fong,⁽²⁴⁾ which examined the interaction of body geometry and plume flow, is indicative of the present state of the art.

The Contact Surface: Blunt and Not So Blunt

The possibility that the plume forward flow structure may collapse into a pointed body with an attached shock is a more severe limitation on plume models. Detachment of plume outer shock clearly has an important effect on plume nose geometry, and has been touched upon by Albini⁽¹⁵⁾ and Thompson et al.⁽¹⁸⁾ For flight Mach numbers in excess of 5 or 6, the maximum semi-vertex angle for which a shock remains attached to a right circular cone is nearly constant at 57° for $\gamma_\infty = 1.4$.⁽²⁵⁾ Shock attachment conditions for flow over cones offers a convenient criterion for estimating limits for the validity of those plume models which assume a detached outer shock. This criterion is used below to estimate the altitude below which the plume outer shock becomes attached, thereby exceeding the limits of applicability of the Jarvinen-Hill model.

A simple criterion for plume outer shock attachment has been suggested by Plotkin and Draper⁽²⁶⁾. They determined the initial angle of the contact surface at the nozzle lip by balancing external pressure, determined by the Newtonian approximation, and internal pressure, determined from the Prandtl-Meyer function.

The shock was assumed to be detached when this angle reached 57° . Their calculations have been extended here to a larger range of engine area ratios, altitudes, and specific heat ratios as illustrated in Figure 5. In this figure, for a given missile, there exists a horizontal line of constant engine area ratio, A_e/A^* as the missile gains altitude. The outer shock remains attached until this horizontal line intersects the curve labeled with the appropriate value of engine specific heat ratio, γ_j . This intersection occurs at 260 km for a missile with $A_e/A^* = 60$ and $\gamma_j = 1.3$. It should be noted that a missile speed of 3 km/sec, a chamber pressure of 6.9×10^6 NT/M² (1000 psia), and a non-divergent nozzle exit have been assumed in constructing Figure 5.

From Figure 5, it appears that, for existing ICBM's, the outer shock is detached for altitudes above 80 to 120 km. This conclusion is supported by observations of plume nose-radii (Hill and Habert)⁽¹⁰⁾ which are shown in the upper right-hand corner of Figure 2. In these observations, the largest deviations from the blast wave prediction occur at the lowest altitudes and where the blast wave theory, which predicts a blunt nose, might be inapplicable.

A significant conclusion to be drawn from Figure 5 is that a special class of high area ratio, high specific heat ratio rocket engines characterized by very slender plumes appears to exist. Due to the very narrow jet flow distribution characteristic of such engines, the current blunt-nosed plume models would overestimate their nose radii. Even at

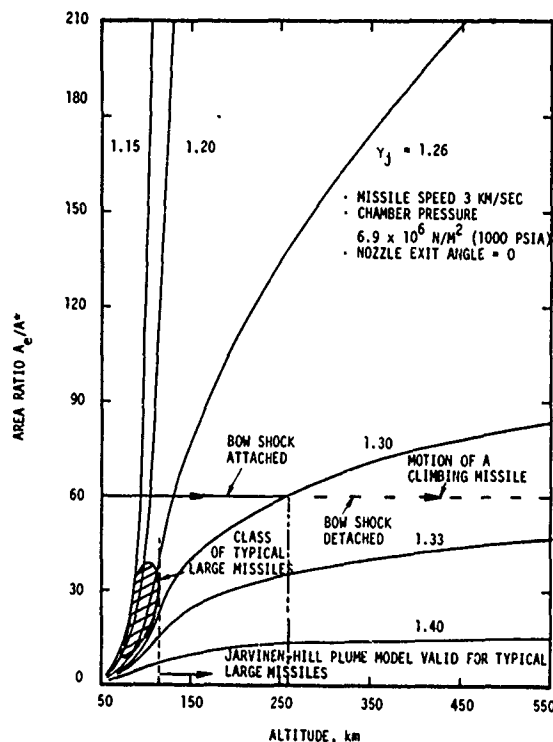


Figure 5 - Shock detachment altitude

very high altitudes, the maximum inviscid expansion from these engines (here neglecting nozzle boundary layer flow⁽²⁷⁾) is insufficient to cause plume outer shock detachment. Care should be taken, however, in using inviscid flow concepts, since relatively low Mach numbers in the nozzle boundary layer allow for a larger Prandtl-Meyer turning angle at the nozzle lip. With the present criterion, we suggest that for this class of engines, having large engine area ratios and large ratios of specific heats, exhaust plumes may be relatively sharp-nosed hypersonic bodies.

The Jarvinen-Hill model describes blunt-nosed plumes generated by engines with nozzle efficiencies characteristic of typical ICBM's (i.e., $C_F/C_{F_{max}}$ approximately 0.8 to 0.9 and plume

drag-to-thrust ratios of about 0.11 to 0.25). This model does not apply to sharp-nosed plumes from high-efficiency (i.e., low D/T) nozzles.

Figure 5 together with Equation (3) suggest a correlation of shock detachment altitude with D/T which is illustrated in Figure 6 where the nozzle efficiency is plotted against the altitude at which shock attachment occurs.

This presentation results in a natural division between blunt-nosed plumes ($C_F/C_{F_{max}} < 0.92$ or $D/T > 0.08$), and sharp-nosed plumes ($C_F/C_{F_{max}} > 0.92$ or $D/T < 0.08$) in the altitude range of interest. The flight regime below and to the right of the shock detachment curves is suitable for application of the Jarvinen-Hill model. The plumes in the flight regime

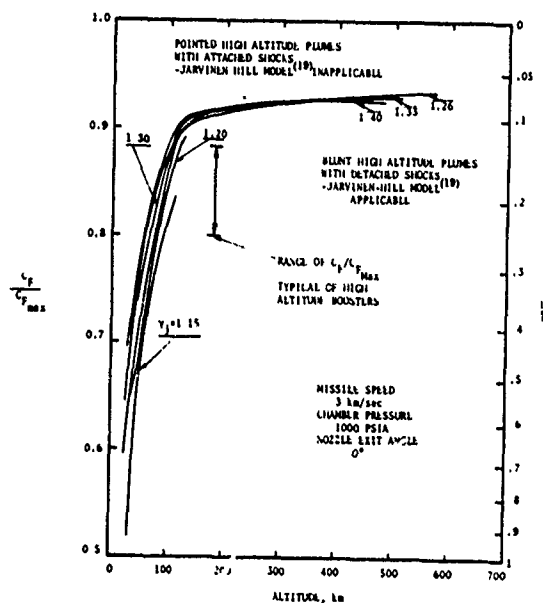


Figure 6 - Correlation of Plume Nose Shape with $C_F/C_{F_{max}}$

to the left and above these curves are not presently described by any available models. Note that these regimes shift somewhat with engine design and trajectory. They should be recalculated for individual missiles and trajectories which deviate markedly from the nominal conditions shown in Figures 5 and 6.

Longitudinal Internal Scaling

With arguments based strongly on the blast wave theory of Sedov⁽²⁸⁾ and Taylor,⁽²⁹⁾ Hill and Habert⁽¹⁰⁾ developed longitudinal and transverse plume scaling parameters incorporated in the universal plume model of Jarvinen and Hill⁽¹⁹⁾ as

$$\hat{x} = x(q_{\infty}/T)^{1/2} \quad (23a)$$

and

$$\hat{y} = y [q_{\infty}/(TD)]^{1/2} \quad (23b)$$

respectively. The considerable success of this scaling apparently comes from the fact that the dominant length scale in both x and y for highly underexpanded plumes in strongly hypersonic streams is $(T/q_{\infty})^{1/2}$, which was shown to be appropriate by purely dimensional arguments.⁽¹⁴⁾ The transverse dimension is distorted also by the parameter $(D/T)^{1/4}$ as is seen by rearranging Eq. (23b) as $\hat{y} = y(q_{\infty}/T)^{1/2} (T/D)^{1/4}$. This very weak dependence upon a parameter which does not vary greatly for engines of practical interest is the only additional scaling provided by the blast wave analogy. The analogy itself is extended beyond its limits of validity when applied to relatively blunt regions of the plume nose radius. The scaling given in Equations (23) is examined here in the limit of very small D/T where the exact scaling is known.

The dominant scaling parameter for both axial and transverse plume dimensions is $(T/q_{\infty})^{1/2}$ for highly underexpanded plumes in strongly hypersonic

streams. If the rocket nozzle is limited to only those with hypersonic exit conditions (equivalent to small D/T as shown below), the hypersonic slender body theory of van Dyke⁽³⁰⁾ applies to the flow within the plume, yielding a scaling in exit Mach number, M_e , and (T/q_∞) as

$$\tilde{x} = x (q_\infty/T)^{1/2} M_e^{-1} \quad (24a)$$

and

$$\tilde{y} = y (q_\infty/T)^{1/2} \quad (24b)$$

with no explicit form for the dependence of scaling upon γ_j . Clearly, the scaling of Jarvinen and Hill fails in this limit, since Equations (24) show that, at least for fixed γ_j , transverse dimensions are unaffected by changing D/T (through changes in M_e) at fixed (T/q_∞) . Equations (24) show the familiar longitudinal stretching with M_e which is absent from Equations (23).

The plume fineness ratio, or ratio of transverse to longitudinal scales, predicted by these equations can easily be examined in the limit of $M_e \gg 1$ since D/T reduces to

$$D/T = (C_{F_{\max}}/C_F) - 1 \approx (\gamma_j - 1)^{-1} M_e^{-2} \quad (25)$$

Thus Equations (23) become, in this limit,

$$\hat{x} \approx x (q_\infty/T)^{1/2}$$

and

$$\hat{y} \approx y (q_\infty/T)^{1/2} (\gamma_j - 1)^{1/4} M_e^{1/2} \quad (26)$$

yielding a plume fineness ratio of

$$\tau \propto (\gamma_j - 1)^{-1/4} M_e^{-1/2} \quad (27)$$

whereas Equations (24) yield the proper theoretical limit

$$\tau \propto M_e^{-1} \cdot f(\gamma_j) \quad (28)$$

where $f(\gamma_j)$ is an unspecified function.

This development shows that the universal plume model of Jarvinen and Hill, which contains a very weak D/T scaling dependence, does not yield the proper limiting forms for longitudinal or transverse scaling or their ratio when D/T is very small. It is not meaningful to attempt an evaluation of their model for large D/T since, for a sonic nozzle with $\gamma_j = 5/4$, D/T is only 2.0. Therefore, the model is confined to a D/T range somewhat smaller than unity, where $(D/T)^{1/4}$ varies only slightly.

Description of the viscous layer between the jet and freestream gases has been a major concern in high-altitude rocket radiation studies. The discontinuities in velocity and total enthalpy along the plume interface in inviscid theory must be replaced by smooth property profiles in the actual situation with transport phenomena included. As the missile climbs it moves faster in a hotter and less dense atmosphere, and the freestream mean free path increases in relation to the plume scale, consequently the portion of the flowfield dominated by these transport processes grows. At still higher altitudes, non-continuum or rarefaction effects must be considered. In this section, we make a somewhat artificial separation of these effects and discuss continuum, viscous processes; rarefaction effects are discussed in Section 5. For the low densities considered here, the laminar character of mixing layers should be insured by the very small Reynolds numbers ($\leq 10^4$).

Vasiliu⁽³¹⁾ was among the first to consider the viscous region in jet plumes at lower altitudes, where turbulent flow occurs in mixing layers. Using the boundary layer equations with a streamwise pressure gradient, he considered chemical production and heating in this layer. Thompson⁽¹⁸⁾ later extended the study by including effects of traverse pressure gradients. Recently Tannehill⁽³²⁾ and Fannehill Anderson⁽³³⁾ studied the turbulent mixing layer for intermediate altitudes using a modification of the MULTI-TUBE⁽³⁴⁾ finite difference program to include chemical reactions. They concluded that the chemistry proceeds so slowly at intermediate and high altitudes (> 50 km) as to be unimportant in determining thermodynamic properties in the mixing layer. Calculations are being extended to high altitudes by Boynton⁽³⁵⁾ using the MULTI-TUBE program.

The inviscid plume models provide no information on either the viscous layer dimensions or thermodynamic properties. The inner shock layer properties presented in the Jarvinen-Hill model are based on (inviscid) calculations by the method of characteristics.

In such calculations, the jet gas flow along the contact surface has undergone a nearly isentropic compression whereas jet gas which enters the inner shock layer further downstream passes through an increasingly stronger shock with increasing entropy rise. This entropy variation and the centrifugal pressure gradient lead to rapidly increasing densities toward the contact surface while the static temperature profile remains comparatively flat. In high-altitude plumes with strongly hypersonic external flows, mixing of the cold inner shock layer with the hot outer shock layer and dissipation should substantially increase mixing layer temperatures and reduce jet gas densities below the prediction of the Jarvinen-Hill model.

The Jarvinen-Hill model⁽¹⁹⁾ offers a useful form for reducing plume mixing layer measurements. By making a mass balance in the inner shock layer, they obtain a reduced density

$$\frac{\bar{\rho}}{\rho} = \frac{\rho_{sl} (g_{lsp})^2}{2q_{\infty}} \left[\frac{C_{Fmax}}{C_F} \right]^2 \quad (29)$$

where ρ_{sl} = the inner shock layer density and $gl_{sp} = c_{eff}$, the effective engine speed. Using $T = \dot{m} c_{eff}$ and $(a_o/u_{lim})^2 = (\gamma_j - 1)/2$, their reduced density can be rewritten as

$$\bar{\rho} = \left(\frac{\gamma_j}{\gamma_j - 1} \right) \left(\frac{1}{CFA^*} \right) \frac{a_{sl}}{\rho_c} \bar{L}^{-2} \quad (30)$$

where the subscript c refers to engine stagnation conditions. This form is useful for the HAPRAP mixing layer data analysis as it includes the inviscid parameters (chamber conditions, hypersonic scale, and engine geometry) which control the mixing layer densities.

We now look at the parameters controlling mixing layer dimensions in cases where viscous effects are significant but do not dominate plume structure. An inviscid aerodynamic theory may predict plume characteristics accurately only if the viscous shear layer between exhaust and ambient gas is thin compared to the distance from this layer to inner or outer shocks. A study of a criterion for inviscid flow for blunt body flow can be based on the order of magnitude arguments from Hayes and Probstein⁽²⁶⁾. For hypersonic flights of rockets with moderately thick exhaust plumes, the thickness of the shear layer at the plume boundary (δ) is ordered as

$$\delta \cong \left[\frac{\mu \bar{L}}{\epsilon^{1/2} \rho u_\infty} \right]^{1/2} = \left[\frac{\mu}{\mu_\infty} \frac{\theta}{\theta_\infty} \frac{p_\infty}{p} \frac{\bar{L}^{-2}}{\epsilon^{1/2} (Re \bar{L})^{-1}} \right]^{1/2} \quad (31)$$

where $\epsilon = (\gamma_\infty - 1)/(\gamma_\infty + 1)$; μ , θ , and p are representative values of viscosity, temperature, and pressure in the shear layer, and Reynolds number is based on stream conditions and hypersonic plume length, $\bar{L} = (T/q_\infty)^{1/2}$. The distance, Δ , from the shear layer to the plume outer shock is typically

$$\Delta \cong \epsilon \bar{L} \quad (32)$$

By simple arguments based on the kinetic theory, Knudsen number (Kn_L) is related to stream Reynolds number (Re_L) as

$$Kn_L \equiv \frac{\lambda_\infty}{L} \propto M_\infty (Re_L)^{-1} \quad (33)$$

where λ_∞ is the freestream mean free path. If the temperature dependence of viscosity is approximated by $\mu \propto T^{3/4}$ and if hypersonic shock relations are used to order pressure and temperature as

$$p/p_\infty \propto M_\infty^2; \quad \theta/\theta_\infty \propto M_\infty^2 \quad (34)$$

then Equations (31) through (33) combine to yield the ratio of shear layer thickness to shock layer thickness

$$\delta/\Delta \propto \epsilon^{-3/8} Kn_L^{-1/2} M_\infty^{1/4} \quad (35)$$

Continuum flow is assured if the ratio of mean free path, λ , to relevant flow dimensions is sufficiently small in all disturbed parts of the flow field. Here we consider the region between the bow shock and the shear layer where the appropriate ratio is λ/Δ . However, λ/λ_∞ is of the order of $\epsilon M_\infty^{1/2}$ with the above viscosity temperature relation, thus

$$\lambda/\Delta \propto (\lambda_\infty/L) \epsilon^{5/4} M_\infty^{1/2} \propto Kn_L M_\infty^{1/2} \quad (36)$$

The inviscid flow theory is only valid for very small values of both λ/Δ and δ/Δ . The latter criterion is clearly more stringent. The weaker criterion of very small λ/Δ , which insures continuum flow but not inviscid flow, is satisfied by typical rockets to much higher altitudes than the first criterion. Failure of the inviscid flow criterion results in substantial cross diffusion of ambient and exhaust gases and thickening of the mixing layer structure. The

impact of viscous effects on inviscid theories for plume structure predictions cannot be assessed quantitatively at this time, however, present measurements should be applied with considerable caution in any comparative evaluation of inviscid plume theories.

In conclusion, inviscid plume models cannot adequately express the mixing layer conditions so that chemical-radiative calculations can be carried out. However, the inviscid calculations supply a technique for mixing-layer data reduction such that viscous phenomena effects are more easily studied. Moreover, within the moderate range of flight Mach numbers of interest, it appears that the prime parameter for describing the viscous-rare fraction development of the freestream-jet interface region under study is the plume Knudsen number.

1.3 AREAS FOR IMPROVEMENT IN THE PLUME MODEL

The principle areas for improving present plume models fall into two general groups: inviscid and viscous. It is useful to preserve the assumption of strongly hypersonic external flow since, as has been mentioned, the radiating region occurs in the forward blunter region of the plume where Newtonian theory applies for most cases of interest (i.e., flight Mach Numbers $\sim 6-10$). Therefore, we consider that the plume structures of interest are located within one hypersonic scale length of the missile $\bar{x} < 1$.

Inviscid Effects

To insure the validity of the simplified far field form for the undisturbed jet core, the plume body must be small compared to the flow scale. This condition seems to be met according to the fairly conservative criterion represented by Equation (21).

Although present ICBM's satisfy the criterion for blunt plume noses with detached outer shock at altitudes above 80 to 120 km, classes of vehicles and ranges of operating conditions appear to be feasible for which the plume structure would be slender at all altitudes of interest. Present plume models should be extended to allow for such slender geometries.

The failure of the Jarvinen-Hill model to provide proper scaling in the limit of hypersonic nozzle exit flow can be remedied by incorporating the proper scaling given in Equation (24). This is especially important for $C_F/C_{F_{\max}} > 0.90$ ($D/T < 0.10$), not for the general case. Some HAPRAP data will be used to study plume scaling for hypersonic nozzle exit conditions.

Viscous Effects

The simple plume models provide essentially no information about viscous plume structure. In the present work, HAPRAP measurements are coupled with theoretical considerations to develop a better understanding of viscous effects in plumes. The primary regions of interest are:

1. Development of parameters basic to description of the viscous mixing layer;
2. Assessment of the degree to which HAPRAP experiments simulate viscous structure in the high altitude plumes,
3. Determination of the relevance (if any) of inviscid plume models (e.g., the hypersonic scale and dimensions) in viscous plumes.
4. Examination of the HAPRAP measurements of viscous mixing layer structure to establish which features display the influence of viscous parameters and which provide inputs to the ultimate task of analysis of plume chemistry and radiation;
5. Formulation, based on previous work and on the HAPRAP measurements, of density regimes which distinguish qualitatively different plume features, for use as a guide to calculations and field data analysis.

Section II

VALIDATION OF THE MEASUREMENTS

The validity of the HAPRAP plume structure studies is examined in this section. Considerable attention to validation has already been given in connection with data reduction in the work of Norman, Kinslow and Lewis,⁽²¹⁾ Smithson, Prince and Whitfield⁽³⁷⁾ and Price, Powell and Moskalik.⁽³⁸⁾ The purpose here is not to reexamine their experimental techniques but rather to consider the HAPRAP data with a view of verifying and upgrading the hypersonic plume models discussed in Section 1. This view may ascertain whether certain HAPRAP measurements which do not support present hypersonic plume models point to experimental limitations or to the occurrence of additional phenomena not accounted for by the models.

The goals and methods of the HAPRAP study are described below. There follows studies of gas dynamic aspects of the measurements and electron beam techniques. The final section briefly summarizes this data validation study.

2.1 THE HAPRAP MEASUREMENTS: PURPOSE, TYPE, SCOPE

The principal goal of the HAPRAP (plume-freestream interaction) wind tunnel studies is to obtain information about the viscous interaction region between the freestream gas and engine exhaust species. These objectives are⁽³⁹⁾ to:

1. Determine the effect of altitude on the size, location and gas-dynamic characteristics of the mixing layer between the exhaust jet and the freestream.

2. Establish criteria for predicting where continuum flow models become inadequate due to rarefaction effects.
3. Study the wind tunnel simulation of high altitude rocket plumes.

In these studies the wind tunnel formed a primary supersonic or hypersonic freestream in which a secondary plume flow was immersed. The interaction between the two flows was studied by the pitot probe surveys and electron beam fluorescence recorded qualitatively in flow visualization photography and quantitatively for each gas species using a filter-photomultiplier-ammeter-recorder package. The experimental setup is schematically represented in Figure 7. The separate experimental arrangements for each facility (wind tunnels M, D and ASC(10V)), the data acquisition processes, and the calibration procedures are described in References 21, 37 and 38.

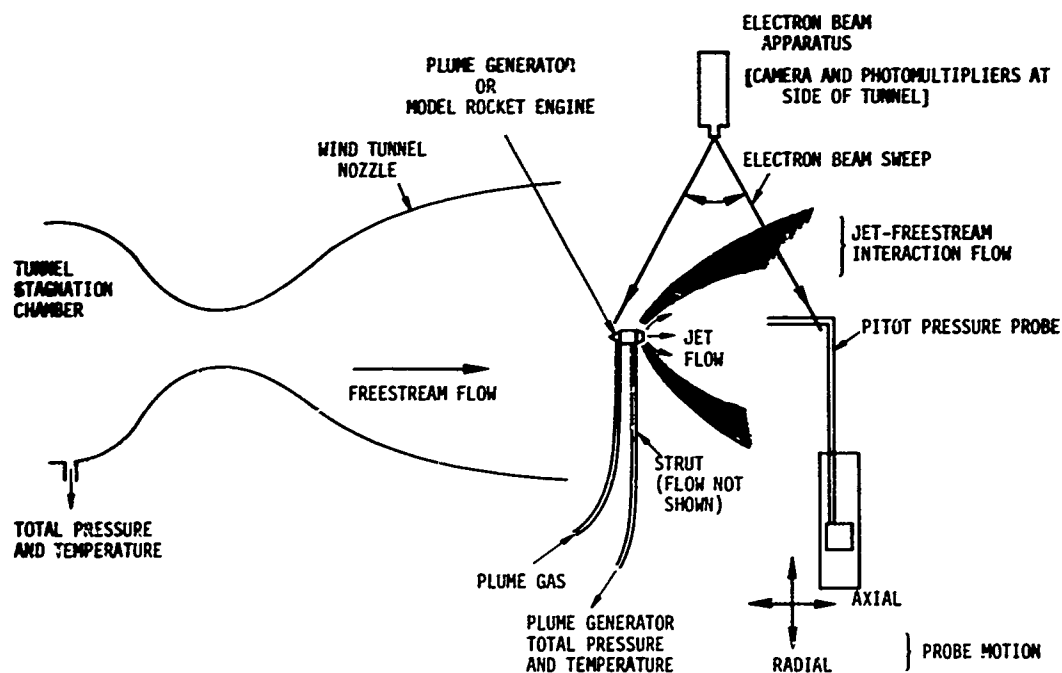


Figure 7 - Jet-freestream interaction experiment setup for the high altitude plume radiation program (HAPRAP).

The influence of relevant boost phase missile parameters on plume properties was studied by varying each parameter separately. Seven sets of experimental conditions were selected for tests in tunnels M and D, to determine the effects of D/T , (T/q_∞) and jet gas specific heat ratio on plume properties, and to attempt to simulate major plume features for a specific flight situation. With the same objectives, a much more extensive study (~ 100 separate runs) was conducted in the Aerospace Chamber 10V, ASC (10V), over broad ranges in nozzle stagnation pressure and stream dynamic pressure. In these studies the nozzle axes were oriented coparallel with, perpendicular to and opposed to the freestream. The combined tests covered a range of two orders of magnitude in plume Knudsen numbers extending from fully continuum flows to flows well within the transitional regime.

2.2 GASDYNAMIC EFFECTS

Gasdynamic phenomena which may disturb the simulation sought in the HAPRAP studies are examined. Nonisentropic processes such as condensation and freezing of internal energy, and disturbances associated with wind tunnel testing are perhaps the most important areas of examination. These and other effects are discussed below.

Gas Condensation

Condensation of jet gases within the nozzle and the undisturbed jet core may significantly affect the plume structure. Estimates of the degree and effects of condensation are difficult due to limited available measurements. Of the three jet gas species (He, Ar, CO_2) used in the HAPRAP studies CO_2 will condense most readily. Consequently only CO_2 is considered in the present discussion.

Condensation is possible when the vapor becomes super-saturated. However, the rate of condensation is limited by the rate of formation of nuclei (clusters of a size suitable to growth). The nucleation rate, or nuclei formed per unit volume per unit time, is⁽⁴⁰⁾

$$J = \left(\frac{p}{k\Theta}\right)^2 \frac{m}{\rho_L} \left(\frac{2\sigma}{\pi m}\right)^{1/2} \exp\left[-4\pi\sigma(r')^2/3k\Theta\right] \quad (37)$$

where

p = gas pressure
 ρ_L = liquid density
 M = molecular wt.

$$r' = \frac{2m\sigma}{\rho_L k\Theta \log(p/p_v)} \quad (38)$$

where p_v is the flat film vapor pressure of the liquid at Θ .

As J is very sensitive to σ , and to gasification corrections not included in Equation (37), it is not feasible to predict the condensation rate a priori, but Equation (37) may be used to extrapolate available data.⁽⁴¹⁾ Thus, assuming σ and ρ_L are constants, the necessary p/p_v to produce a constant nucleation rate, as T is varied, can be found from Equation (37) as,

$$\log \frac{p}{p_v(\Theta)} = - \frac{C_2}{\Theta^{3/2} [\log J/\rho - \log C_1]^{1/2}} \quad (39)$$

where ρ is gas density.

If we assume the onset of condensation occurs at a certain value of J/ρ then the pressure for onset of condensation is given as a function of temperature by Equation (39). This relation is used to extrapolate the data of Duff⁽⁴¹⁾

to yield the broken line in Figure 8. Also shown in Figure 8 are isentropes corresponding to two HAPRAP runs with CO_2 as the jet gas, which cross the curve for onset of condensation at jet pressure of order 0.1 psia.

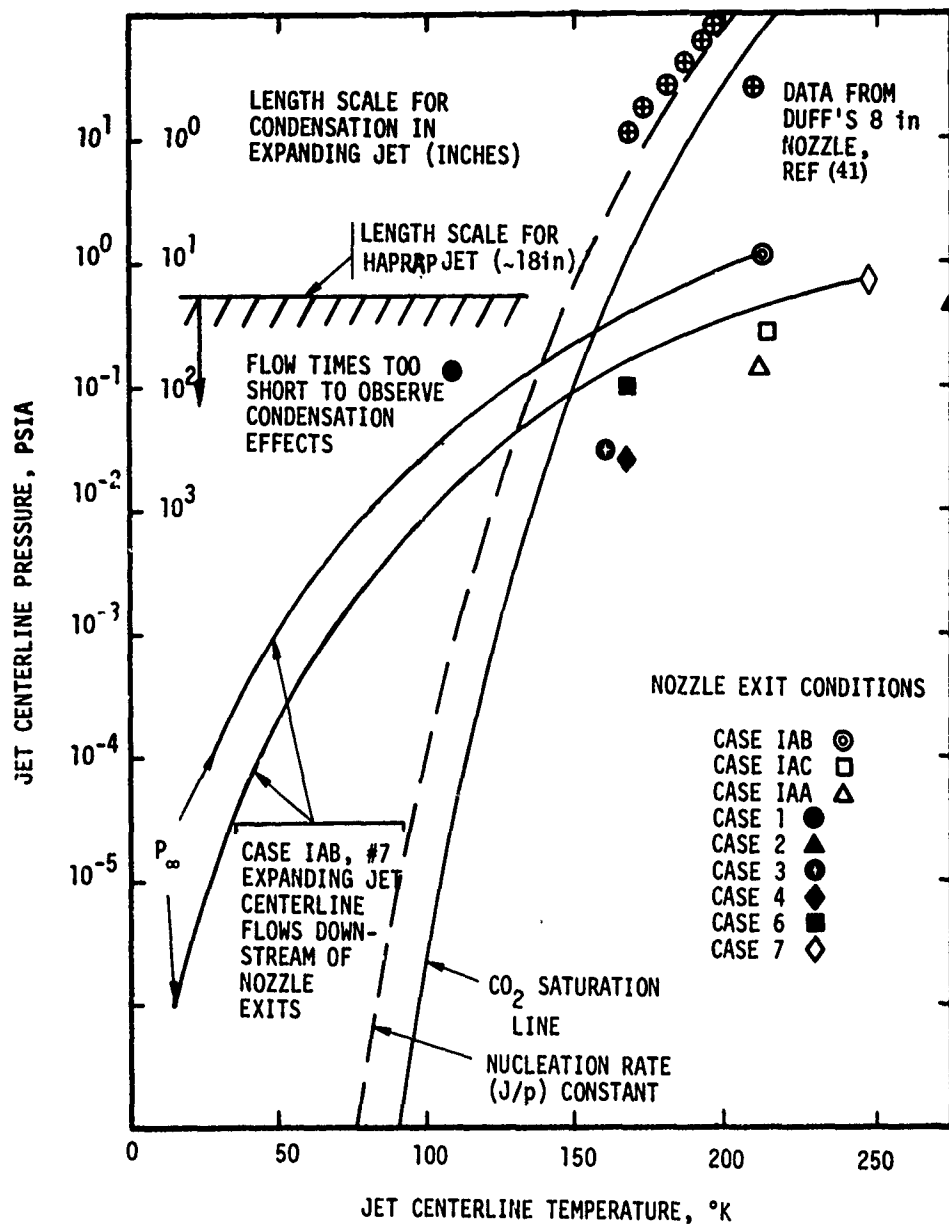


Figure 8 - Evaluation of appearance of macroscopic condensation effects in HAPRAP jets

The occurrence of onset of condensation alone does not indicate significant condensation without a sufficiently rapid droplet growth rate. The theory of droplet growth is subject to uncertainties in the droplet's thermal balance, most of which stem from uncertainty in accommodation coefficients. If we assume that the ratio of drop temperature to vapor temperature is constant, then the droplet radius change as

$$\frac{1}{r} \frac{dr}{dt} = \text{Constant } (T) \left\{ \frac{p}{\Theta^{1/2}} - \frac{p_L}{\Theta_L^{1/2}} \right\} \propto \frac{p}{\Theta^{1/2}} \quad (40)$$

where Θ_L is the droplet temperature and p_L is the vapor pressure over the drop. Thus the time scale for droplet growth is proportional to $\Theta^{1/2}/p$. Typically the square of the jet velocity is proportional to jet stagnation temperature, which for fixed nozzle geometry is proportional to local jet temperature. Thus the length scale for droplet growth is proportional to p^{-1} . Duff's data show significant condensation effects at $p \approx 10$ psia in a length scale of about one inch; this provides the length scale ordinate in Figure 8, which is to be interpreted as the minimum flow field length required in order that condensation effects be noticeable. Nozzle exit conditions are shown in Figure 8 for the HAPRAP coparallel flow CO_2 jets. With the exception of the ASC(10V) facility case No.1 ($\Theta_c = 280^\circ\text{K}$) which will be discussed further, all points lie to the right of the CO_2 saturation line. Consequently for these cases condensation does not occur inside the nozzle. Outside of the nozzle droplet growth rates are sufficiently slow to insure no significant condensation. This is shown by the expansion lines for cases IAB and No. 7, for which the flow time available for drop growth is an order of magnitude too small to allow appreciable effects of condensation in the portion of the flow field examined in

the HAPRAP studies, i.e., within about 14 in. of the jet nozzle. The only HAPRAP case for which the expansion isentrope crosses the saturation line inside the nozzle is case No. 1, where $\theta_c = 280^\circ\text{K}$.

In the HAPRAP data analysis of electron beam fluorescence photographs, shock coordinates were normalized by the hypersonic scale $(T/q_\infty)^{1/2}$. The outer and inner plume shock positions are plotted in these normalized coordinates in Figure 9 for cases No. 1 and 2 in the ASC(10V) facility. These cases have the same nozzle geometry, jet gas, jet stagnation pressure, and plume scale. The principal difference is jet stagnation temperature, for case No. 1, $280^\circ\text{K} < \theta_c < 478^\circ\text{K}$, while for case No. 2 $\theta_c \sim 700^\circ\text{K}$. Our previous consideration in Part I of the hypersonic plume scaling indicated that the shock structures should not depend upon θ_c . However, that development does not include condensation effects which may have existed in case No. 1 according to the arguments above. When the flow condenses within the nozzle the released heat of vaporization lowers the nozzle exit Mach number thus decreasing the nozzle efficiency, $C_F/C_{F\text{max}}$ (increasing D/T), which should result in a broader plume structure. Therefore we might expect a rather abrupt shift in jet dimensions as the nozzle stagnation temperature is decreased to the point where saturation occurs within the nozzle. This may be similar to the retrojet freestream shock jump reported in Ref. (37). On the basis of this analysis the differences in normalized shock locations between cases No. 1 and 2 (Figure 9) are believed to result from the occurrence of significant condensation in case No. 1. We further conclude that condensation is negligible in all other HAPRAP runs.

These conclusions are supported by observations of jet condensation by both Golomb⁽⁴²⁾ and Beylich.⁽⁴³⁾ Golomb observed condensation in CO_2 jets and in Ar jets using a mass spectrometer located behind a cooled skimmer about 10^3 orifice diameters downstream of the nozzle. The source stagnation pressure corresponding to maximum centerline dimer concentration was observed for fixed stagnation temperature. By viewing this maximum as indicative of "massive condensation!" he obtained a plot of nozzle conditions (stagnation pressure vs. temperature) for determining the appearance of

condensation. These "condensation plots," indicated the occurrence of condensation with Golomb's sonic nozzle A, for CO₂ jets, when $\theta_c < 400-500^\circ\text{K}$ with $P_c \sim 20-60$ psia (3×10^3 torr).

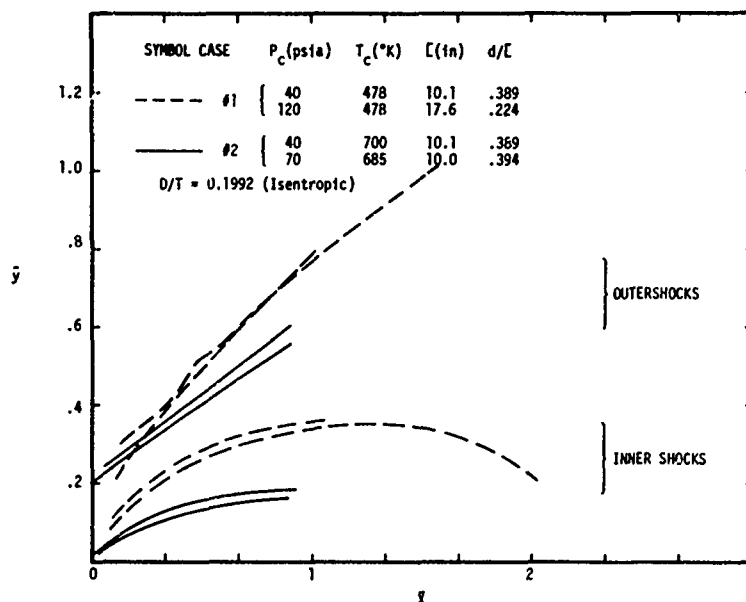


Figure 9 - Shock location dependence upon nozzle chamber temperature.

This point can be developed further using one dimensional condensation calculations presented by Beylich⁽⁴³⁾ which predict condensation to occur when saturation occurs inside his nozzles. This is supported by his measurements where stagnation temperatures ranged from 290 to 495 $^\circ\text{K}$. If Beylich had extended his studies to higher stagnation temperatures, saturation would not have occurred inside the nozzle and the onset of condensation would have occurred in the free jet. Beylich's Figure 8 suggests in this case that no significant condensation would occur in the free jet for stagnation temperatures above about 600 $^\circ\text{K}$.

It is noted that the absence of condensation in the HAPRAP tests is not fortuitous but the result of the nozzle design effort described by Thomas and Stewart.⁽⁴⁴⁾ We conclude that their design goal of avoiding jet condensation has been achieved.

Internal Mode Freezing

Rapid decreases in collision frequency with distance along streamlines in expanding flows results in freezing of internal modes in molecular gases leading to an increase in effective ratio of specific heats which in turn may have a significant effect on plume structure. The plume contact surface is located by a balance between jet and ambient dynamic pressures. Internal mode freezing which typically occurs at large local Mach numbers with little effect on the flow dynamic pressure and so should have little effect on the contact surface location. This is not the case for the shock locations. The vibrational modes remain virtually frozen across the low density, oblique, hypersonic inner shock, thus causing a reduced shock density compression ratio. Occurrence of vibrational mode freezing, therefore, significantly increases the distance from internal shock to contact surface (to accommodate the flow at reduced density in this region) but should have little effect on the contact surface.

Selected pitot probe data have been reduced to jet centerline static pressure versus distance from the nozzle exit. The farfield jet static pressure should vary as $x^{-2\gamma}$. Figure 10 shows the data are closely represented by a straight line, with slope corresponding $\gamma = 1.29$. This value of jet specific heat ratio suggested in Ref. (37) is 1.27. Only a suggestion of gamma shifting appears as a slight dip in the data below the dashed line just upstream of the Mach disc. This small effect appears typical of the HAPRAP runs and such changes in the value of the specific heat ratio will be neglected.

Pitot Probe Calibration

Pitot probe measurements are affected by rarefaction phenomena in the low density flows studied. Norman, Kinslow, and Lewis⁽²¹⁾ have described and carried out the probe rarefaction adjustment and plotted corrected CO_2 and N_2 impact pressure results from tunnels M and D. A low density flow calibration curve for the ASC(10V) pitot probe has been provided by AEDC.⁽⁹⁵⁾ The probe calibration also varies with jet and freestream species mixture ratio as the probe traverses the mixing layer. Determination of the mixing layer conditions

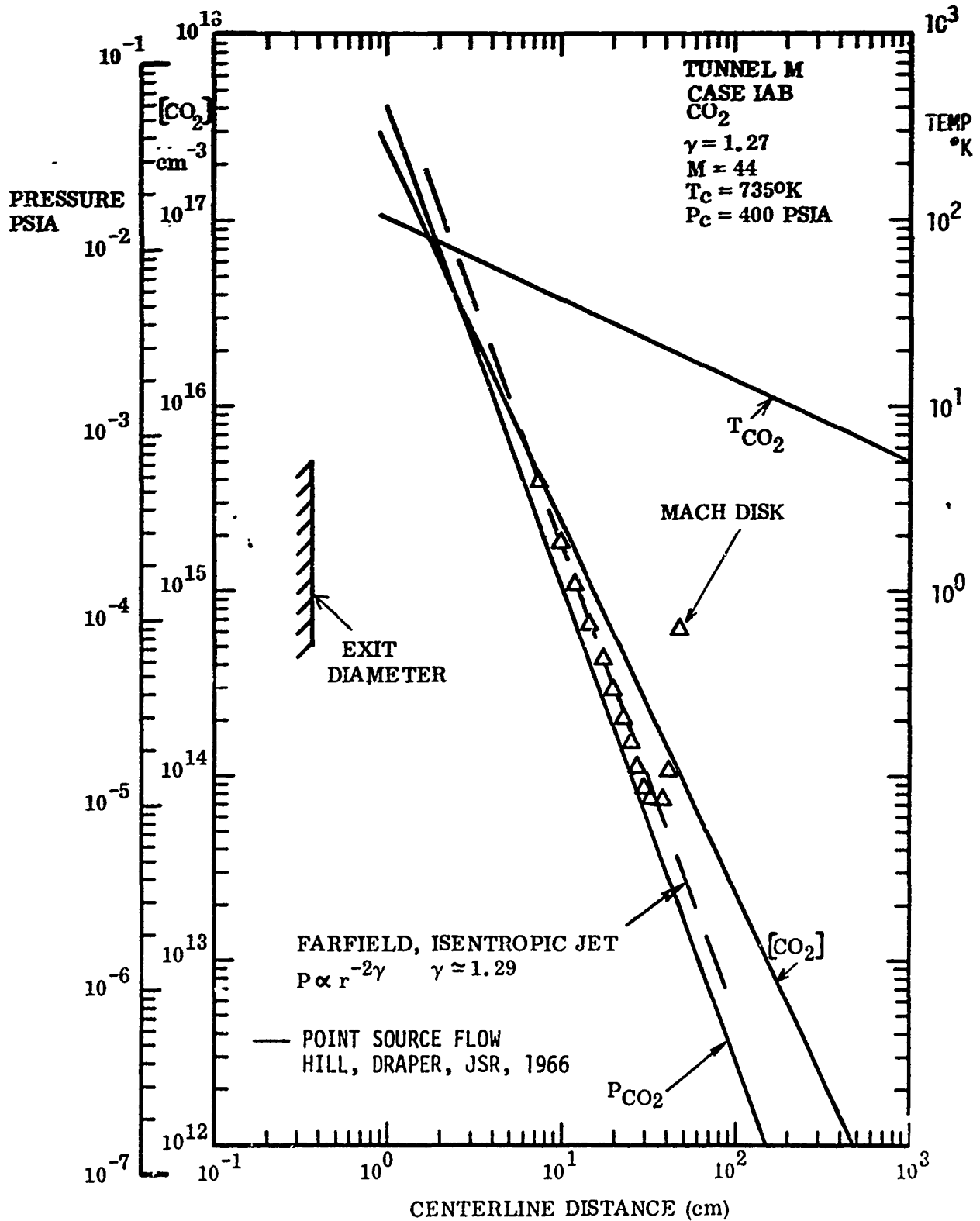


Figure 10 - Pitot probe measurements compared with farfield jet calculations

by pitot probes requires both rarefaction corrections and additional information on the mixture ratio. However, the individual species profiles are also obtained independently via the electron beam species concentration measurements. This latter method is the better one for studying the mixing layer structure and the pitot probe data is used below only to determine shock locations. Hence the pitot probe calibration is not considered further. It should be pointed out that the pitot probe surveys were originally intended as the basic source of flowfield data. Subsequently it developed that the electron beam surveys were far more extensive than originally conceived and can be relied upon to supply the mixing layer flowfield data.

Strut Shock

Model rockets were suspended in the freestream by a strut which generated a disturbed flow on one side of the model plume. Without azimuthal surveys of plume densities the extent of this disturbance is difficult to assess from the data. Certainly the disturbed plume region increases as the freestream Mach number decreases, thus the case No. 1-3 plumes in tunnel ASC(10V), which have the lowest freestream Mach numbers ($M_\infty \sim 3.6$), were most strongly perturbed by strut effects.

Examination of the electron beam flow visualization photographs⁽⁴⁵⁾ for those cases (Nos. 1-3) does not show disturbances caused by the strut on that side of the plume 135° away from the strut azimuthal location (off-strut side of the plume). All the shock locations considered here were taken from the off-strut side of the plume. With certain exceptions external shock data tabulated in Ref. (37), when normalized by the scaling parameter $(T/q_\infty)^{1/2}$ all lay along in a restricted zone with a scatter of $\pm 30\%$. Exceptions lay $\sim 200\%$ above this curve. Reexamination of flow visualization photographs⁽⁴⁵⁾ showed that in these exceptional cases the shock shape tabulation of Ref. (37) was obtained from the strut side of the plume. (e.g. case No. 5, $P_c = 10$ psia, $\theta_c = 538^\circ\text{K}$, Figure III-47 of Ref. (37).)

Freestream Flow Uniformity

The freestream in tunnel M was found to be quite uniform. The flow vector lay within 0.3° of the tunnel axis at the plume outer shock periphery for case No. 7. In the ASC (10V) tunnel the model rocket was mounted 4 in. off the tunnel axis to make best use of the uniform core. This also has the advantage of insuring more nearly parallel freestream flow on the off-strut side of the plume (6 in. off the model rocket axis, 2 in. off the tunnel axis, on the off-strut side of the plane, and 11.7 in. downstream of the tunnel exit). In contrast, were the model rocket mounted on the tunnel flow axis, the freestream at the same location for case No. 7 would diverge $\sim 1^\circ$ from the tunnel axis. Axial and radial pitot probe surveys determined the spatial extent of the uniform freestream region, and disturbed regions were avoided in the plume studies.

Other Effects

Boundary layer growth in the model nozzle and influences on the plume outer shock and viscous region by the model body are discussed later with respect to simulation of full scale rocket plumes.

2.3 ELECTRON BEAM CONCENTRATION MEASUREMENTS

The electron beam technique provides the most important body of HAPRAP flow field data because each species concentration is unambiguously determined and the measurement system responds linearly in the range of species concentrations studied. This is not the case for the pitot probe data in the same flow field. However, several potential problems associated with the electron beam technique require examination. This section examines the electron beam data and its application for deducing valid estimates of plume properties.

2.3.1 Flow Field Concentration Measurements by Electron Beams

Multikilovolt electron beams can excite molecules and atoms which subsequently result in radiative emissions. The emission may be used as a diagnostic to determine the number density of the radiating states as well as the ground states which interact with the electron beam. The technique of using electron beam fluorescence requires knowledge of the processes affecting the population of the radiating state. These processes include primary and secondary (resulting from previous electron-ionization processes) electron excitation, collisional nonradiative deactivation, radiative lifetimes and radiation trapping of strong resonance lines.

The emission per unit volume from radiating states is given by the relation

$$I = (j\sigma_{\text{exc}}[x]) \left(\frac{1}{k_d[Y] + 1/\tau_{\text{rad}}} \right) \frac{1}{\tau_\lambda} \quad (41)$$

where

σ_{exc} = effective excitation cross section

$[x]$ = ground state number density

τ_λ = lifetime of observed radiation

τ_{rad} = lifetime for all radiative transitions from the excited state

k_d = collisional deactivation rate constant in collisions with species Y

$[Y]$ = number density of quenchant species, Y

The first parenthesis gives the emission without effects of collisional deactivation, resonance trapping and other radiative paths. The term $k_d[Y]$ is due to collisional quenching. The lifetime τ_{rad} of the excited state includes the effects of radiation trapping, if any.

Provided the excited states are not transported out of the radiometer field of view before they radiate, the emission given by Equation (41) offers the basis for remotely analyzing a gas flow. The following sections will examine the extent to which the complicating factors given by the second parenthesis in Equation (41) affect the HAPRAP data.

2.3.2 Validity of the Concentration Measurements

The HAPRAP simulated plume electron beam measurements are the first large data body on the hypersonic plume mixing layer region. The accuracy of these measurements must be determined. It will be necessary to show only that the concentration measurements behave linearly with species concentrations within the range of the plume data (even for the binary species mixing layer) and can be absolutely calibrated by independent means (e. g., not relying upon measurements or calculations of σ_{exc}).

Linearity and Accuracy of Concentration Measurements

The following linearity and accuracy tests of the electron beam measurement take advantage of independent knowledge of the experimental aerodynamics conditions:

1. The freestream species concentration upstream of the plume shock known from the wind tunnel conditions
2. The undisturbed jet centerline density found using method of characteristic (M.O.C.) computer calculations
3. The jet integrated number flux using electron beam measurements which remains constant with distance downstream from the jet exit plane.

Jet Species Concentrations

The electron beam survey along the jet centerline also provides a simple test of the jet species concentration measurements. Linearity can be checked because the jet centerline concentration varies as $1/x^2$ in the fully developed jet flow regime many exit diameters downstream where x is the distance from the jet exit plane. The centerline concentrations are undisturbed by the external flow (until the Mach disc regime is reached) and thus relatively easy to calculate. Jet centerline concentration profiles have been obtained from both an "exact" numerical techniques, the Lockheed M.O.C. program^(46,47,48) run by ARO, Inc. of AEDC, Tullahoma, Tenn., and a simple farfield flow model.⁽⁴⁹⁾ In Figure 12 the ASC(10V) facility jet centerline electron beam measurements⁽³⁷⁾ for case No. 7 with CO_2 are compared with both computation techniques.

The electron beam concentration measurements show the $1/x^2$ as illustrated by the farfield model's number density slope, the solid line labeled $[\text{CO}_2]$. The measured concentrations appear to fall about 10-30% below the magnitudes indicated by the Lockheed M.O.C. solution. This difference between the measured and static calibration jet concentration is in agreement with Figure 11 for the freestream gases.

A later version of the Lockheed M.O.C. program⁽⁵⁰⁻⁵³⁾ gives smoother profiles for two high area ratio, high specific heat ratio nozzles (Tunnel M case IB and ASC(10V) case No. 5⁽³⁷⁾) until the calculation terminates due to numerical difficulties associated with the very high Mach numbers (> 38.6) encountered in these flows. The calculations stopped before reaching the region in which the concentration data shows a $1/x^2$ dependence (i.e., in the fully developed exhaust flow where species self-quenching is negligible) and where comparison of the measurements and calculations is meaningful. The results of these latter calculations are not shown here. However, the comparison available in Figure 12 show that the ASC(10V) electron beam concentrations are:

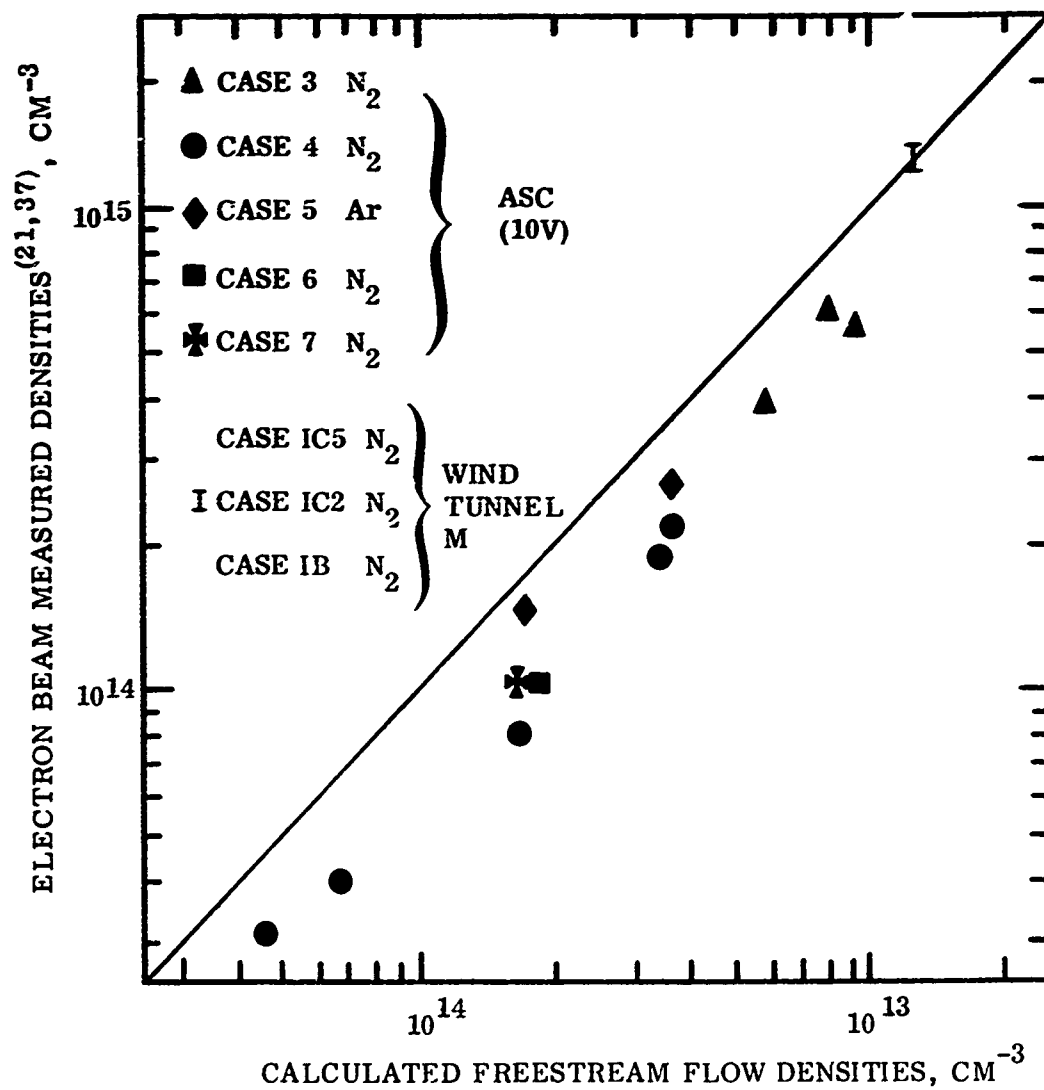


Figure 11. Comparision of calculated and measured electron bem densities

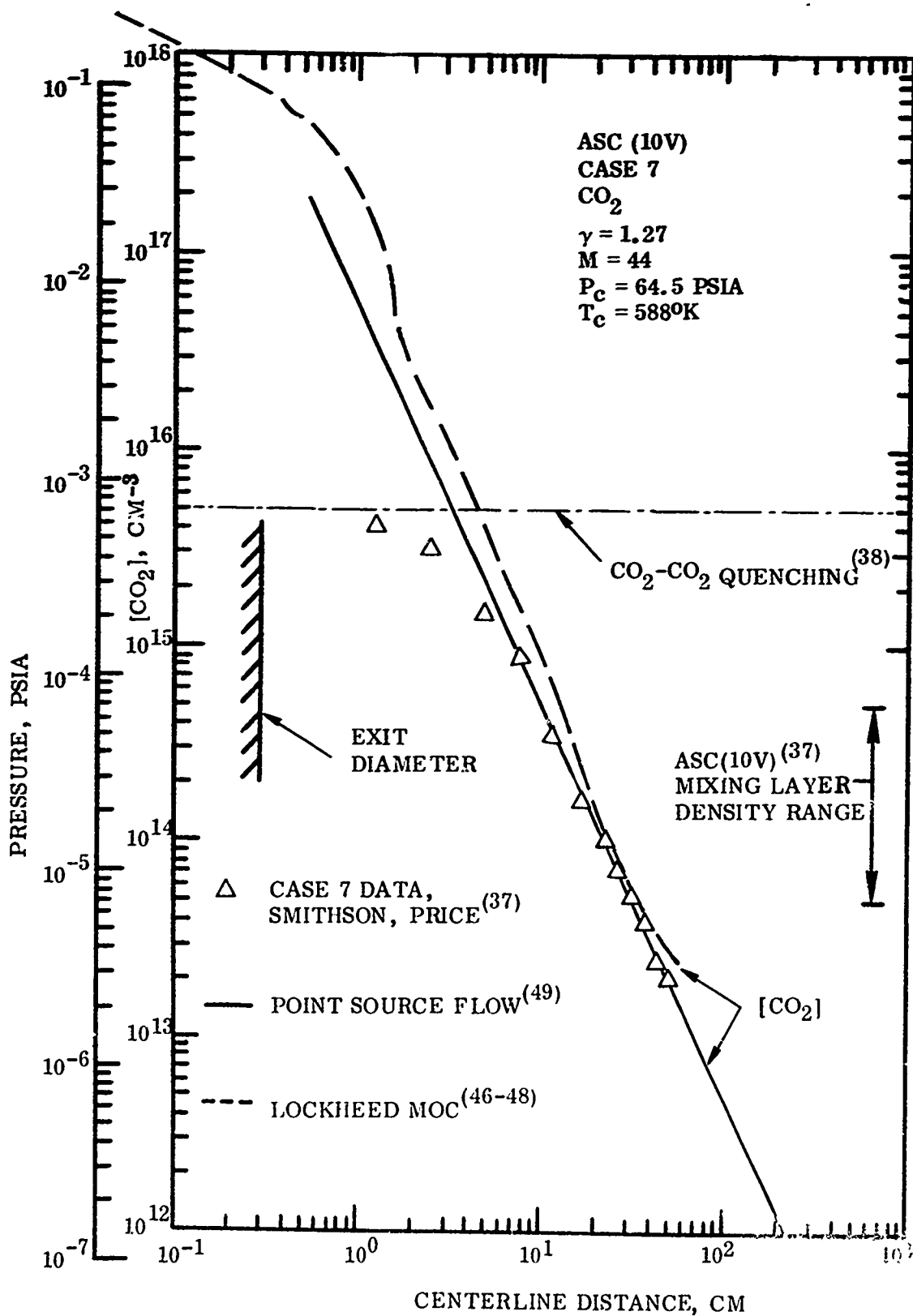


Figure 12. Electron beam density measurements compared to farfield jet calculations.

1. Correct for the principal jet species (CO_2) to within 10-30%,
2. Linear over the concentration range from 2×10^{13} - $9 \times 10^{14} \text{ cm}^{-3}$ (This covers the range of interest for mixing layer densities shown on the right-hand side of Figure 12.)

The electron beam concentration measurements are linear and their absolute calibrations are known for the tunnel M, D and ASC(10V) free-stream species, and for the ASC(10V) jet species, CO_2 . The centerline concentrations for the other ASC(10V) jet species, Ar, were not obtained from the M.O.C. calculations. The same is true of the helium jets which were used in tunnels M and D for the electron beam concentration measurements.⁽²¹⁾ These jet species calibrations are discussed in the following section.

Jet Particle Fluxes

The steady state flux of jet species remains constant from one axial station to another. Therefore, since the measured jet total number flux can be calculated, the number flux as measured by the electron beam along the jet axis provides another check on the electron beam measurement technique.

If, at a fixed axial station, x , the electron beam measurement at a radial position, y , of jet species j concentration is $n_j(y)$ and the gas speed is $u(y)$, then the jet total number flux N_j is

$$N_j = \int_0^{\infty} u(y) n_j(y) 2\pi y dy \quad (42)$$

The local gas speed, $u(y)$, was not measured, however, a useful approximation is

$$u(y) = u_{\text{lim}} \quad (43)$$

for the highly underexpanded jet exhaust. This approximation does not allow for the effects of compression in the inner shock (which tends to reduce $u(y)$ a small fraction) and shear in the viscous mixing layer regions (which may increase or decrease $u(y)$ depending upon the magnitude of u_∞). The major error in the determination of \dot{N}_j is in using u_{lim} for the mixing layer speed because of low values of $u_\infty/u(y)$. The resulting value of \dot{N}_j would be large by about 20% at the largest. Since the observed \dot{N}_j values are low compared to the values predicted it appears that the use of Equation (43) introduces only a small error.

Jet species fluxes have been calculated for some sample HAPRAP runs by carrying out the integration of the measured density profiles of Ref. (21 and 37) using Equation (42). Because quenching of He is a significant effect in the tunnel M runs the "corrected" electron beam concentration profiles of Ref. (21) have been used. The species fluxes are presented in Figure 13. The jet species flux are plotted against axial station. The horizontal lines show the calculated jet number fluxes assuming the perfect gas relation⁽⁵⁴⁾

$$\dot{N}_j = \gamma_j \left(\frac{A^* p_c}{a_c m_c} \right) \left(\frac{2}{\gamma_j + 1} \right)^{([\gamma_j + 1] / [2(\gamma_j - 1)])} \quad (44)$$

The measured He fluxes in the tunnel M cases are twice the calculated fluxes. The ASC(10V) measured particle fluxes are low by 20-40%. An error of this magnitude in the tunnel M and D measurements which were the first to be set up was possible.⁽⁵⁵⁾ In the ASC(10V) cases the freestream velocity is about equal to the jet limiting speed, while the reduction in the velocity across the oblique, hypersonic inner shock is small. Hence the density change due to departures of u from u_{lim} would also be small. The measured jet total number fluxes fall at ~30 to 80% of the calculated fluxes and vary linearly with the jet concentration. This is in substantial agreement with the previous examination of the ASC(10V) electron beam freestream species measurements.

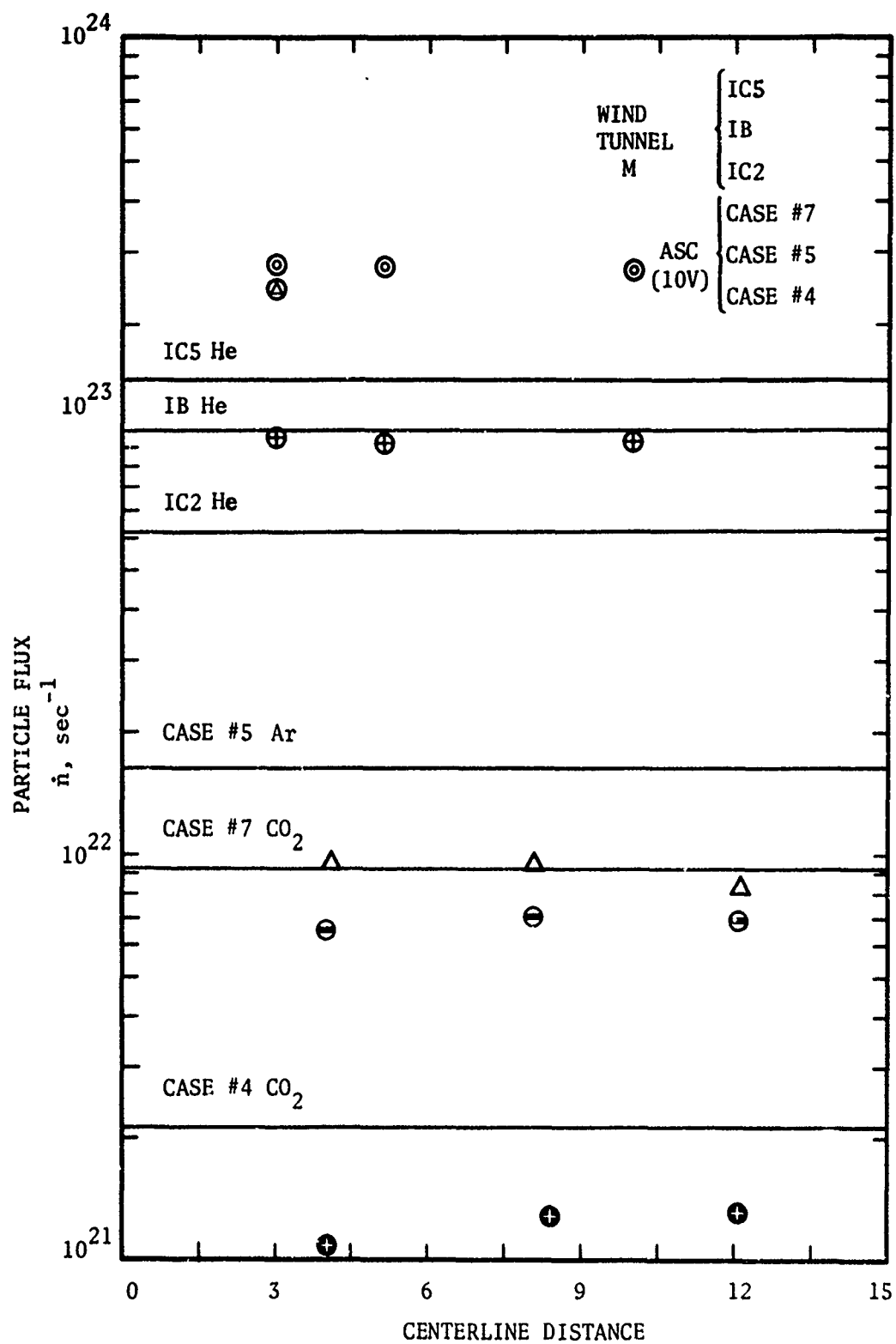
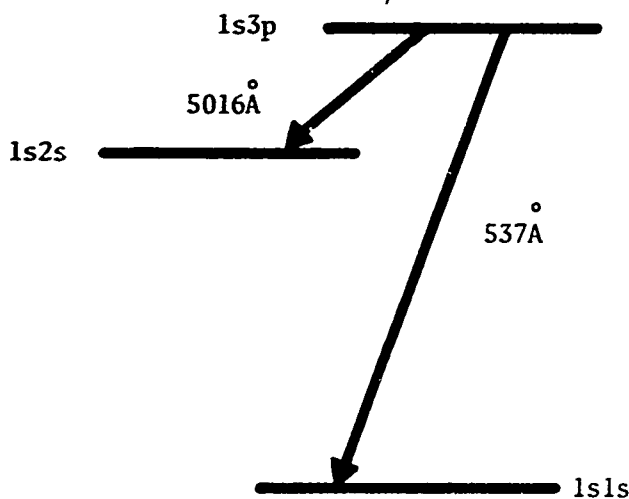


Figure 13. Jet particle fluxes measured by electron beam.

Resonant Trapping Effects in Helium

Radiation can be trapped in the gas when the gas is optically thick to the radiation. A particular example of this is resonant trapping in helium. This can occur only when the upper level of the diagnostic wavelength is common with a strong transition to the species ground state. This occurs for helium 5016A radiation which was observed in the tunnel M and D. The helium energy level diagram is shown schematically in Figure 14. The



(1s3p) state can radiate at 5016A and 537A producing transitions to the (1s2s) and (1s1s) states respectively. The 537A radiation is strongly absorbed and there can be many absorptions and remissions before the radiation escapes the gas.

The effect of resonant trapping is to increase the effective lifetime of the radiating (1s3p) level, longer than the 2×10^{-9} second spontaneous radiation lifetime.⁽⁵⁶⁾

If we denote this radiating level as He^* and the effective lifetime as τ_{eff} , then the net rate of production of He^* by electron impact is

Figure 14. Helium energy level diagram

$$\frac{d[\text{He}^*]}{dt} = j\sigma_{\text{exc}} [\text{He}] \sigma \frac{[\text{He}^*]}{\tau_{\text{eff}}} - k_q [\text{He}] [\text{He}^*] \quad (45)$$

where

$[He]$ = ground state helium number density;

$[He] \gg [He^*]$

k_q = collisional quenching rate constant

For the HAFRAP measurements these processes quickly (on the scale of the flow time and measurement system response) attain a steady state such that the emission observed from the 5016A line is

$$I_{5016} = \frac{[He^*]}{\tau_{5016}} = \frac{j \sigma_{exc} [He]}{\tau_{5016} / \tau_{eff} + k_q [He] \tau_{5016}} \quad (46)$$

where $\tau_{5016} = 7.5 \times 10^{-8}$ seconds is the 5016A radiative lifetime.⁽⁵⁶⁾ It remains to determine the effective lifetime for the helium (1s3p) level, τ_{eff} . Detailed measurements of τ_{eff} for 5016A emission were obtained by Heron, McWhirter and Rhoderick.⁽⁵⁷⁾ Their results are in agreement with the theoretical treatment of resonance trapping by Holstein.⁽⁵⁸⁾ The effective lifetime for the 1s3p state can be written

$$\frac{1}{\tau_{eff}} = \frac{1}{\tau_{5016}} + \frac{g}{\tau_{537}} = \left(\frac{1}{7.5 \times 10^{-8}} + \frac{g}{1.77 \times 10^{-9}} \right) \text{sec}^{-1}$$

$$\tau_{eff} = \frac{7.5 \times 10^{-8}}{1 + 42.3g} \text{ sec} \quad (47)$$

g must have values between 0 and 1. The quantity g is the escape factor to account for the resonance trapping. g is essentially the ratio of the number of 537A photons escaping the optically dense region to the total number emitted within the region. In the limit of infinite trapping, $g \rightarrow 0$, $\tau \rightarrow \tau_{5016}$ and I_{5016} is a maximum. In the limit of zero trapping, $g = 1$, $\tau \ll \tau_{5016}$ and I_{5016} is a minimum.

The escape factor for a cylindrical geometry and for a doppler broadened line is given by⁽⁵⁸⁾

$$g = \frac{1.6}{k_0} R \sqrt{\pi \ell n(k_0 R)} \quad (48)$$

$$k_0 = \frac{(\ell^*/\ell) \lambda^3 [\text{He}]}{8\pi^{3/2} \sqrt{2kt/m} \tau_{537}} \quad (49)$$

where

k_0 = maximum absorption coefficient⁽⁵⁹⁾ (only Doppler broadening)

ℓ = degeneracy of excited level $\ell s3p$

ℓ^* = degeneracy of ground level $(1s)^2$

k = Boltzmann constant

m = mass of helium atom

$\tau_{537} = 1.8 \times 10^{-9} \text{ sec}^{(56)}$

The effective radius R is given by the distance for the flow to change in direction which corresponds to a shifting of the velocity vector in the very cold, radially expanding jet flow. For conical flow, R is approximately x/M , where x is the axial distance and M is the Mach number at x . For case IC5 from tunnel M the helium jet ($\lambda = 537\text{\AA}$) with a concentration of $\sim 3 \times 10^{14} \text{ cm}^{-3}$ and translational temperature of $\sim 2^\circ\text{K}$ at a downstream centerline distance, x , of 25 cm (assuming no translational freezing). Under these conditions $k_0 \sim 190 \text{ cm}^{-1}$. Here the effective radius, R , is $\sim 1 \text{ cm}$; $g = 2 \times 10^{-3}$ and the 537A line is strongly trapped. At smaller x the trapping is more extreme as the helium density has a x^{-2} dependence, whereas the effective plume width discussed here varies more as x^{-1} .

Detailed calculations of g must be made at each point in the flow field. However, an approximate formula for the effective lifetime in the jet is

$$\tau = \tau_{5016A} (1 + g \cdot 42.3)^{-1} = 7.5 \times 10^{-8} \left(\frac{1}{1 + 3 \times 10^{13} / [\text{He}]} \right) \text{ sec} \quad (50)$$

Resonance trapping becomes important and Equation (12) is only applicable below 3×10^{13} helium atoms per cm^3 and can be ignored at higher densities.

Excited State Quenching

Collisional deactivation of radiating states which have been excited by electron impact must be considered in the measurement of species concentrations. Quenching becomes important when the mean time between collisions is comparable to or smaller than the radiative lifetime. That is

$$\left. \begin{array}{ll} \frac{\tau_{\text{rad}}}{\tau_{\text{col}}} \gg 1 & \text{quenching important} \\ \frac{\tau_{\text{rad}}}{\tau_{\text{col}}} \ll 1 & \text{quenching negligible} \end{array} \right\} \quad (51)$$

The collisional quenching time τ_{col} is given by the relation

$$\tau_{\text{col}} = \frac{1}{k_b} [\text{M}] \quad (52)$$

where k_b is the bimolecular hard sphere rate constant.

The temperatures in the plume mixing layer regions are on the order of 300°K (by N_2 rotational temperature measurement in tunnel M) and typically $k_b \sim 2 \times 10^{-10} \text{ cm}^3/\text{sec}$. For the tunnel M helium jets the mixing layer helium number densities reach $(3 \text{ to } 4) \times 10^{15} \text{ cm}^{-3}$. The minimum mean time between $[\text{He}] - [\text{He}]$ collisions is,

$$\tau_{\text{col}} \sim 1.6 \times 10^{-7} \text{ sec} \quad (53)$$

For the ASC(10V) typical plume mixing layer densities are $\sim (1 \text{ to } 2) \times 10^{14} \text{ cm}^{-3}$ such that

$$\tau_{\text{col}} \sim 2 \times 10^{-5} \text{ sec} \quad (54)$$

The ratio of radiative to collision lifetimes for the observed transitions are presented in Table I.

TABLE I.
Importance of Quenching in HAPRAP Mixing Layers

Species	Transition	$\tau_{\text{rad}}/\tau_{\text{col}}$	Reference	Quenching Corrections
N ₂	(1-)	3×10^{-3}	60	not required
CO ₂	FDB	5×10^{-2}	(Figure 12)	not required
Ar	$4'_p \text{ } ^2\text{F}^o \rightarrow 4_s \text{ } ^{12}\text{D}$	5×10^{-4}	56	not required
He	$3'\text{P}_1 \rightarrow 2'\text{S}_0$	$\sim 5 \times 10^{-4}$	56	required and carried out in Ref. (21)

Quenching is generally unimportant in the electron beam analysis of the ASC(10V) data but should be accounted for (as has been done in Ref (21), in the tunnel M data. It should be noted that quenching was observed in the high concentration regions of the ASC(10V) flow fields. The comparison of the CO₂ centerline calculations with the corresponding concentration measurements in Figure 12 show saturation of the CO₂ FDB system at $[\text{CO}_2] \sim 5 \times 10^{-15} \text{ cm}^{-3}$. The M.O.C. program calculations show the undeveloped part of the jet slowly rolling off from the exit number density of $\sim 1.6 \times 10^{17} \text{ cm}^{-3}$ and breaking

toward a $1/x^2$ slope at $x \sim 10$ cm or ~ 3 exit diameters. In contrast the electron beam centerline density measurements roll off toward a saturation level far downstream at $x \sim 100$ cm or 30 exit diameters, well in the fully developed ($1/x^2$) region of the jet. The extremes of the particle concentrations in the mixing layers studied in the ASC(10V) chamber cover a range well within the linear (i.e., $1/x^2$) CO_2 data range of $[\text{CO}_2] \sim 5 \times 10^{13} - 5 \times 10^{14} \text{ cm}^{-3}$ as indicated in Figure 12. Therefore both the Ar-Ar and CO_2 - CO_2 quenching have no important effect on the ASC(10V) electron beam density analysis of the mixing layer.

Beam Resolution

Blow-up of the electron beam could effect the interpretations of the measurements; however, in this experiment beam blow up does not degrade the data analysis. Electron beam blow up is caused by: 1) poor focusing, and 2) multiple scattering in the gas. An electron beam traversing a gas makes many elastic coulomb collisions with the nuclei in the gas and the beam tends to blow up into a gaussian shape. The full half-width of the gaussian shape W is given by the relation⁽⁶¹⁾

$$W = \frac{1.2 \times 10^{-27} n_j^{1.5} \ell_b^{2.5}}{1 + 3.5 \times 10^{-18} n_j \ell_b} \quad (\text{cm}) \quad (55)$$

n_j is the nitrogen number density per cm^3 and ℓ_b is the distance from the gun to the observation point. The coefficients are for nitrogen gas. This formula is for constant gas density along the path. In this experiment, the plume gases have variable density. Since the blow up is produced mainly by the gas near the beam entrance into the gas, and the plume is near the end of the path at the measurements, this formula should be applicable to this experiment. The beam widths at the plume axis for tunnel M and ASC experimental conditions are presented in Table II. In tunnel M, density measurements employed a one-inch long slit perpendicular to the beam.

TABLE II.
Electron Beam Widths in the Tunnel M and ASC(10V) Facilities

Tunnel	Gas	n_j	l_b	W
M	N ₂	$1.3 \times 10^{15}/\text{cm}^3$	50 cm	0.8 cm
ASC	N ₂	$\left\{ \begin{array}{l} 3 \times 10^{13}/\text{cm}^3 \\ 6 \times 10^{14}/\text{cm}^3 \end{array} \right\}$	70 cm	$\begin{array}{l} 0.008 \text{ cm} \\ 0.5 \text{ cm} \end{array}$

Since this was 2.5 times larger than the beam blow-up, multiple scattering beam blow-up is not important. In the ACS tunnel, the beam was swept perpendicular to viewing direction and there are no beam blow-up corrections, since the out-scattering correction at any point is compensated by the in-scattering from the opposite point. Thus the beam resolution is sufficient to obtain the measurements and the correction to the beam blow up can be neglected.

2.3.3 Flow Visualization Image Slip

In selecting radiative transitions for observation, care must be taken that the radiative lifetime is not so long that particles excited at one point in the flow are subsequently convected distances comparable to the flow structures dimensions before radiating. The systems selected for photometric concentration measurements made by electron beam in the HAPRAP work are all brief-lived (~ 10 -100 nsec) so that the convection displacement is negligible $\sim 10^{-2}$ - 10^{-1} mm for tunnel M ($u_\infty \approx 2.5$ mm/ μ sec) and less for the ASC(10V) data. Such is not the case for the flow visualization photography. The tunnel M flow visualization photographs⁽²¹⁾ reveal the plume outer shock in red. This radiation is from the N₂(1+)(4,0) system which has a radiative lifetime of $\tau = 6.7 \pm 0.7 \mu\text{sec}$.⁽⁶⁰⁾ The photographic image of the outer shock can be displaced a distance of approximately $\tau u_\infty \sim 1.7$ cm. This is illustrated schematically in Figure 15. The N₂⁺(1-)(00) system, used for the photometric concentration measurements, has an ~ 60 nsec⁽⁶⁰⁾ lifetime and is not subject to similar effects.

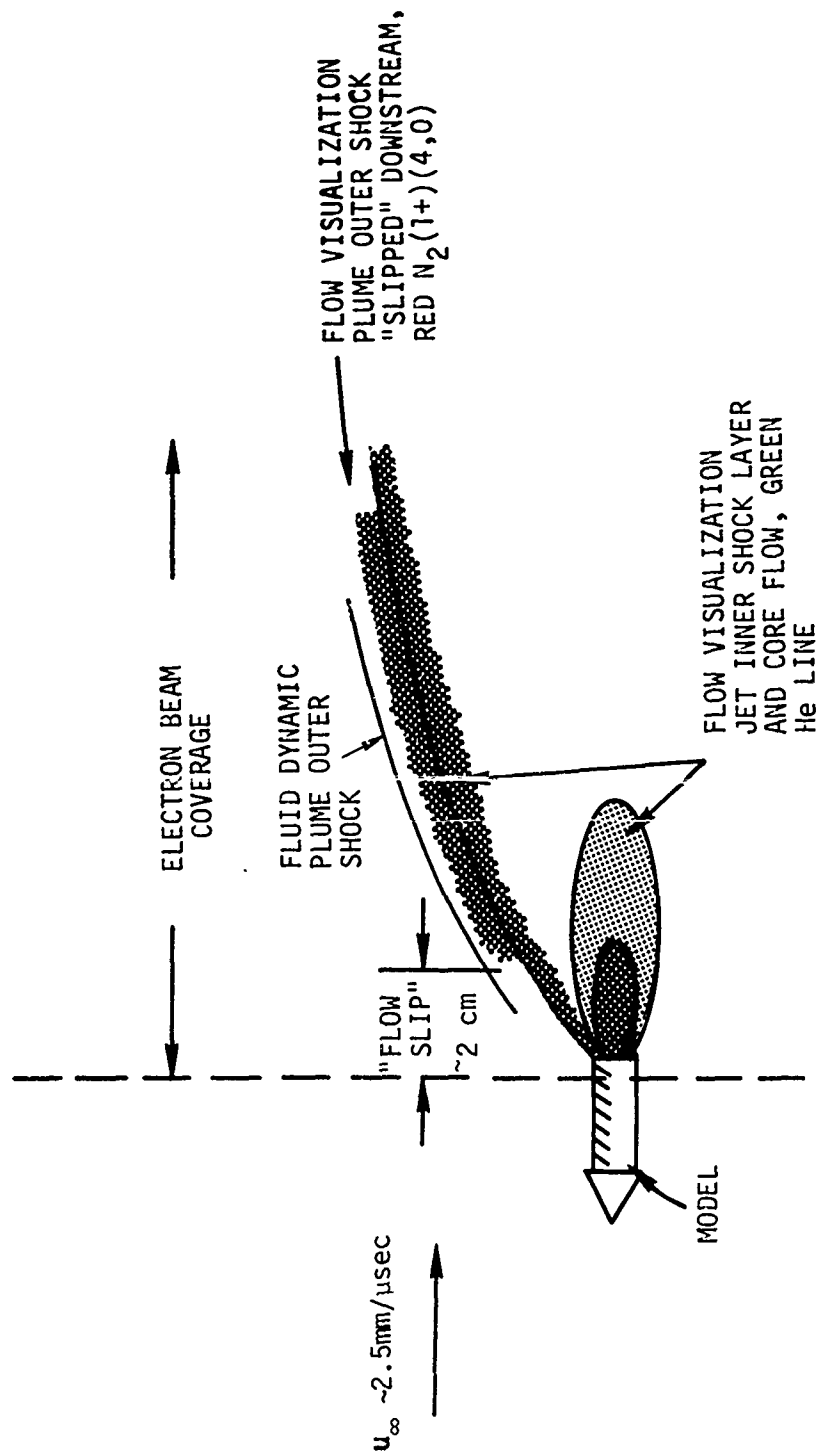


Figure 15. Sketch of N_2 shock "flow slip"

The long lifetime of the $N_2(1+)$ system results in an "image slip." Consider a short electron beam pulse at the point x_0 and at a time t_0 . The intensity variation with time $I(t)$ is

$$I(t) = I_0 e^{-(t-t_0)/\tau_{\text{rad}}} \quad (56)$$

where τ_{rad} is the excited state lifetime. Consider a gas moving at speed u_∞ downstream from x_0 and assume that the electron beam illuminates the region downstream from x_0 . The intensity per unit length at point x , $I_L(x)$, is determined by the sum of the decaying excitation from the illuminated points upstream of x .

$$I_L(x) = I_0 e^{-x/\tau_\infty} \int_0^x e^{x_0/\tau_\infty} \frac{dx_0}{\tau_\infty} = I_0 \left[1 - e^{-x/\tau_\infty} \right] \quad (57)$$

This gives the intensity buildup along the streamline. At $x = u_\infty \tau$ the intensity reaches 63% of its asymptotic limit, I_0 . This intensity buildup delay is clearly seen in Figure 24 and 25 in Ref. (21) and is approximately the expected amount of displacement flow.

A comparison between the three methods of determining shock position used for the tunnel M case IC5: 1) pitot probe, 2) electron beam $N_2^+(1-)$ emission and 3) $N_2(1+)$ flow visualization photography from Ref. (21) is shown in Figure 16. Note the close agreement between the steepest slope and total shock breadth locations as measured by the electron beam $N_2^+(1-)$ and pitot probe; however, the $N_2(1+)$ flow visualization indicates the shock image "displaced" ~ 2 cm downstream. This magnitude of the downstream shift is in agreement with the calculation of the distance required for intensity buildup.

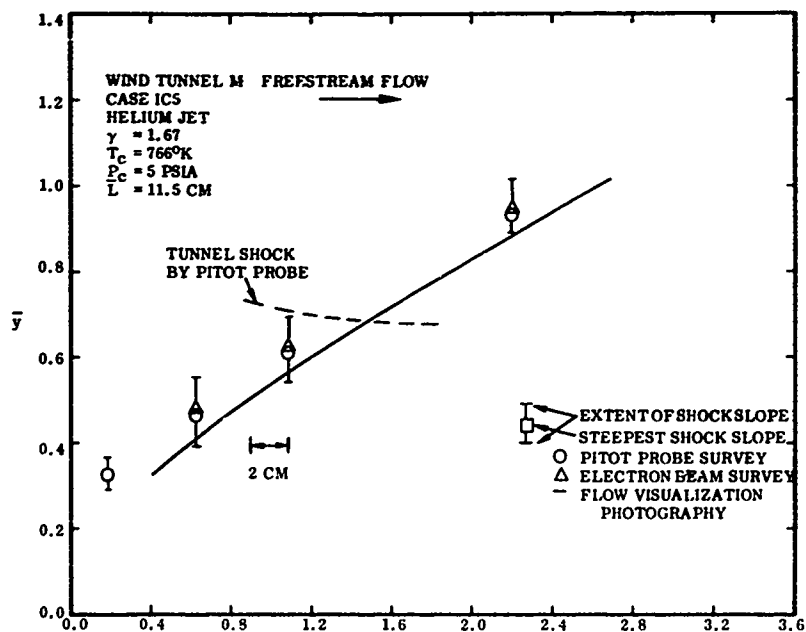


Figure 16. Plume Outer Shock Location by Three Techniques

Another problem arises with the flow visualization photographs using the $N_2(1+)$ red system. This system is excited almost entirely by the slow secondary electrons. The electron beam produces ion-electron pairs along its path. The slow secondary electrons move out from the beam and have the range

$$\text{Range} \approx \frac{3 \times 10^{13}}{[N_2]} \quad \text{meters} \quad (58)$$

where $[N_2]$ is the concentration. The free stream density in the ASC(10V) facility was 3×10^{13} to $6 \times 10^{14} \text{ cm}^{-3}$, corresponding to secondary electron ranges from 100 to 5 cm. The density jump across the outer shock reduces the range in proportion to the jump. Thus, the region of gas excited to radiate in the $N_2(1+)$ band is quite wide, further complicating the interpretation of the pictures.

2. 4 SUMMARY OF THE MEASUREMENTS VALIDATION

Most of the HAPRAP experimental data can be directly used to study the plume geometry and the viscous plume interaction. Specifically, jet gas condensation, jet species internal mode freezing, the support strut flow and freestream flow nonuniformity can be neglected or easily avoided in the data analysis. The electron beam concentration measurements behave linearly range and can be simply adjusted (by comparison with independent information) to give acceptable absolute values in the mixing layer structure for both jet and freestream species (N_2 , Ar, CO_2) in the ASC(10V) facility and only for freestream species in the tunnel M data. The helium jet data in the tunnel M has a factor of 2 calibration shift from the static data. In addition, radiation trapping effects are particularly hard to estimate in the mixing layer where the helium concentration rapidly goes to zero. Thus, there is some uncertainty in the analysis of the interaction region for the helium data.

The electron beam spatial resolution was quite satisfactory. Quenching is accounted for (as a 10-30% effect) in the tunnel M data and is negligible in the lower density ASC(10V) facility data.

The flow visualization photography indicates image shifts of the position of the N_2 shock structure because of reliance upon the long lived $N_2(1+)$ system. This effect is most important in tunnel M as its freestream speed is significantly higher than that for the ASC(10V) facility.

Pitot probe rarefaction corrections could be carried out. However, corrections for changing gas mixture ratios in the jet freestream interaction region cannot be made without considerable difficulty. Since the electron beam concentration measurements of the mixing layer structure can be calibrated to yield absolute jet and freestream species concentrations in a simpler and more dependable fashion, these latter measurements are used to study the mixing layer flowfield.

Section III

AERODYNAMIC SIMULATION OF FULL SCALE PLUMES

The freestream-jet interaction region behavior and the extent to which the HAPRAP studies simulate this region as it occurs in high altitude rocket plumes are of primary interest in the measurements program. The laboratory (wind tunnels M and D and Aerospace Chamber (10V)) data were intended to simulate conditions in a variety of full scale plumes at high altitudes. The purpose of this section is to show the degree of simulation attained and the extent of ICBM trajectories to which it applies.

3.1 THE SIMULATION PARAMETERS

Complete aerodynamic simulation of full scale missile plumes requires that all nondimensional parameters which characterize the flow be matched. The ranges of values for these parameters which occur in ICBM operation are first compared to the values of these parameters in the HAPRAP studies. Then the quality or completeness of simulation is discussed on the basis of this comparison.

One strongly radiating portion of the flow as observed in the field is the forward section of the plume where the dominant freestream influence at high altitudes is through its dynamic pressure. The HAPRAP tests were designed to examine this forward region of the plume by pitot probe and electron beam techniques. Simulation of ICBM flight at high altitudes (>100 km) requires large freestream Mach numbers ($\sim 6-10$) so that dynamic pressure is the dominant influence. The nozzle thermodynamic efficiency has been seen in Section 1 to affect the plume slenderness. The extent of the viscous mixing layer and the degree of shock rarefaction are controlled by the plume Knudsen number, see Section 1.

ICBM engines operate with sufficiently high nozzle densities that the freestream cannot penetrate this forward region of the exhaust flow and strong interactions occur which form the forward region of the plume flow. To assure sufficient interaction here and the proper nozzle boundary layer phenomenology the simulation of the exit plane Knudsen number (see Equation (33)), will also be examined. The plume can be perturbed by the missile body and the plume outer shock structure disturbance will depend on ℓ_m/\bar{L} where ℓ_m is the vehicle length. The mixing layer structure disturbance should depend on d_m/\bar{L} where d_m is the vehicle diameter. The relevant simulation parameters are therefore,

Freestream Mach number, M_∞

Engine thermodynamic efficiency, C_F/C_{Fmax}

Plume Knudsen number, $Kn_{\bar{L}}$

Engine exit plane Knudsen number, Kn_e

Ratio of body length to plume scale, ℓ_m/\bar{L}

Missile fineness ratio, d_m/ℓ_m

3.2 RANGE OF SIMULATION PARAMETERS

Freestream Mach Number, M_∞

The freestream Mach numbers to be simulated are those characteristic of full scale ICBM's at high altitudes. The velocity-altitude histories for three typical ICBM's² are shown in Figure 17. These histories are truncated at low altitudes where plume structure size approaches missile size, a region which is also associated with turbulent burning in the plume and not under study here. These histories terminate at high altitudes at main booster engine shutdown.

Mach number-altitude histories for these missiles are determined from Figure 17, and model atmosphere tabulations^(23, 62) of ambient gas properties ambient sound speed.

²As unclassified trajectory data were not available these vehicles are not further identified.

$$a_{\infty} = \left(\frac{\gamma_{\infty} k T_{\infty}}{m_{\infty}} \right) \quad (59)$$

These histories are shown in Figure 18 and show that Mach numbers of 6 to 10 are sufficient to simulate plumes to the highest altitudes of interest. A second reason that the ICBM Mach number range of 6 to 10 is desirable in the simulating facility relates to studies of plume rarefaction. It is easy and convenient to specify plume rarefaction development using the plume Knudsen number which is related to the degree of rarefaction by $M_{\infty}^{1/2}$, (see Equation (36)). Therefore, for the relatively restricted range of Mach numbers applicable to high altitude (>100 km) ICBM plumes we would like $M_{\infty}^{1/2}$ to be relatively constant and describe rarefaction solely in terms of Kn_L . Comparisons of the remaining simulation parameters with ICBM flight parameters are given as functions of M_{∞} .

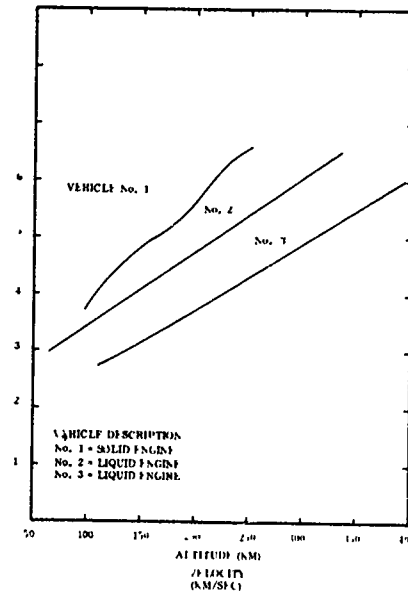


Figure 17. Typical missile Mach number altitude histories

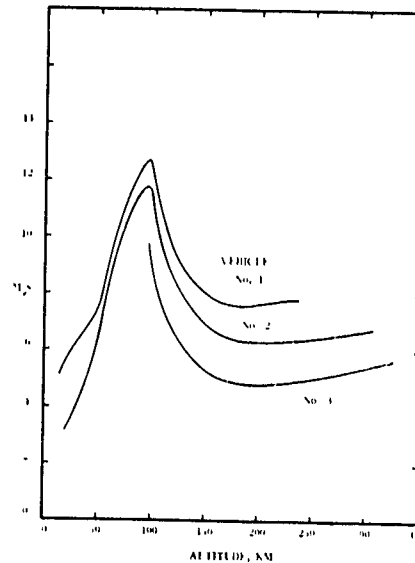


Figure 18. Typical missile velocity altitude histories.

Engine Thermodynamic Efficiency, $C_F/C_{F_{max}}$

The jet exhaust at large distances from the nozzle exit is characterized by total mass flow, an angular spread of this mass flow and the jet limiting velocity. The total momentum flow determines the overall plume scale. The angular spread of the mass flow determines the plume shape. Plume shape is related to nozzle efficiency through plume drag to thrust ratio, D/T . As outlined in Section 1, $C_F/C_{F_{max}}$ combines the engine design parameters γ_i and A_e/A^* , into a single parameter for the description of plume shape, for all plume scales.

Since the plume shape does not have a strong dependence on D/T , it is not necessary to precisely match D/T to obtain an acceptable simulation of the full scale plume. The range of D/T for the ICBM's shown in Figure 17 is seen in Figure 19. Jarvinen and Hill predict plume breadth varies as $(D/T)^{1/4}$.

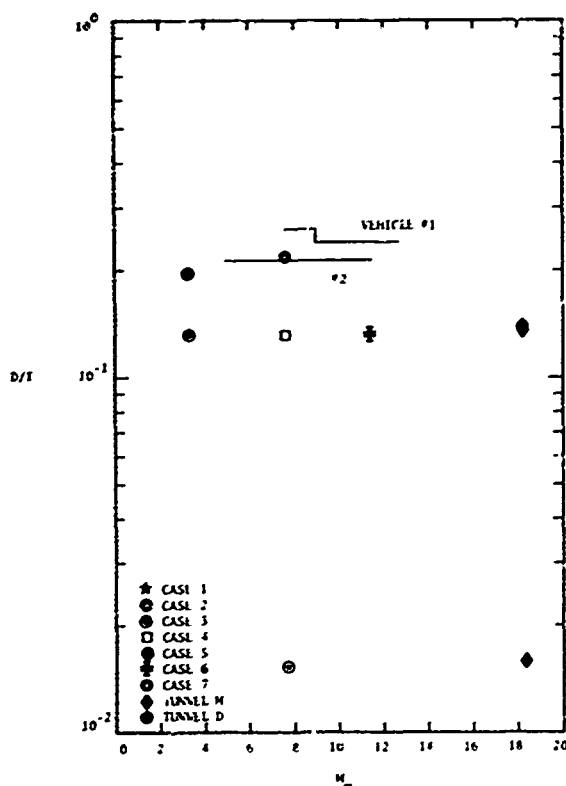


Figure 19. Full scale and HAPRAP plume shape parameters

This dependence is used to assess the degree of simulation of launch vehicles by HAPRAP tests as shown in Table III. Poor simulation for cases No. 5 and IIB resulted because very low values of D/T were selected to test the extreme influence of D/T.

TABLE III.
HAPRAP Simulation of ICBM Engines

Case	Facility	Simulation Error in $(D/T)^{1/4}$ (%)	Simulation in M_∞
1, 2, 3	ASC(10V)	< -20	M_∞ low
4, 6	↓	< -20	Satisfactory
5	↓	< -100	↓
7	↓	< 5	↓
Tunnels M, L*		< -20% (except for IIB)	↓
* The electron beam data from tunnel M were not incorporated into the rarefaction study so that the very large M_∞ values did not constitute a limitation.			

Plume Knudsen Number, Kn_L^-

Matching Reynolds numbers based on plume scale insures simulation of phenomena in the freestream-jet gas mixing layer provided that the freestream and jet gas physical properties are approximately matched, e.g., molecular weights and specific heat ratios. The Reynolds number based on the plume scale is

$$Re_L^- = Re_\infty \bar{L} = \frac{\rho_\infty u_\infty \bar{L}}{\mu_\infty} \quad (60)$$

and the plume scale is given by Equation (1). The viscosity can be approximated⁽⁶³⁾

$$\mu_{\infty} \cong \frac{1}{3} \rho_{\infty} \bar{c}_{\infty} \lambda_{\infty} \quad (61)$$

then

$$R_{e\bar{L}} \cong 2.225 \frac{M_{\infty}}{Kn_{\bar{L}}} \quad (62)$$

where the Knudsen number is given in Equation (33). A more exact relation for nitrogen ($\gamma_{\infty} = 1.4$) is,⁽⁴⁵⁾

$$R_{e\bar{L}} \cong 1.49 \frac{M_{\infty}}{Kn_{\bar{L}}} \quad (63)$$

Equation (63) shows that simulation of freestream Mach number and the plume Reynolds number assures simulation of plume Knudsen number. Notice that if we ignore variations in chamber pressure, vehicle speed and vehicle Mach number, plume Knudsen number varies as

$$Kn_{\bar{L}} \propto (\lambda_{\infty})^{1/2} \quad (64)$$

So that as λ_{∞} varies over a range of $\sim 10^4$ for a missile climbing from 100 km to 300 km, $Kn_{\bar{L}}$ and $R_{e\bar{L}}$ vary over a range of only $\sim 10^2$. In the HAPRAP tests conducted in the ASC(10V) both model rocket chamber pressure and freestream mean free path were varied, thus allowing a substantial part of this range in $Kn_{\bar{L}}$ to be covered. This does not mean that complete simulation was attained over this range as is shown below in connection with the other simulation parameters.

The ranges of R_{eL} associated with the vehicles and altitudes in Figure 18 and the values of R_{eL} and M_∞ for the HAPRAP tests are shown in Figure 20. The flight vehicle values of R_{eL} decrease monotonically by a factor of 100 with increasing altitude but Mach number does not vary greatly over the altitude range from 100 to 300 km. The high Reynolds number for the test in tunnel D⁽²¹⁾ does not satisfactorily simulate high altitude plumes (Figure 20). The low supersonic tests using the M3 nozzle in the ASC(10V)⁽³⁷⁾ (cases No. 1, 2, 3) do simulate flight vehicle values of R_{eL} but have values of M_∞ below the range of practical interest.

The HAPRAP tests which represent the best simulations of high altitude ICBM plumes, in terms of plume Reynolds number and stream Mach number are cases No. 4 through 7 in the ASC(10V) are shown in more detail in plots of plume Knudsen number versus M_∞ in Figure 21. These cases deserve further comment:

Case 4: This case is particularly interesting because it covers the greatest range of plume Knudsen numbers corresponding to an altitude range of 120 to 330 km for vehicle No. 2. This range was effected in two ways. First, model rocket and freestream reservoir pressures (P_c and P_o in the notation of Ref. (37) were varied over a range of a factor of ~ 60 (see Table IV, Ref. (37)). By Equation (1) the resulting Kn_L variation is a factor of 7-8, which is shown by the two lower points for case No. 4 in Figure 21. Second, while holding P_c/q_∞ constant the freestream reservoir temperature, T_o , was increased by a factor of ~ 3 . Increasing T_o increases u_∞ and λ_∞ which both tend to increase Kn_L (by a factor of 3 in this case). Hence the total variation in Kn_L was a factor of ~ 50 , corresponding to an altitude range of ~ 120 to 330 km.

Case 5: This case is not a good simulation of ICBM plumes because a high area ratio model rocket was used with Ar as the jet gas, which resulted in an unrealistically low D/T. This does not suggest that such engines have no function but rather that no existing booster rockets of practical interest are represented by this case.

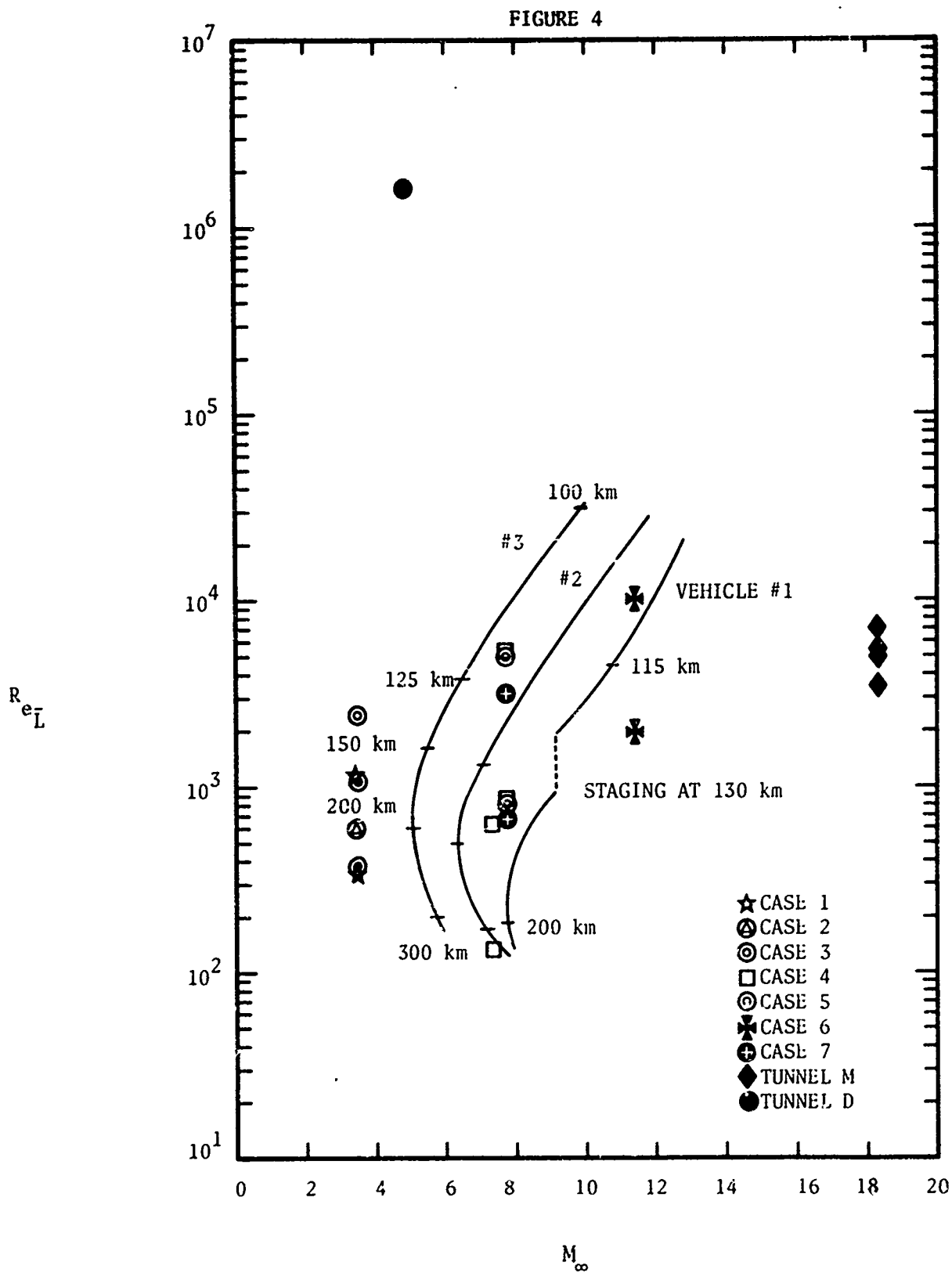


Figure 20. Full scale and HAPRAP Reynolds Number

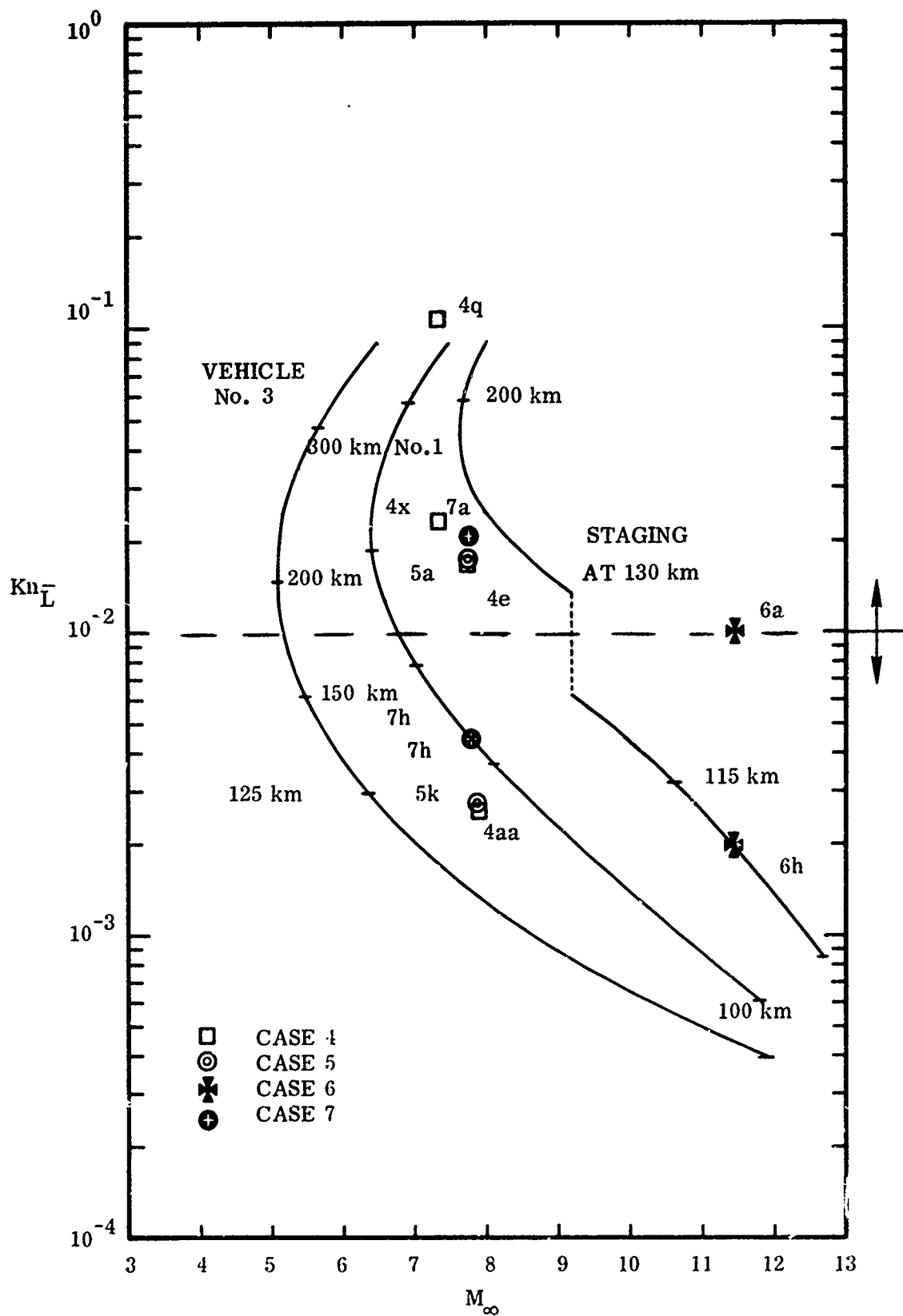


Figure 21. Scale and HAPRAP plume Knudsen numbers.

Case 6: This case simulates higher speed missiles over a restricted, low altitude range. This results from using Ar as the freestream gas with the M6 tunnel nozzle, so that $M_\infty \sim 11$. Simulation is questionable for this case because at low altitudes γ_∞ is close to 1.4 whereas in these tests $\gamma_\infty = 1.67$. This would probably cause poor simulation in plume outer shock location, however, contact surface location should be only weakly affected.

Case 7: This case differs from case No. 4, only in that it applies to a smaller range of altitudes.

The plume density regime designations shown on the left hand boundary of Figure 21 are discussed in Section 5 below.

Engine Exit Plane Knudsen Number, Kn_e

The situation to be simulated is that of a large and highly underexpanded ICBM engine operating at high altitudes. Accordingly in the model simulation the jet must have a very small Knudsen number (equivalent to large Reynolds number) at the nozzle exit plane,

$$Kn_e \equiv \frac{\text{exit plane mean free path}}{\text{nozzle exit diameter}} \equiv \frac{\lambda_e}{d_e} \quad (65)$$

to insure that the nozzle boundary layer is sufficiently thin to be neglected. The ranges of Kn_e values for the HAPRAP tests and for typical ICBM engines are shown in Figure 22.

Nozzle boundary layer development is usually expressed in terms of stagnation chamber Reynolds number. Kn_e is related to chamber Reynolds number, for frozen isentropic flow, by,

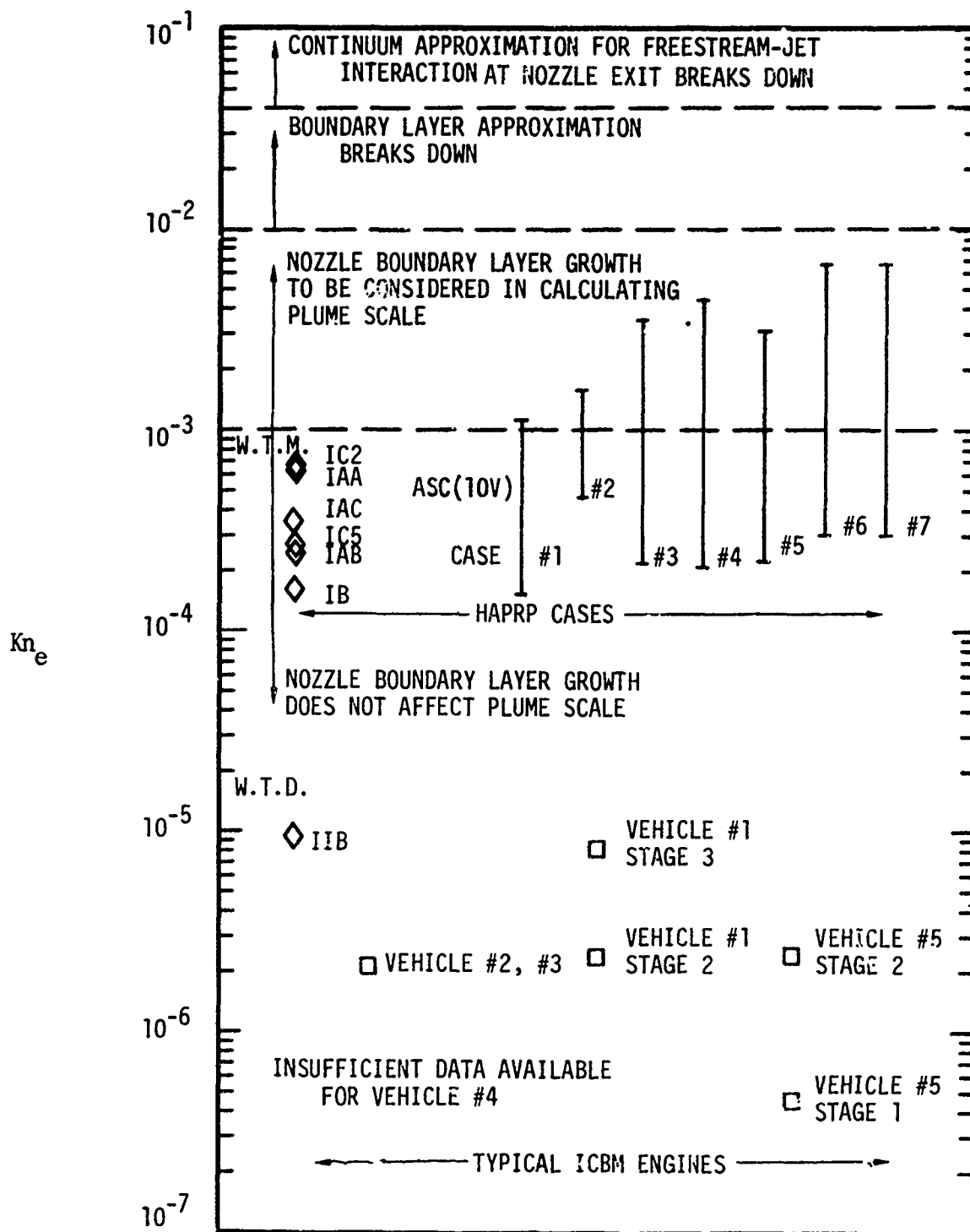


Figure 22. Knudsen number based on nozzle exit conditions for full scale vehicles and HAPRAP tests.

$$R_{e_{c,r}}^* = \frac{\rho_c (2H_c)^{1/2} r^*}{\mu_c} \quad (66)$$

This can be written as,

$$R_{e_{c,r}}^* \approx 1.5 \left(\frac{\pi \gamma_j}{\gamma_j - 1} \right)^{1/2} \left(\frac{A^*}{A_e} \right)^{1/2} \left(1 + \frac{\gamma_j - 1}{2} M_e^2 \right)^{1/(\gamma_j - 1)} Kn_e^{-1} \quad (67)$$

where H_c is the model rocket chambers enthalpy and Equation (61) has been used for the model rocket chamber viscosity. Equation (67) is written out to show that the conventional nozzle boundary layer thickness criterion based on $R_{e_{c,r}}^*$ may also be expressed in terms of Kn_e and that,

$$R_{e_{c,r}}^* \propto Kn_e^{-1} \quad (68)$$

HAPRAP nozzle exit Knudsen numbers, as seen in Figure 22, are large relative to those for typical ICBM's. Consequently a criterion is here developed to determine if model nozzle boundary layer effects, such as the reduction in the effective nozzle area ratio, may be neglected.

Calculations of nozzle boundary layer growth have been carried out⁽⁴⁵⁾ for case IC2 in tunnel M ($p_c = 2$ psia, $T_c = 700^\circ K$, $d^* = 0.315''$, $R_{e_{c,r}}^* = 2900$, jet gas helium). These show that the geometric area ratio of 1.61 is reduced to 1.30 by boundary layer growth. This corresponds to a reduction in thrust coefficient from $C_F = 1.42$ to $C_F = 1.38$. Because the plume scale varies as $C_F^{1/2}$ the observed plume should be $\sim 1-2\%$ smaller than that predicted on the basis of inviscid jet flow. A reduction of $\sim 1-2\%$ in jet scale would not be detectable due to experimental scatter.

For low γ_e and high A_e/A^* such as in cases IAB, IAC, IAA in tunnel M and cases No. 1 through 7 in the ASC(10V) reductions of the plume scales by boundary layers warrant further analysis. Boundary layer thickness is approximated as,

$$\delta \sim \left(\frac{20 S \lambda_n}{M_n} \right)^{1/2} \quad (69)$$

where

S = length of boundary layer development along nozzle wall

λ_n = mean free path at the outer edge of the boundary layer

M_n = Mach number at the outer edge of the boundary layer

This relation applies strictly to flat plates and may be expected to considerably overestimate boundary layer growth inside nozzles, as nozzles have strong favorable pressure gradients.

For a nozzle of $\sim 15^\circ$ half angle the exit diameter can be expressed as

$$d_e \sim \frac{S}{2} \quad (70)$$

If the dependence of δ on M_n is assumed to be similar for nozzles of interest then this dependence may be approximated by a constant typical value of $M_n (\sim 4)$, thus reducing Equations (69) and (70) to,

$$\frac{\delta}{d_e} \sim (10 \text{ Kn}_e)^{1/2} \quad (71)$$

Assuming that the boundary layer has a significant effect on the plume scale for $\delta/d_e > 0.1$, then those HAPRAP runs for which $Kn_e > 10^{-3}$ may be significantly perturbed by boundary layers development.

Figure 22 shows that tests in tunnel D best simulate ICBM engine boundary layers. However, as seen above, these tests provide poor simulations of plume Reynolds numbers. Of the remaining runs, some are affected to a marginal degree by boundary layer growth. Based on calculations^() for case IC2 it appears that the above boundary layer influence criterion is conservative and boundary layer influence is probably weak in all HAPRAP tests. It is apparent that if the HAPRAP nozzles had been significantly smaller or if the model rocket chamber pressures had been reduced further the data reduction task would have been severely complicated by boundary layer influences. From a judicious choice of operating condition and nozzle geometries these studies cover the broadest practical, useful range of Kn_e for studies of high altitude plumes.

Ratio of Body Length to Plume Scale, ℓ_m/\bar{L}

Rocket bodies influence jet plumes to a significant degree only if the rocket dimensions are comparable to plume dimensions. In such cases it is necessary to scale body geometry with plume scale in model simulation of booster rockets. Body influence is therefore judged in terms of the magnitude of the ratio of body length, ℓ_m , to plume scale, \bar{L} . The ranges of this parameter for typical flight vehicles and for the HAPRAP tests are shown in Figure 23. It was concluded in Section 1 that body influence on typical vehicles is not important for altitudes above 120 km. However, at substantially lower altitudes, corresponding to larger values of ℓ_m/\bar{L} , this influence becomes important. In all the HAPRAP model tests ℓ_m/\bar{L} was larger than for the typical flight vehicles at altitude of interest. In fact the model tests would have better simulated flight vehicle values of ℓ_m/\bar{L} over an altitude range of 85-100 km, a range where body influence on plume structure can be significant.

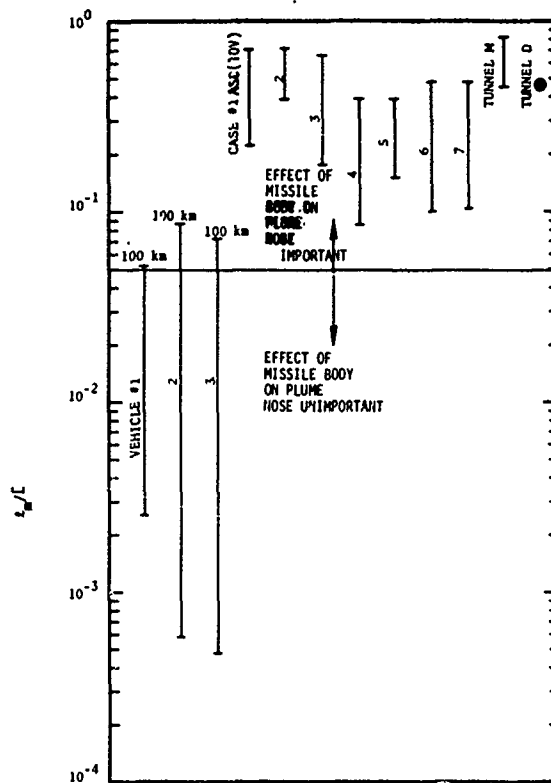


Figure 23. Ratio of vehicle body length to plume characteristic length.

We may expect that the rocket body size influence will be most strongly displayed in the plume outer shock location and shock layer structure as a result of the vehicle bow shock. If separated flow occurs near the base of the vehicle, entrainment of jet gas into the outer shock layer will occur. The location of the mixing layer, between jet and ambient gases, may be influenced to a lesser degree, since the primary external flow influence on its location and structure is through dynamic pressure. This pressure is not strongly altered by passage through the relatively weak bow shock associated with a slender vehicle. The following data analysis supports these arguments on the degree and nature of body influence on plume structure.

Missile Fineness Ratio, d_m/l_m

For the typical vehicles and altitude shown in Figure 23 the vehicle dimensions are small compared to plume dimension; therefore the vehicle influence on plume structure is not significant and details of body geometry such as fineness ratio (vehicle diameter \div vehicle length) are even less important. In an attempted simulation where model l_m/\bar{L} is not small there is little purpose in preserving the vehicle fineness ratio. Better simulation would be achieved if model geometry were designed to minimize body-plume interferences, which would result in bodies with fineness ratios of order 0.5-1.0 rather than of order 0.12-0.24 as in the HAPRAP tests.

3.3 SUMMARY OF THE AERODYNAMIC SIMULATION

The degree of simulation of flight vehicles is summarized in terms of the parameters discussed above. Overall degree of simulation is judged by weighting these parameters as shown in Table IV. The first three columns identify the HAPRAP tests by facility, reference and case designations. For the measurements reported in Ref. (37), case designations are taken from Table IV, pp. 59-61, which is labeled "Electron Beam Photograph Test Conditions" (note: this table is the most comprehensive but is not complete; e.g., case No. 2 tests with Ar as the jet gas are reported in Table V, p. 62 but not in Table IV). In Table IV of Ref. (37) runs are listed vertically under case numbers. We have identified different runs under each single case number by adding alphabetically a single letter (double letters for more than 26 runs) to the case number, e.g., 4a, 4b, . . . 4z, 4aa . . .

Table IV shows that the simulation of the flight vehicle mixing layer which is the principle phenomenon under investigation in the HAPRAP measurements, by matching values of Kn_L is excellent for all cases except the test conducted in tunnel D. This is shown in Figure 20 where Re_L (Kn_L) for tunnel D is much larger than the range for flight vehicles at altitude of interest, whereas all other test results lie within this range. The tunnel M case simulation of mixing layer structure are acceptable. Unfortunately the freestream Mach

TABLE IV.

SUMMARY OF HAPRAP SIMULATION OF ICBM FLIGHT

Simulation Parameter Facility	Ref.	Case	M_{∞}^*	D/T	$Kn \bar{L}$	$Kn \bar{L}$	$Kn \bar{L}$	$\ell m / \bar{L}$	γ_{∞}	Overall Simulation		Remarks
										Quantitative†	Qualitative	
Tunnel M†† → Tunnel D ASC (10V) →	21 → 37 →	IC5	5	4	5	4	3	4	4	0.30	Fair	$\ell m / \bar{L}$ large
		IAB	5	4	5	4	3	4	4	.30		
		IC2	5	4	5	4	3	4	4	.30		
		IAC	5	4	5	4	3	4	4	.30		
		IAA	5	4	5	4	3	4	4	.30		
		IB	5	1	5	4	3	4	4	.08	Poor	D/T small $Kn \bar{L}$ small M_{∞} small → γ_{∞} large
		IIB	4	4	1	5	3	4	4	.06		
		1a-1d	2	5	5	4	3	4	4	.15		
		2a-2c	2	5	5	1	3	4	4	.15		
		3a-3k	2	4	5	4	3	4	4	.12		
		4g	5	4	5	3	3	4	4	.06	Fair	
		4c	5	4	5	4	3	3	3	.23	Fair	
		4x	5	4	5	4	3	3	3	.23	Good	
		4bb	5	4	5	4	4	4	4	.41	Poor	D/T small γ_{∞} large γ_{∞} large
		5a-5k	5	1	5	4	3	4	4	.08		$\ell m / \bar{L}$ large
		6a	5	4	5	4	3	1	1	.08		$\ell m / \bar{L}$ large
		6h	5	4	5	4	4	1	1	.10		γ_{∞} large
		7a	5	4	5	4	3	3	3	.23	Fair	
		7h	5	4	5	4	4	4	4	.41	Good	$\ell m / \bar{L}$ large

* Simulation Weights: 5 = excellent 3 = fair 1 = very poor
4 = good 2 = poor

† Quantitative weight equals product of weights divided by (5⁶).

†† Here the very large values of M_{∞} and their effect upon rarefaction were not included in determining the M_{∞} weights for tunnel M as these data were not used in the rarefaction study.

numbers are so large that the critical plume Knudsen numbers for rarefaction in ICBM plumes are not well simulated. Table III.2 shows that cases No. 1 through 3 in the ASC(10V) do not adequately simulate vehicle freestream Mach numbers. They are too low to insure that stream dynamic pressure is the dominant stream influence on plume structure over a major portion of the plume nose region.

The remaining ASC(10V) data show various degrees of quite acceptable simulation. It is noted that cases No. 5 and IB were characterized by extremely small values of D/T , thus they did not satisfactorily simulate any existing booster vehicles. In cases No. 6a to 6h, $\gamma_{\infty} = 1.67$ which is a reasonable simulation of the freestream only in the upper portion of the altitude range of interest. However, it was noted earlier that γ_{∞} affects the plume outer shock layer but has only a weak effect on location of the mixing layer and on internal jet structure. Thus these cases may provide good simulations of these plume features.

The remaining measurements including all of cases No. 4 and 7 provide fair to good overall simulations of high altitude rocket plumes. Figure 23 and Table III.2 show that large model bodies are the main limitation to achievement of excellent overall simulation. Because of this the HAPRAP simulations of plume outershock structures are severely compromised. However, the mixing layer and internal jet flow field are relatively less disturbed by body influences and should therefore be reasonably well simulated in terms of flow field structure.

Section IV

PLUME MIXING LAYER FLOW FIELD ANALYSIS

There are four principal categories into which the flowfield analysis falls: the plume outer shocks; the plume inner shocks (barrel shock and Mach disc); the surfaces of equal concentrations of freestream and jet species; and the concentrations along these surfaces of equal concentration. Analysis of plume outer shocks revealed several disturbing influences which limit useful interpretation. Mach disc locations illustrate longitudinal scaling of the interior flow as a function of nozzle and stream conditions. Within mixing layers, surfaces of equal concentrations are shown to be relatively insensitive to the disturbances which influence outer shocks. They are studied in some detail as they may prove to be of some importance for developing a simple and quick calculation technique for estimating the rates of chemical and excitation processes in the high altitude rocket plume mixing layer.

4.1 THE PLUME OUTER SHOCK

HAPRAP measurements of plume outer and inner shock locations, obtained in both tunnel M and the ASC(10V), have been transformed to coordinates normalized by the hypersonic scale. Selected results are shown in Figure 24 where $D/T = 0.135$ and in Figure 25 where $D/T \approx 0.017$. In this section we discuss only the outer shocks. These outer shocks clearly are not correlated only by the hypersonic scale at fixed D/T . A variety of effects related to aerodynamic simulation and measurement techniques appear to be the source of this lack of correlation.

1. The limited extent of the strong outer shock region dominated by the freestream dynamic pressure
2. Varying values of the freestream specific heat ratio

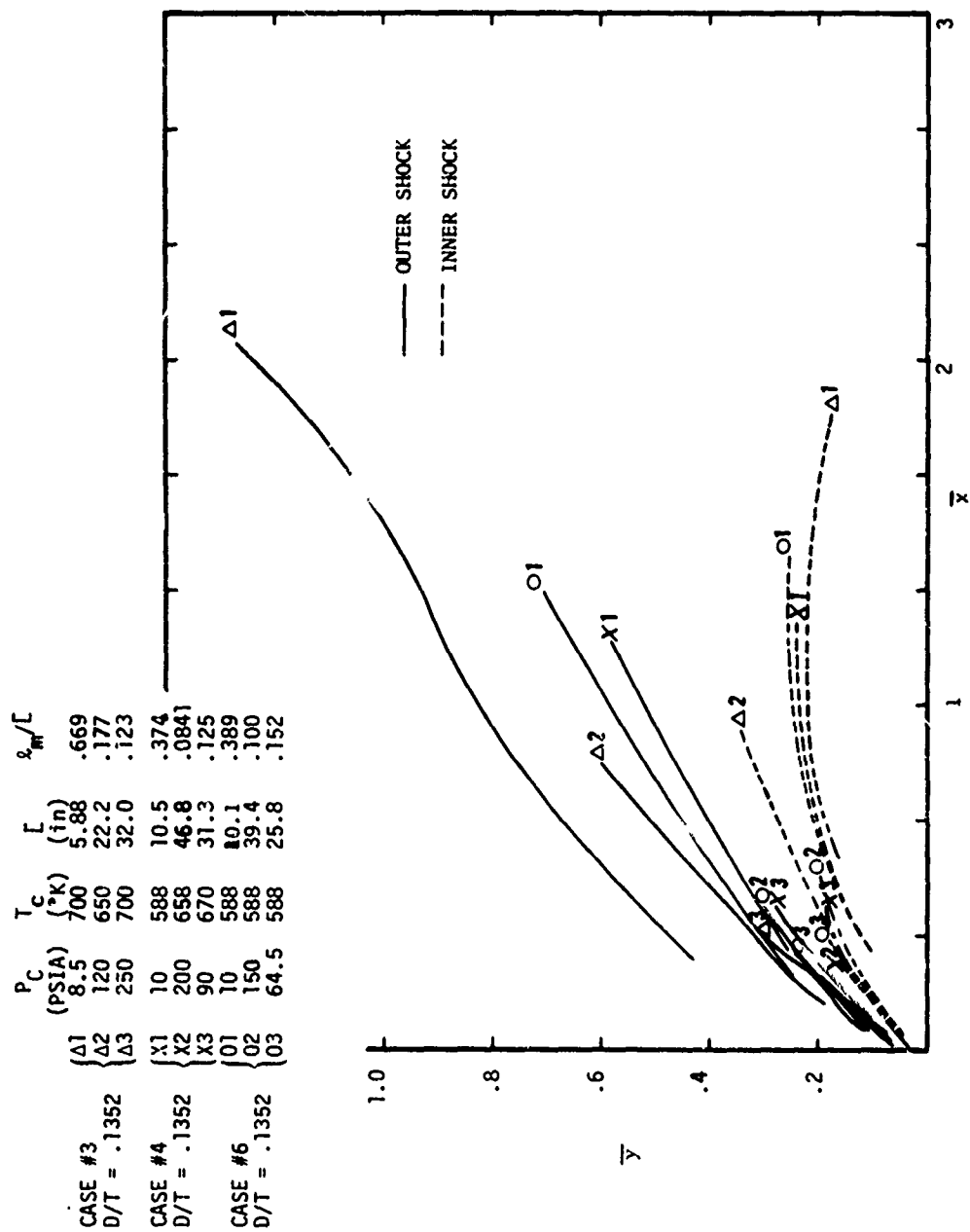


Figure 24 - Electron beam flow visualization photographs for ASC(10V) Cases No. 3, 4, 6.

3. Image slip in the flow visualization photographs
4. Freestream flow divergence
5. Errors in alignment of the electron beam apparatus
6. Growth of the viscous mixing layers

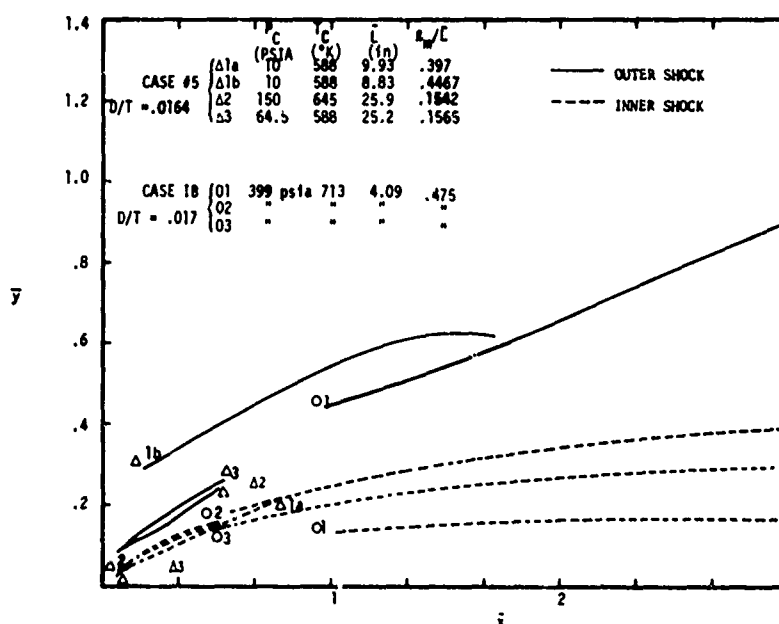


Figure 25 - Electron beam flow visualization photographs for ASC(10V) Case No. 5 and tunnel M Case IB.

The outer shock locations in cases No. 1 through 3 in the ASC(10V) should not collapse to a single curve at fixed D/T , since the freestream Mach number was too low and the assumption of strongly hypersonic external flow is not satisfied. This correlation does not include the dependence of γ_∞ , which is known to affect outer shock locations; consequently case No. 6 in the ASC(10V) with $\gamma_\infty = 5/3$ is not expected to display the same normalized outer shock position as the other tests where $\gamma_\infty = 7/5$. Flow visualization photographs for tunnel M are subject to image slip, discussed in Section 2, and consequently the photographed shock locations are somewhat downstream from their true locations.

Nonparallel freestream flow and flow not aligned with the model rocket axis for the flow visualization photographs for the ASC(10V) facility may have caused shifts in the shock locations from those locations for a freely coparallel plume. The freestream flowfield diverged significantly and the model was mounted off the tunnel axis, consequently the plume say an average effective angle of attack of $\sim 3^\circ$. The "flow axis" in flow visualization photographs for the ASC(10V) was determined by bisecting upper and lower portions of images of the shock locations, ⁽³⁷⁾ which results in a flow centerline diverging from the true jet axis. Recall that on the side of the plume away from the model strut the freestream flow was nearly parallel with the jet axis and thus constituted an acceptable simulation for the electron beam concentration measurements which were referred to the true jet axis.

For the early ASC(10V) cases ⁽³⁷⁾ the electron beam used to measure speicies concentrations was not well aligned with the flow axis which resulted in a distortion of the plume geometry in the region near the mosel rocket. This is evident in case No. 3 in Figure V-1 on page 305 showing the jet centerline concentration abruptly falling off as X/RE drops below ~ 10 . This corresponds to the electron beam slicing through the side of the plume (rather than remaining on the centerline) and is made evident when the radial surveys are used to plot the plume profile.

There were also perturbations due to the model rocket body when it was of significant size compared to the hypersonic plume scale. We see that the plume outer shock is markedly moved upstream in case $\Delta 1 (\ell/\bar{L} \sim 0.67)$ of Figure 24 and in $\Delta 1b (\ell/\bar{L} \sim 0.40)$ of Figure 25.

There is an important additional influence on the outer shock structures which is illustrated using pitot probe data from tunnel M, as shown in Figure 26. Here the outer shocks (outer maxima in pitot pressure) are plotted in normalized coordinates for tests with the same freestream gas, comparable ratios of body length to plume scale, and nearly equal nozzle efficiencies. Observed differences in the scaled outer shock locations must be attributed either to differences in nozzle exit Mach numbers or jet gas species or both.

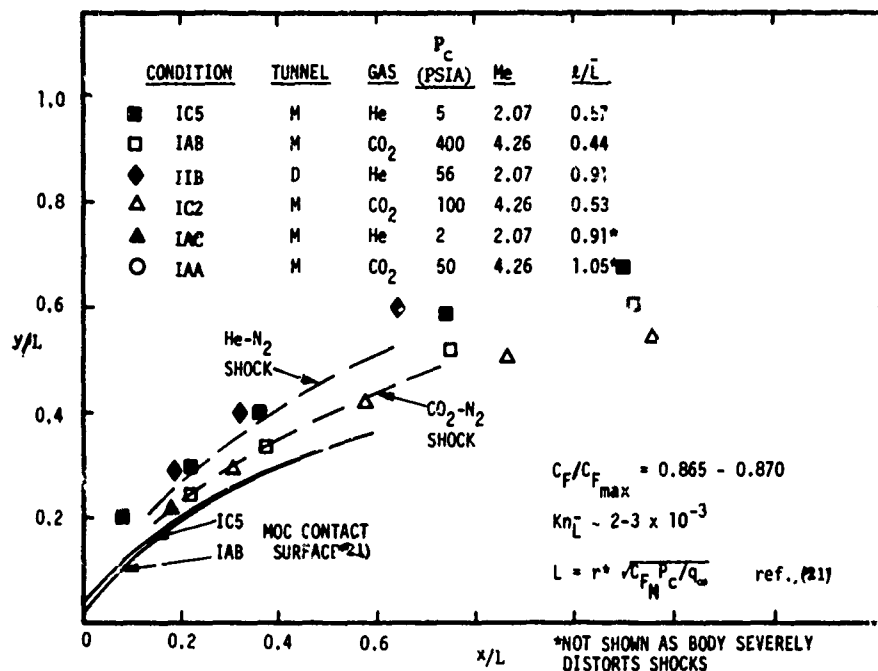


Figure 26 - Viscous layer influence on outer shock layer location.

For the data in Figure 26 plume Knudsen numbers are $\sim 2 - 3 \times 10^{-3}$ so that the plume flow fields are in the viscous continuum regime and it is appropriate to describe outer shock locations on the basis of viscous shock layers, i.e., viscous flow throughout the region between inner and outer shocks. To obtain a reference surface for description of outer shock locations we assume that the viscous shear layer is centered on the plume contact surface as obtained from inviscid calculations.

Method of characteristics solutions for contact surfaces corresponding to two of the tunnel M cases⁽²¹⁾ (IC5, IAB) are shown in Figure 26 normalized by the hypersonic plume scale. These show that varying M_e does not significantly alter the normalized contact surface location (at fixed D/T) and therefore does not significantly influence the outer shock location. This suggests that the difference in plume outer shock locations in Figure 26 are the result of different jet gases. Considering viscous effects, we may expect that the viscous layer

layer thickness is larger for He jets than for CO_2 jets because, everything being equal, He has a greater viscosity than CO_2 .

The shock layer thickness will be qualitatively described by viscous shear layer analysis. From Lock⁽⁶⁴⁾ the viscous shear layer thickness, at fixed concentration and temperature, is taken to vary as,

$$t \propto \nu^{1/2} \propto m^{-1/4} \sigma^{-1/2} \quad (72)$$

where

t = viscous shear layer thickness

ν = kinematic viscosity

m_j = molecular mass of species j

σ_j = molecular collision cross-section of species j

Here, $\nu \propto \bar{c} \lambda$ has been used where \bar{c} is mean thermal speed and λ is mean free path in the layer.

We assume the shear layer viscosity is characterized by the reduced mass, m_μ , of a gas mixture of equal parts of freestream and jet gas. For the two shear layers being compared the ratio of reduced masses is

$$\frac{(m_\mu)_{\text{CO}_2 - \text{N}_2}}{(m_\mu)_{\text{He} - \text{N}_2}} = \frac{1/m_{\text{He}} + 1/m_{\text{N}_2}}{1/m_{\text{CO}_2} + 1/m_{\text{N}_2}} \sim 4.9 \quad (73)$$

and the ratio of collision cross sections⁽⁶⁵⁾ is

$$\frac{\sigma_{\text{CO}_2 - \text{N}_2}}{\sigma_{\text{He} - \text{N}_2}} = \frac{(r_{\text{CO}_2} + r_{\text{N}_2})^2}{(r_{\text{He}} + r_{\text{N}_2})^2} \sim 1.7 \quad (74)$$

where r_j is the radius of species j derived from viscosity data. The resulting ratio of magnitudes of viscous layer thicknesses is

$$\frac{t_{\text{He} - \text{N}_2}}{t_{\text{CO}_2 - \text{N}_2}} \sim 4.9^{1/4} 1.7^{1/2} \sim 2 \quad (75)$$

The viscous outer shock layer thickness is estimated from Figure 26 as the normal distance between the corresponding inviscid contact surface (shown by the solid line) and the mean (shown by the dashed line) through the outer shock data points for a single jet gas. It is seen that the estimated He - N₂ outer shock layer thickness is indeed approximately twice that for CO₂ - N₂. The observed plumes are in a fully viscous regime and display outer plume shock shifts in location directly related to viscous layer growth. Viscous effects have a pronounced influence on plume structure even well within the continuum regime, $\text{Kn}_L \sim 10^{-3}$ which corresponds to ICBM flight at altitudes of ~ 100 km, see Figure 21. Therefore, purely inviscid plume flows do not occur at high altitudes where the simple hypersonic inviscid plume models are used. However, such models do remain quite useful for restricted purposes as will be seen below.

In evaluating the usefulness of the Jarvinen-Hill inviscid plume model, the present examination of the outer shock structures has shown that:

1. Comparison of data in coordinates normalized by the hypersonic plume scale with the same jet and stream gases for similar degrees of body influence and similar D/T, still shows a considerable scatter of ($\sim \pm 20\%$) which overlaps the Jarvinen-Hill shock position

2. The normalized shock surfaces are more slender for smaller D/T , which is in qualitative agreement with the Jarvinen-Hill model; however, there are limitations imposed on the usefulness of calculating shock locations in the high altitude plume imposed by the appearance of viscous and rarefaction phenomena.
3. Viscous effects can have a significant influence on the locations of high altitude plume outer shocks.
4. Moreover, by way of anticipation of the results of Section 5, shocks lose their identity as the plume enters the transitional flow regime.

In general we see that disturbing influences and low density effects make the interpretation of these outer shock data of limited value for the study of viscous, high altitude plumes structure.

4.2 THE MACH DISC

The Mach disc is an interior shock frequently used to establish the longitudinal scale for plume flowfields. The Jarvinen-Hill⁽¹⁹⁾ model places the Mach disc a distance of $3\bar{L}$ downstream of the engine independent of the value of D/T . However, it is shown in Section 1 that the longitudinal scaling of the interior flow must also depend on D/T . This is supported by the tunnel M Mach disc data presented in Figure 27, where the Mach disc location has been normalized by \bar{L} . A definite D/T dependence appears which agrees qualitatively with the discussion of Section 1. The normalized distance from nozzle to Mach disc increases from $\sim 2.85\bar{L}$, for $D/T \sim 0.14$, to $\sim 4.3\bar{L}$, for $D/T \sim 0.017$. The mach disc will be placed at $\sim 2.9\bar{L}$ for the ICBM type plume for which $D/T \sim 1/6$.

In the five cases with comparable D/T (0.138-0.142) in Figure 27, normalized mach disc locations lie fairly close to the Jarvinen-Hill prediction of $3\bar{L}$. In all these cases the static pressure contribution to the total mixing layer pressure (based on Newtonian flow and mixing layer slope obtained from

electron beam photographs) is less than 10% over the portion of the plumes forward of the Mach disc location. Consequently the hypersonic scale $(T/q_\infty)^{1/2}$ used by Jarvinen and Hill, is appropriate. For case IB in Figure 27, where $D/T \sim 0.017$, the static pressure contribution to the mixing layer pressure, by Newtonian theory is $\approx 60\%$ at the Mach disc location. However, as the static pressure contribution increases the local mixing layer pressure over the dynamic pressure term (based on the local mixing layer slope) its effect should be to reduce the Mach disc length scale. Consequently it is implausible that the Mach disc location differs from the Jarvinen-Hill model due to the static pressure effect and what we see in Figure 27 is a D/T dependence. Unfortunately there is only one measurement of the Mach disc location for $D/T \sim 0.017$ (the ASC(10V) case No. 5 axial pitot survey does not show a Mach disc structure). In any event, it appears that the Mach disc location is not properly scaled by $(T/q_\infty)^{1/2}$ alone.

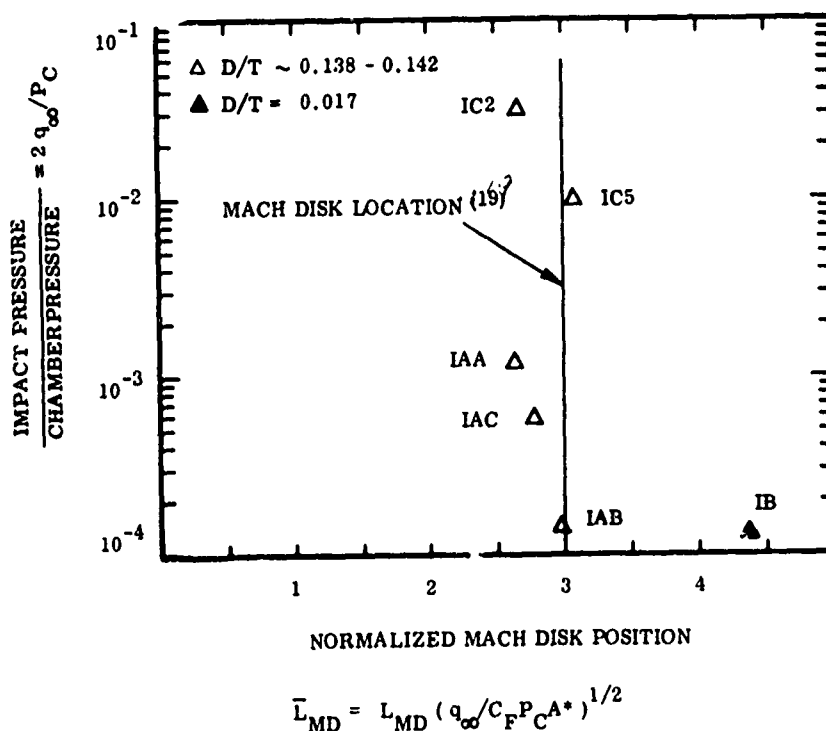


Figure 27 - Dependence of Mach disk location on plume drag-to-thrust ratio

For the tunnel M data shown in Figure 27, obtained at $M_\infty \approx 18$ for $D/T \sim 0.15$, the Mach disc is located at $\sim 2.9 \bar{L}$, in good agreement with the Jarvinen-Hill model, which was based on calculations assuming strongly hypersonic external flow. However, for typical ICBM high altitude flight, the freestream Mach number is frequently in the low hypersonic range (see Figure 18) with $M_\infty = 5-6$. Under these conditions the stream static pressure may contribute significantly to mixing layer pressure at $\sim 3\bar{L}$ and location of the Mach disc location at $2.9\bar{L}$ may be incorrect. However, the Mach disc is a relatively low density and thus unimportant structure in the high altitude plume or its ground based aerodynamic simulation. Few Mach discs are actually revealed in flow visualization photographs, because the Mach disc is a relatively low density feature. Although it is in the field of view based on pitot probe surveys (see Table V, Ref. (21), in Figures 24, 25, and 26 of this reference), it is not in evidence. This is particularly striking for case IC2 where the Mach disc should be located in the center of the photograph (Figure 25 of Ref. 4 at $x = 8''$) relatively close to the jet where the merged layer is still visible and the internal jet flow is still fairly dense. Hence, not being a site of high densities and pressures in the high altitude plume (> 100 km) the Mach disc and its location are of relatively little interest in radiation studies of these flows and are not further considered.

4.3 THE MIXING LAYER

The mixing layer is a region characterized by large velocity, temperature and species density gradients. The HAPRAP measurements contain no direct information about mixing layer temperatures (excepting a restricted number of tunnel M measurements) or velocities. Species concentration data are, however, quite detailed and are here the subject of analysis.

The Electron Beam Concentration Surveys

Radial concentration surveys are shown in Figure 28 from case IC5 in tunnel M for three axial stations and from case No. 4 in the ASC(10V) facility for one axial station. These surveys will be discussed in detail to illustrate a number of features of the mixing layer development and difficulties associated with the interpretation of these surveys.

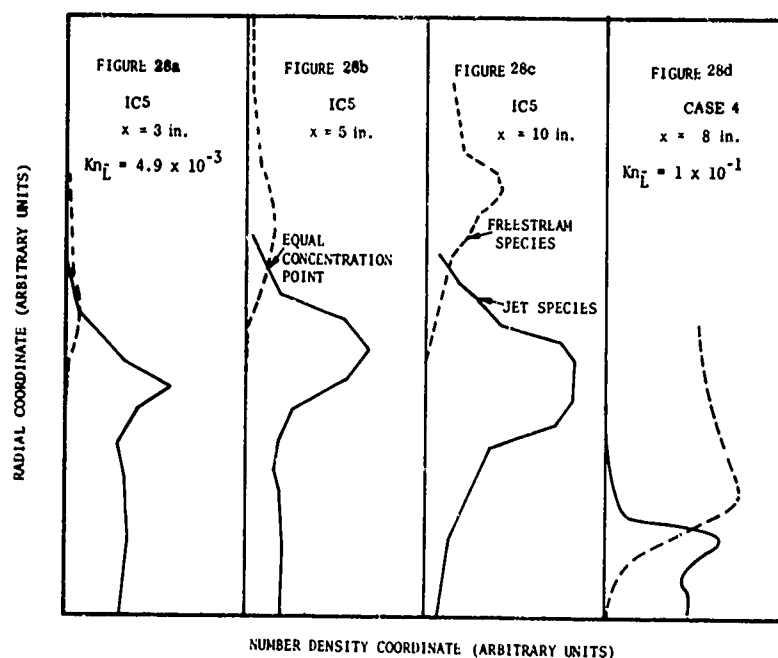


Figure 28 - Typical electron beam surveys

The case IC5 survey at $x = 3''$ of Figure 28a shows the entire mixing layer dominated by the jet species (He). This probably results from entrainment of the jet species into the separated flow around the model and as such represents an improperly scaled effect because of the overlarge model rocket bodies. Once in this separated region the jet species are entrained into the shear layer originating on the forward point of the model, see Figure 29, and substantial amounts of jet species can be injected into the outer regions of the plume mixing layer which

would otherwise contain only freestream species. This forward motion of exhaust products along a rocket body, discussed by Adams and Holland,⁽⁶⁶⁾ is important for relatively large bodies, $l_M/\bar{L} \sim 0.57$ here. Because of the dominance of jet species in the mixing layer at this forward axial station the pitot probe measurements show more details (see Figure 29c of Ref. 21) than the electron beam survey here.

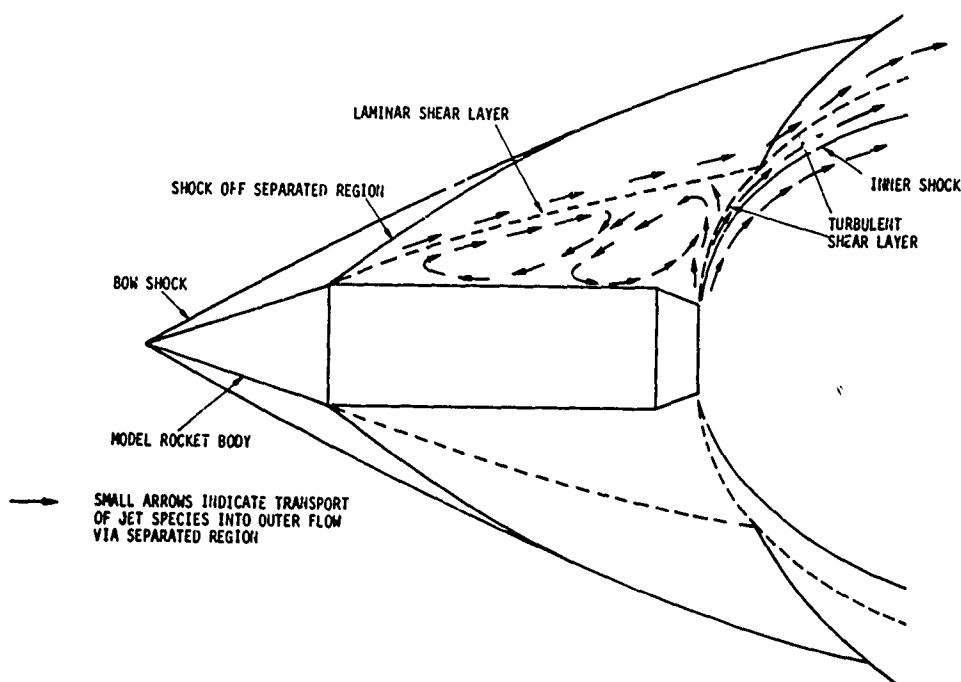


Figure 29 - Separated flow region-medium altitude plume (80-100 km altitude)

At $x = 5''$, Figure 28b, the influence of the separated flow region is less pronounced than at $x = 3''$ and the outer shock structure can be examined in some detail. The freestream mean free path is $\lambda_\infty \sim 0.125$ cm. The shock width based on the steepest slope is $\sim 0.6-0.7$ cm or about $5-6 \lambda_\infty$. This width is consistent with shock measurements^(67, 68) of $4-5 \lambda_\infty$. The significant overlap between the regions of diffusion of the jet and freestream particles inside the shock structure indicate a very viscous flow has been

reached. Strong viscous effects and (possibly) the onset of rarefaction effects are indicated by a weakening in the observed rise in total density across the outer shock. The measured density rise is approximately 3.7, which is to be compared with a value of at least 5.3 calculated from the shock geometry and tunnel conditions. It will be seen later that the plume Knudsen number, $Kn_L \sim 5 \times 10^{-3}$, for this case at these large Mach numbers ($M_\infty = 18$) indicates the continuum-transitional flow boundary is indeed being approached and that the flow is certainly in the viscous-continuum flow domain.

The electron beam survey at $x = 10''$, Figure 28c, is not meaningful for the present study due to interference by the tunnel shock. Pitot probe surveys (Figure 29 of Ref. (21)) show interference between the plume outer shock and the tunnel shock at axial stations beyond $x = 5''$.

Similar plume features are present in the ASC(10V) data. However, since these tests were conducted at values of Kn_L generally larger than in tunnel M , they show stronger cross-diffusion of jet and freestream species, as seen qualitatively in Figure 28d for case No. 4. The large degree of jet-freestream species overlap seen here is a real effect due to the large plume Knudsen numbers (or small plume Reynolds numbers) used to attain the highest altitude ICBM flight simulations shown in Figure 21.

Surfaces of Equal Concentration

The mixing layer density profiles are quite complex as is seen from the measurements of mixing layer dimensions and species profiles.^(21, 37) In the present analysis a single feature of these species concentration surveys is considered. This feature is the surface along which jet and freestream species concentrations are equal,

$$[Z] = [Y] \quad (76)$$

where Z is the jet species and Y the freestream species. This surface is fairly easy to identify from the data (see Figure 28) and provides one indication of the mixing layer location. It is determined from the intersection of two large concentration gradients of opposite sign; therefore, it should be relatively insensitive to reasonably small flow disturbances, such as jet species entrainment forward along the model body discussed above.

The equal concentration surface is of some interest for making chemical calculations in the mixing region. From a study of collateral HAPRAP data it is seen that this surface is located near the higher static temperatures of the mixing region. Specifically the N_2 rotational temperature measurements show that the static temperature reaches a maximum in the vicinity of the equal concentration surface. Further, the electron beam photographs (viz. Figures 24 to 28 of Ref. (21) and Figure 20a of Ref. (37)) show a dark region between the plume outer and inner shock layers that indicates a zone of relatively low density and high static temperature in this region.

For a restricted class of chemical reactions (producing a new species X) or excitation processes involving collisions between freestream and jet species, the equal concentrations surface lies in the region of relatively large volumetric production or excitation rates assuming the volumetric production or excitation rate is the product of a temperature dependent rate times and the product of jet and freestream concentrations,

$$\frac{d[X]}{dt} = k_b \exp \left\{ -\frac{E_{act}}{\Theta_t} \right\} [Z]_s [Y]_s \quad (77)$$

where the subscript s indicates a property along the equal concentration surface and the rate has been written in terms of the reaction rate excitation energy, E_{act} . Therefore, some chemical reactions of interest and associated radiation phenomena may proceed near their maximum volumetric rates along this surface and the equal concentration surface is of interest in relation to the problem of radiation signatures.

The surfaces of equal concentration for the ASC(10V) cases No. 3 and 4, for which D/T and m_∞/m_j are approximately constant, are shown in Figure 30 in normalized coordinates. These data collapse very well compared to the shock structures previously studied. The data show little sensitivity to the disturbing effects of a relatively large model body. The ratio of molecular weights, m_∞/m_j , is not far from unity for these runs. Consequently one may expect that, as viscous transport becomes more important the cross diffusion of jet and free-stream species will have little effect on the location of the equal concentration surface. The contact (pressure balance) surface of the Jarvinen-Hill⁽¹⁹⁾ model shows good agreement with these data. It is seen that even though the detailed flow structure may be rarefield (Kn_L^- increases toward 10^{-1}), inviscid models are still of use in the viscous plume as they give the surface of momentum balance between the jet and freestream such that the plume overall structure still scales with the hypersonic plume scale and is still approximated by continuum calculations. This situation will hold until the largest plume structures breakdown due to lack of collisions on very large scales in the very low density regime.

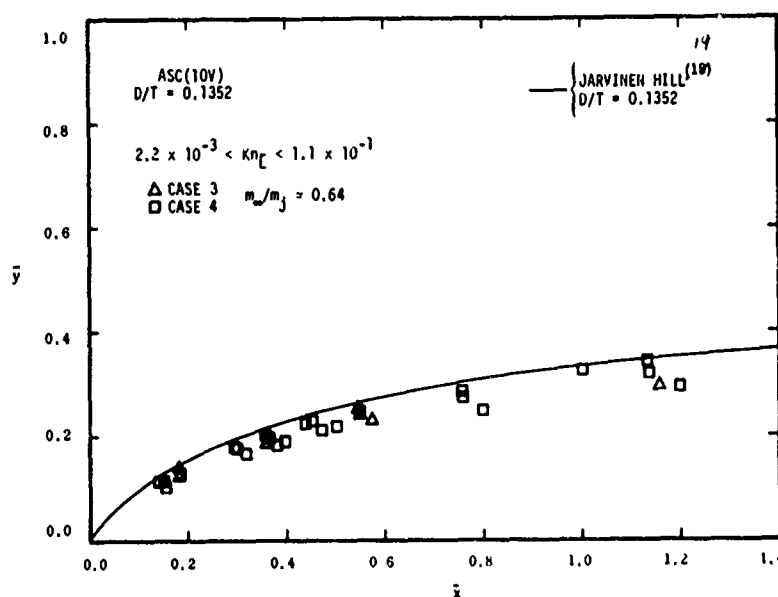


Figure 30 - Surfaces of equal concentration for fixed D/T , m_∞/m_j

Surfaces of equal concentrations are shown in Figure 31 in normalized coordinates with CO_2 and He as jet gases and N_2 and Ar as the freestream gases. In all runs presented here D/T is approximately constant: One might expect a correlation of results for CO_2 and He jets. This is not the case as the He jet equal concentration surfaces are far larger than the CO_2 surfaces. The broader surfaces of equal concentrations for He jets in the normalized coordinates are attributed to the stronger outward diffusion the low molecular weight gas. It is noted, however, that the He test results may also reflect effects of both a relatively larger model body and a jet dynamic concentration calibration which is large by a factor of 2 as discussed in Section 2. A quantitative discussion of the dependence of the locations of surfaces of equal concentrations on m_∞/m_j is coupled to other transport phenomena in the full Navier-Stokes equations and its description is beyond the scope of this work.

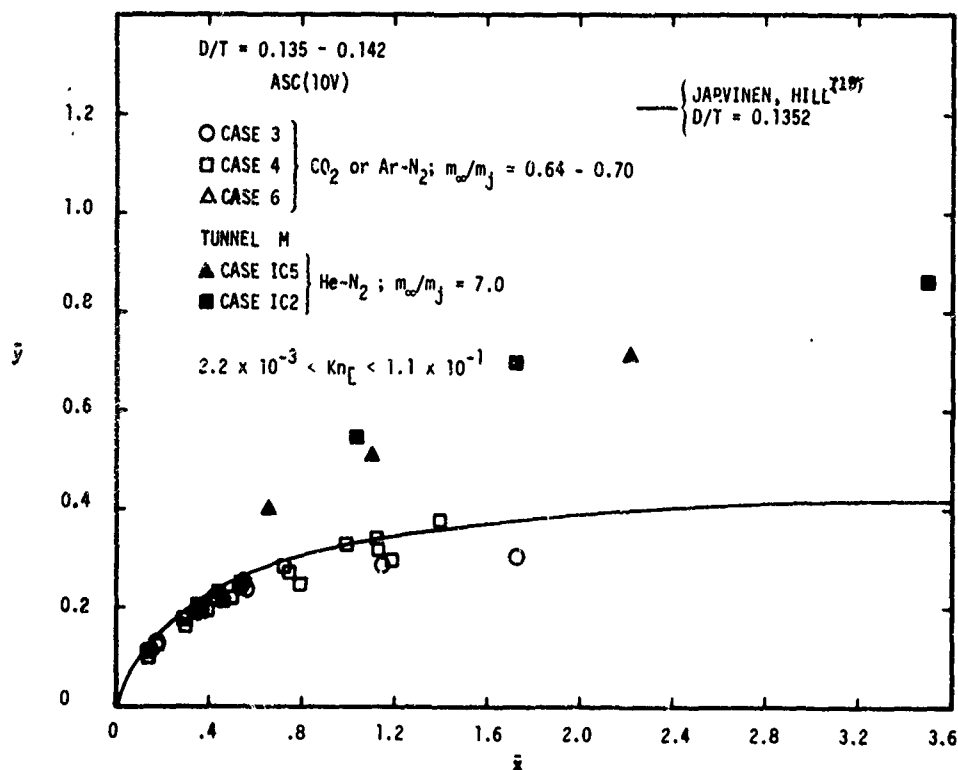


Figure 31 - Surfaces of equal concentrations for varying m_∞/m_j , fixed D/T .

The effect of varying D/T on surfaces of equal concentrations is seen in Figure 32. All runs included here have very nearly the same molecular weight ratio, m_∞/m_j , so that diffusion effects should be equalized. These surfaces grown broader with increasing D/T , a qualitative dependence on D/T in agreement with the Jarvinen-Hill model. However, reduction of these surfaces to a single curve by D/T scaling has not yet been attained.

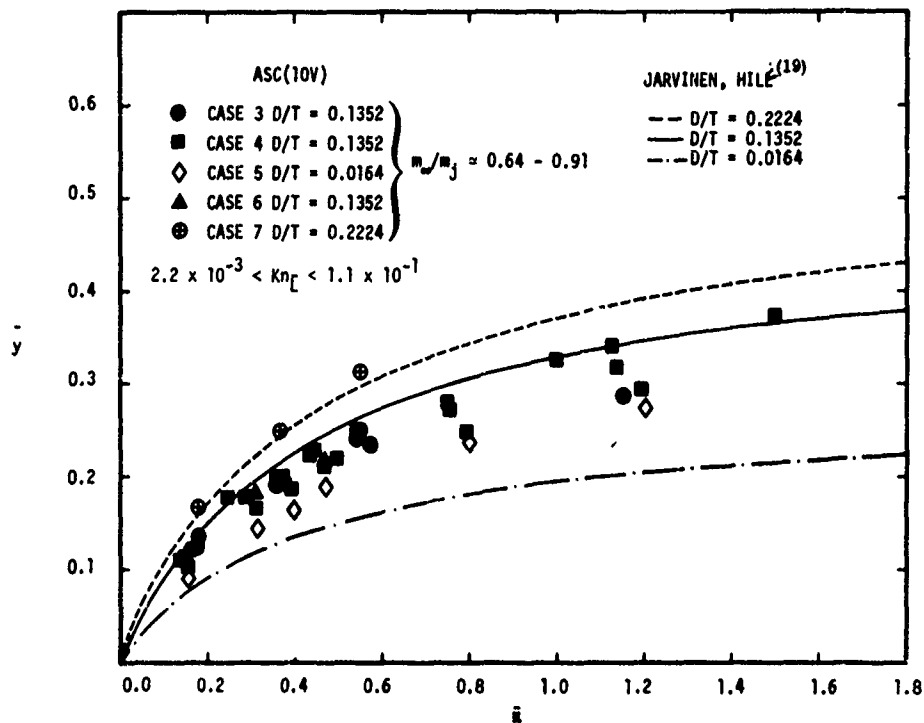


Figure 32 - Surfaces of equal concentrations for varying D/T , fixed m_∞/m_j .

Number Densities Along Surfaces of Equal Concentrations

The species concentrations measured along surfaces of equal concentrations cover a range of roughly 300 as shown in Figure 33. The inviscid concentration of Jarvinen and Hill⁽¹⁹⁾ normalization shown in Equation (29) of Section 1 has been applied to these concentration data with the results shown in Figure 34. The usefulness of the Jarvinen-Hill normalization for inviscid inner

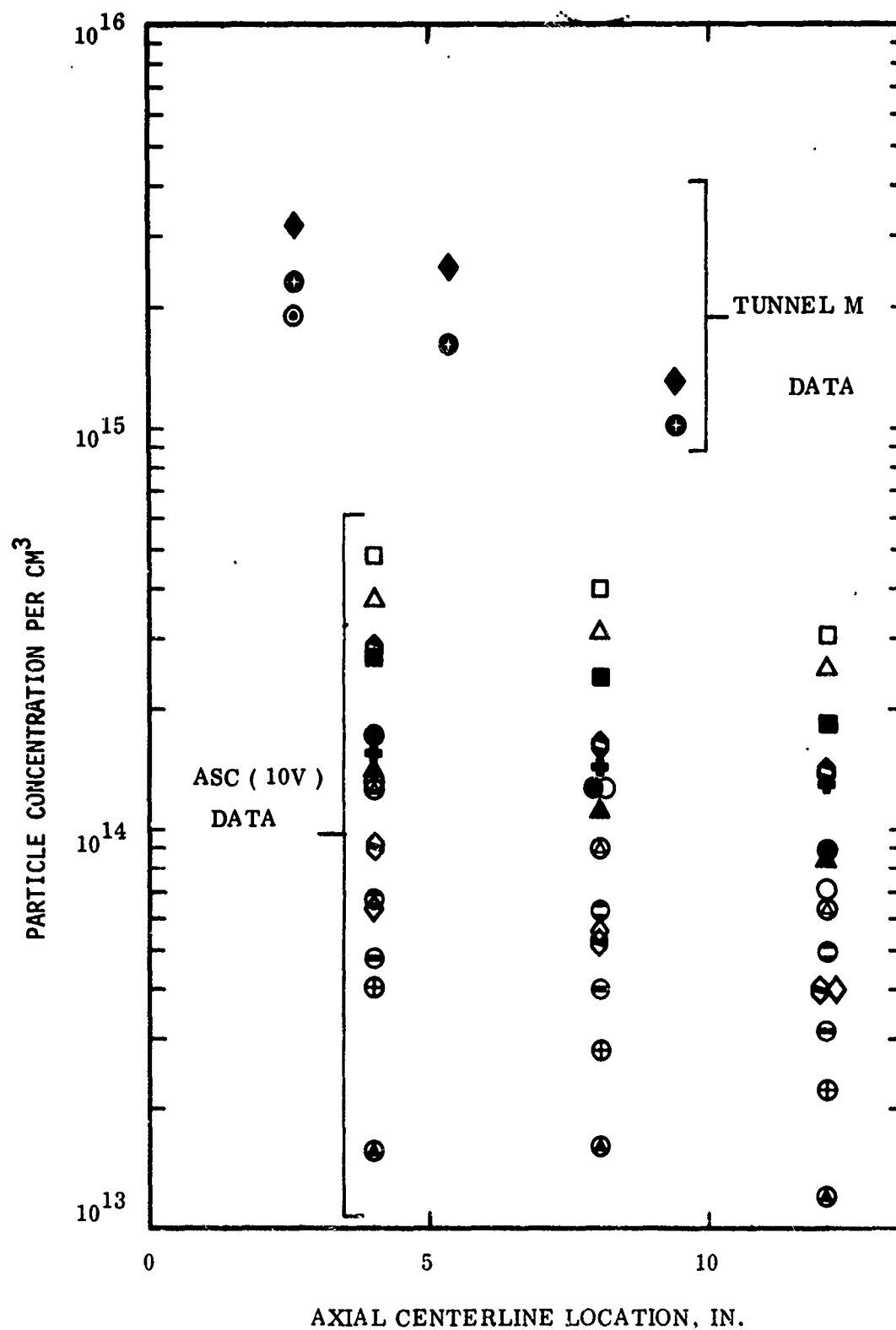


Figure 33 - Concentrations along surfaces of equal concentrations.

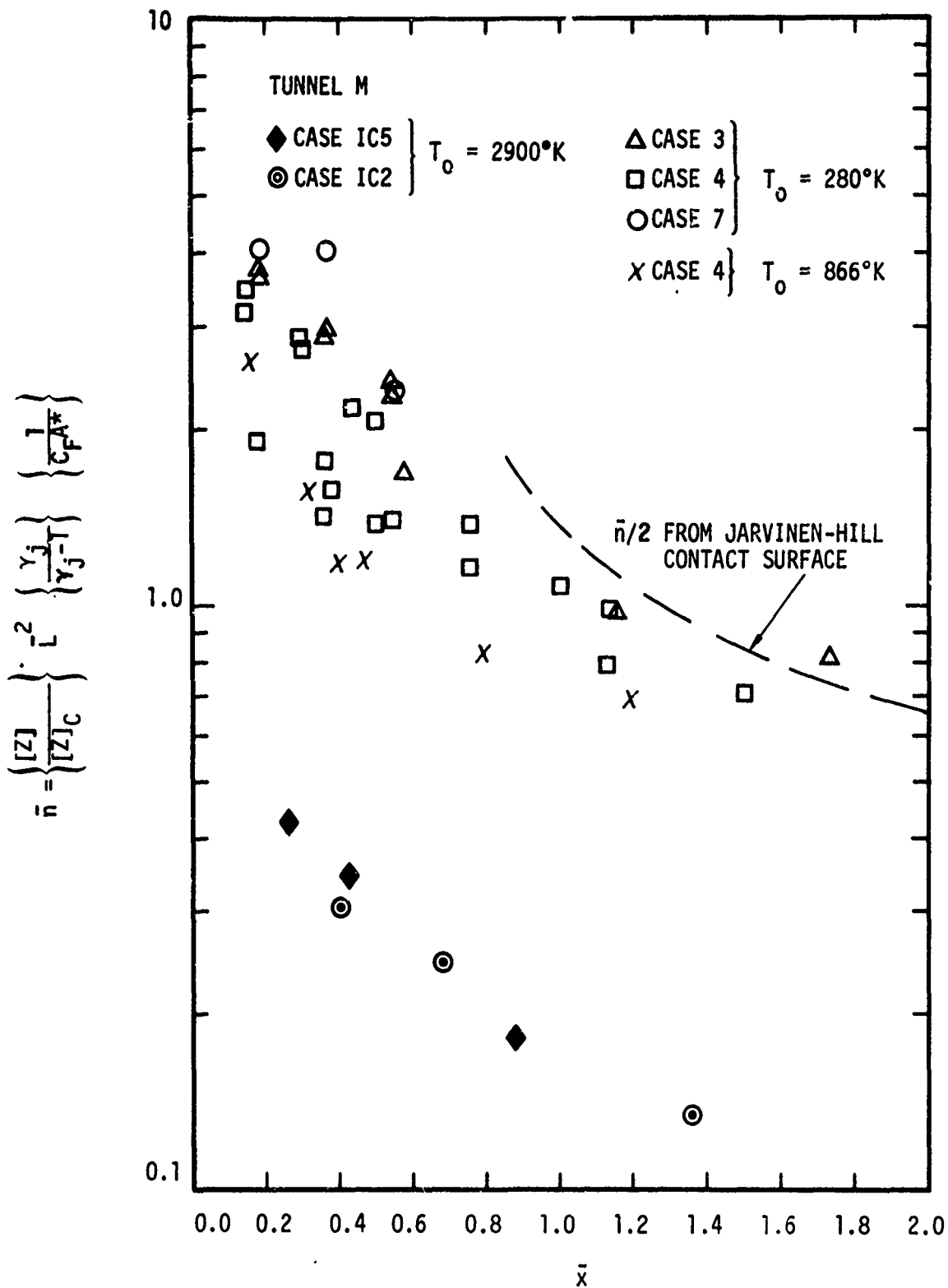


Figure 34 - Normalized concentrations along the equal concentration surfaces

shock layer densities (or concentrations) in correlating viscous shock layer concentration data is quite evident. These normalized concentrations fall roughly into three similar families of curves that are distinguished by different free-stream stagnation temperatures, θ_0 . Also the difference between freestream speed and limiting jet speed, $u_\infty - u_{lim}$, appears to have an effect which is weaker than θ_0 effect and is not so clearly resolved by the HAPRAP test matrix as the freestream stagnation temperature effect.

Normalized data for each θ_0 may be approximated by a single curve with approximately a scatter of $\pm 50\%$. All curves are roughly parallel to that of the model of Jarvinen and Hill normalized density along the inside of the contact surface. For the low θ_0 value ($\sim 280^\circ\text{K}$) the viscous plume concentrations lie only slightly below the inviscid prediction. For the highest θ_0 ($\sim 2900^\circ\text{K}$) the normalized viscous plume concentrations are lower than the Jarvinen-Hill values by a factor of approximately 8 to 10. This behavior of the normalized concentrations results from increased heating in the outer mixing layer region due to the increasing freestream stagnation temperatures. This heating reduces the densities along surfaces of equal concentrations below those corresponding to the inviscid predictions (i.e., those on which the Jarvinen-Hill model is based) in which an adiabatic contact surface is assumed.

An important extension of plume models would be the inclusion of the θ_0 , θ_c , and $u_\infty - u_{lim}$ dependencies in the normalization of concentration to yield a universal curve of equal concentrations for viscous plumes. Such a curve combined with the equal concentration surface pressure would yield temperatures from the perfect gas relation. Thus the state of the gas along the surface of equal concentrations could be estimated.

Pressures Along the Surfaces of Equal Concentration

The pressure along the equal concentration surface is obtained through the Newtonian pressure coefficient and the contact surface local slope in the simple plume models.^(13, 15, 16) Since the simple inviscid model has been found to closely approximate the equal concentration surface in some cases, see

Figures 30-32, it seems reasonable to calculate the equal concentration surface pressure using the same procedure. This procedure for calculating pressure is tested for the tunnel M case IC2 at $x = 5''$ where the N_2 rotational temperature and concentration were both measured at the point of equal jet and freestream concentrations. The tunnel conditions together with the slope of the surface of equal concentrations, $\sigma_\infty \approx 10^\circ$, yield a Newtonian surface pressure of $\sim 11 \text{ NT/M}^2$. The species total concentration is $2[\text{He}]_2 \sim 3.4 \times 10^{15} \text{ cm}^{-3}$ so that, by the perfect gas law, the local static temperature is $\sim 240^\circ\text{K}$. The N_2 rotational temperature measured at this location is in the range of $200\text{--}250^\circ\text{K}$ (see Figure 44 of Ref. (21)).

Unfortunately, there are very few data to test this question since local static temperature was measured in only a few cases. However, pending more extensive measurements, it appears that the use of "universal" curves of equal concentration surface location, normalized concentrations along these surfaces, used with Newtonian surface pressures, and the perfect gas law, will allow approximate determination of the thermodynamic state along this surface. Because aerodynamics and chemistry are incoupled at high altitudes (e.g., see Ref. (23)), aerodynamic simulations in wind tunnels should be sufficient to provide the data required to establish such "universal" curves.

4.4 SUMMARY OF FLOWFIELD ANALYSIS

The flowfield analysis shows that the plume outer shock locations determined by electron beam, pitot probe and flow visualization photography are in substantial agreement once the image slip phenomenon of Section 2 is included. The shock locations show qualitative agreement with the Jarvinen-Hill plume model dependence of \bar{L} and D/T . However, a variety of disturbing effects in the data, such as overlarge model rocket bodies, image slip, and thick mixing layers resulted in a large amount of scatter in normalized shock locations. Moreover, since these shock structures became quite weak in the transitional flow regime which characterized a large amount of the data, these structures are not considered in detail.

The internal shock structure (the Mach disc) shows that longitudinal scaling indeed varies with D/T as discussed in Section 1. This shows the Jarvinen-Hill model is incorrect in assuming this feature is independent of D/T . However, this plume model was designed specifically to describe existing ICBM plumes at high altitudes (i.e., moderate "efficiency" engines with $0.80 < C_F/C_{F_{\max}} < 0.88$), and the HAPRAP data show that for this class of plumes the Mach disc is correctly located at $\sim 2.9 \bar{L}$. Still this modification may be somewhat fortuitous since flight at $M_\infty \sim 6$ the Mach disc position may depend upon both dynamic and static pressure in the freestream. Furthermore, the Mach disc does not appear to be a significant contributor to the high altitude (> 100 km) radiation signature since densities are so low at its location many kilometers aft of the missile. Therefore, the Mach disc is not considered in detail.

The HAPRAP data that constitutes the most novel contribution to the study of high altitude plumes are the detailed, two species, radial surveys of the jet-freestream interaction zone in the forward part of the plume, here taken to be $\bar{x} < 1$. This region plays a significant role in the high altitude radiation signature, therefore dependence of plume features in this region on \bar{L} , m_∞/m_j , D/T , and $Kn_{\bar{L}}$ were studied. Specifically the surface of equal concentrations of jet and freestream species was examined because:

1. It appears to be close to the surface of maximum chemical production for a restricted class of reactions,
2. It is relatively insensitive to the model rocket size,
3. It was found to be a persistent feature easy to identify in all the data for the entire range of the parameters of interest.

The surfaces of equal concentrations were found to be approximately reducible to a single curve (for m_∞/m_j and D/T fixed) when scaled by \bar{L} . Similar scaling was not successful in reducing the plume outer shock data. This single curve (for m_∞/m_j and D/T fixed) was constructed from data over the

plume Knudsen number range, $2 \times 10^{-3} < \text{Kn}_L < 1 \times 10^{-1}$. This curve was in close agreement with the contact surface of the Jarvinen-Hill model for the same D/T. Data with several values of D/T (m_∞/m_j fixed) showed qualitative but not quantitative agreement with the predicted D/T dependence of the Jarvinen-Hill plume model. Increasing m_∞/m_j (D/T fixed) resulted in broader equal concentration surfaces indicating stronger diffusion of the lighter jet species into the heavier free-stream species. In addition to location of surfaces of equal concentration magnitude of concentrations along these surfaces were also studied. It was found that the normalization of inner shock layer density suggested by Jarvinen and Hill is very effective in correlating these concentration data at fixed stream stagnation temperature. For low stream stagnation temperature this correlation is in substantial agreement with the prediction of the inviscid model of Jarvinen and Hill. However, at the higher stream stagnation temperature the normalized concentration lay on a curve which is a factor of 6 or so below the inviscid prediction. It was demonstrated (based on a very limited amount of data) knowledge of the inclination of the surface of equal concentrations, σ_∞ , and used in the Newtonian approximation to the pressure coefficient ($2 \sin^2 \sigma_\infty$), appears to yield the local static pressure along the equal concentration surface.

Section V

RAREFACTION PHENOMENA IN PLUME FLOW

As a missile with a continuum flow regime plume climbs to higher altitudes, the parameter controlling the plume size, \bar{L} , grows as $\lambda_{\infty}^{1/2}$ (for constant missile thrust and speed). If the missile accelerates or stages to lower thrust levels, the length \bar{L} increases more slowly with increasing altitude than $\lambda_{\infty}^{1/2}$. Therefore, the atmospheric mean free path eventually approaches the plume size and the flowfield passes out of the range at which continuum concepts apply. We will consider one a description of this process and a suitable parameter for specifying how far this rarefaction process has advanced. Particular consideration will be given to the continuum plume flow as it enters the transition regime.

5.1 PREVIOUS WORK

The appearance of noncontinuum flow effects in the high-altitude plume flow has, until recently, come under relatively little discussion. Hill and Habert,⁽¹⁰⁾ Alden and Habert,⁽²³⁾ and Thompson *et al.*,⁽¹⁸⁾ all touched on the question theoretically. Muntz, Hamel, and McGuire⁽⁶⁹⁾ established a solid basis for the study of plume rarefaction by carrying out the first experimental study of Mach disc rarefaction in an underexpanded jet with no external flow. They formulated rarefaction of these shock structures in terms of a parameter dependent upon the background or static pressure appropriate to the plume in a stationary ($M_{\infty} = 0$) environment. However, static pressure has no significance for the hypersonic plume structures considered here which are dominated by impact pressure. Moreover, in the high-altitude plume, the Mach disc is a low density structure rather distant downstream from the head of the plume and it tends to contribute negligibly to radiation signature.

Muntz⁽⁷⁰⁾ subsequently formulated the rarefaction problem for jet plumes in an atmosphere moving coparallel to the jet axis. His analysis began in the

scattering regime by calculating a surface in the jet flow where a single atmospheric molecule would first collide with the jet species. The resulting surface is similar to a paraboloid with a nose radius, R_N , which is on the order of the exponential penetration distance of the ambient gas into the jet, r_p . A "plume Knudsen Number" is then defined by

$$K_{NP} = \frac{r_{1/e}}{R_N} \quad (78)$$

where $r_{1/e}$ is the exponential length scale of the attenuation of the jet species (with respect to its undisturbed $1/r^2$ distribution) by the background and $r_p \approx R_N$ is assumed in Equation (78).

Muntz defines the density regime boundaries as

$K_{NP} = 1$	"Scattering High Density Limit"
$K_{NP} = 0.1$	"Thick Shock Waves"
$K_{NP} = 0.01$	"Merged Flow"

The scattering high density limit is the point at which the jet gas distribution becomes significantly disturbed on the same scale as the ambient particle distribution, and the two effects interact strongly with each other. At lower densities, the jet disturbance occurs only on the scale of the ambient mean free path while the ambient boundary is entirely controlled by the jet density. The boundary is located along the first collision surface described by Muntz and never penetrates significantly to the nozzle as $Kn_e \ll 1$ for the class of vehicles discussed here. The plume flow is certainly in the "scattering regime" when $r_{1/e} \gg r_p$. For higher density flows, $K_{NP} = 0.1$, the jet and ambient penetration distances are increasingly affected by multiple collisions which lead to a density buildup in the freestream-jet interaction zone. This region, termed "thick shock waves" by Muntz, marks the first appearance of a freestream jet species interaction sufficient to strike a momentum balance between the flows. It is probable that this

is the region in which the continuum scaling with \bar{L} first appears in the large dimensions of the plume structure but the small details still behave as λ_∞ .

Muntz considers $K_{NP} = 0.01$ to be a merged flow regime in which the interaction zone shocks have decreased in scale until they become of the order of the interaction zone thickness. At this point, the jet species ceases to penetrate into the outer ambient flow altogether and the \bar{L} scaling becomes firmly established. Muntz presents a thrust-altitude "rarefaction diagram" of the form of Figure 35 to aid in determining the altitudes at which missiles encounter these rarefaction criteria. It is noted that, as Muntz assumes a constant relationship between freestream and jet velocities to simplify his rarefaction diagram, these curves do not exhibit a dependency upon the flow velocities. In fact, the jet and freestream velocities do affect calculation of these criteria for the general case. Muntz analysis appears best suited to defining the scattering-transition boundary rather than the continuum-transition boundary.

Simons⁽⁷¹⁾ discussed rarefaction of the principal plume structures in the continuum, transition, and scattering regimes. The merging of the bow shock with the mixing layer and the departure of the bow flow from the continuum regime are both considered in terms of the Reynolds number behind the shock, Re_2 , for which experimental values at merging and transition are quoted. Using approximations for the flow properties and the normal shock relations, Simons expressed the continuum-transitional boundary criterion in terms of the plume nose radius, R_{NP} , and the ambient mean free path. Simons quotes, from Ahouse and Bogdonoff,⁽⁷²⁾ an experimental value of R_b/λ_∞ which is observed to correspond to the onset of noncontinuum behavior in blunt solid body flow:

$$\frac{R_b}{\lambda_\infty} = 40 \quad (79)$$

where R_b = the body nose radius. Simons, based on these experimental results, determine the continuum-transitional flow boundary to be at $Re_2 = 30$. This boundary is shown with Simons' shock-mixing layer merging boundary, at

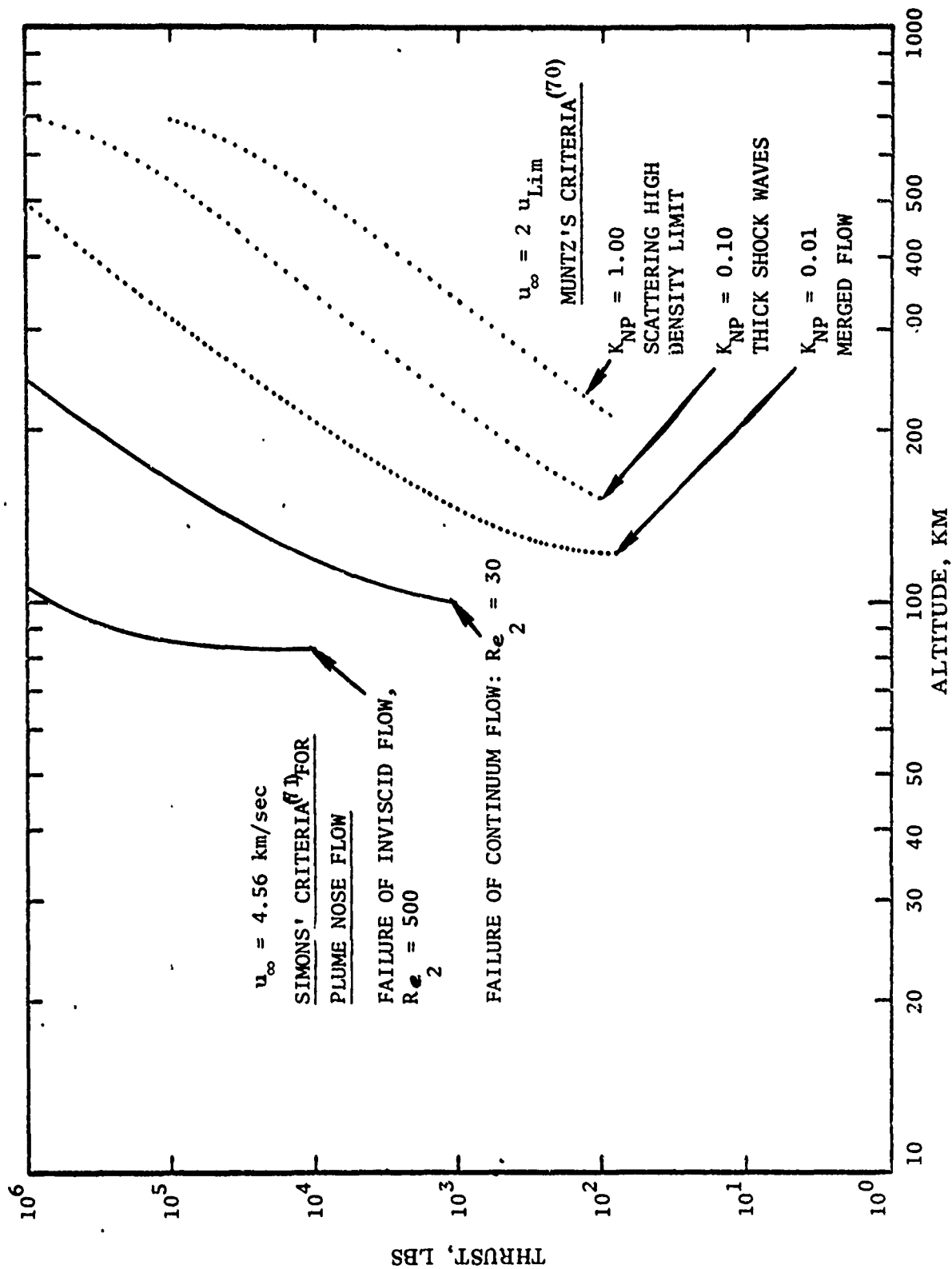


Figure 35. Rarefaction Diagram showing Simons' results for continuum transitional boundary and Muntz's for scattering regime boundary.

$Re_2 = 500$, on Figure 35. Notice for $\gamma_\infty = 1.4$ and $D/T = 1/6$, that $R_s \sim L/7$ from Equation (4). Where $R_s = R_b$ is assumed, this value of R_b can be used in Equation (79) to obtain a value of Plume Knudsen number

$$Kn_{\bar{L}} = \frac{\lambda_\infty}{\bar{L}} \sim 4 \times 10^{-3} \quad (80)$$

that corresponds to the appearance of rarefaction effects in the plume nose exterior flow as proposed by Simons. It is important to note that $Kn_{\bar{L}}$ is a continuum regime plume Knudsen number, defined in Equation (33), as contrasted with Muntz, rarefied regime plume Knudsen numbers K_{NP} defined in Equation (78).

Simons' plume nose radius, $R_{NP} \approx 0.42 \bar{L}$, is about three times Hill and Habert's⁽¹⁰⁾ plume nose radius (R_s for $\gamma_\infty = 1.4$) described in Section 1. There, on the basis of a correlation of the blast wave expression with observations of high altitude plumes, it was concluded that R_s is a good approximation of the plume nose radius. However, since Simons uses $R_{NP}/3$ as his length scale, his continuum-translational boundary should be approximately correct.

Simons also discusses failure of continuum flow in the region of the Mach disc. However, since in the present study the Mach disc is considered to be of secondary importance, no further consideration is given to it here. Finally, Simons considers the particles scattered by the "continuum core" of the plume in his estimation of the perturbation of the freestream particles rebounding from this continuum core. The dimension chosen is the distance from the jet nozzle to the onset of translational mode freezing. The mean free path for the freestream species in the jet differs from that for jet species self collisions. Therefore, it is not evident that the distance to the jet species translational freezing point is an appropriate one for describing the extent of the jet core region, off which the freestream species scatters. Simons' work, therefore, is best suited to describing

the rarefaction of the continuum plume nose while Muntz's work is most appropriate for describing the scattering plume and, thus, their results complement each other, as illustrated in Figure 35.

When the continuum merged freestream shock layer enters the transitional regime, the particle self collisions become insufficient to maintain full translational equilibrium. Then the freestream kinetic energy is not fully redistributed into an isotropic Boltzmann distribution of velocities, i.e., completely "thermalized." This event can have important implications for calculation of plume radiation signatures. When thermalization is not attained, the use of chemical rates based on the Arrhenius formulation may not express the actual chemical and upper state excitation rates. Vogenitz⁽⁷³⁾ has carried out Monte Carlo calculations of the plume nose flow field in which strong rarefaction effects, i.e., large departures from an equilibrium velocity distribution appear. He has demonstrated that such effects may result in radiation levels orders of magnitude different from the corresponding equilibrium velocity distribution prediction for high altitude rocket operation of interest.

Significant deviations from the fully thermalized (isotropic Boltzmann velocity distribution) occur when the total number of particle self-collisions becomes small. The total number of collisions the particle encounters in the plume nose cap region, N_s , can be obtained in the form,

$$N_s \propto (M_\infty Kn_L)^{-1} \quad (81)$$

This shows, that, as one aspect of an increasingly rarefied plume moving across the continuum-transitional boundary, a "thermalization" boundary or criterion can be appropriately expressed in terms of the plume Knudsen number, Kn_L .

5.2 SCALING AND NONTHERMAL EFFECTS OF RAREFACTION

5.2.1 Continuum-Transitional Flow Regime Boundary Based Upon Dimensional Scaling Considerations

Flow field properties cannot be adjusted by collisions over distances less than a few mean free paths. In the continuum regime where $Kn_L \ll 1$, the flow field properties are continuously adjusted by collisions on distances very small compared to the overall plume flow scale. In the extremely rarefield scattering regime where $Kn_{NP} \gg 1$, freestream molecules collide with the plume jet structure, are caught up in the exhaust jet, and are ejected back into the freestream, creating only small perturbations in the oncoming freestream molecular flow (this phenomena has been sketched by Muntz⁽⁷⁰⁾). This oncoming flow cannot penetrate the jet flow near the nozzle because the engine exit plume Knudsen numbers, for the devices considered here, are quite small compared with unity. Thus, as the freestream does not affect the central jet flow, these freestream particles penetrate the jet flow to a point determined solely by engine design and, after ejection from the dense jet regions, travel a distance controlled only by the freestream mean free path.

Between the continuum and scattering regimes is a transitional region where the continuum shock structures on each side of the mixing layer spread out and merge into each other, so the discrete continuum identities are lost. However, the local densities are appreciably increased by flow interactions (compared to the full scattering regime case) so as to form a specific mixing region structure on a scale large compared to the mean free path. In the transition region, because there is a significant interaction between the freestream and jet particles, we find that the large scale mixing layer structure dimensions are controlled by the jet-freestream momentum balance since this balance involves many collisions on distances of the order of the large structure dimension \bar{L} . On the other hand, the details small compared to \bar{L} , such as merged layer widths, tend to vary as λ_∞ , the rarefied flow scale. Thus both continuum and scattering regime scaling laws appear in the transitional regime.

The transitional regime scaling dichotomy can be demonstrated by study of the HAPRAP data. It is seen in Figure 30 that the overall merged layer structure appears to scale satisfactorily with \bar{L} for plume Knudsen numbers up to $Kn_{\bar{L}} \sim 10^{-1}$. It will now be shown that the smaller scale structure begins to vary with λ_{∞} before this limit is reached. The smaller scale structure to be studied will be the thickness of the freestream species concentration in the merged layer. The thickness chosen, δ' , is the width of the freestream species peak taken half way between the peak concentration in the merged layer and the freestream concentration. The HAPRAP data for δ'/λ_{∞} is plotted against $Kn_{\bar{L}}$ in Figure 36 where the dimension δ' is shown graphically.

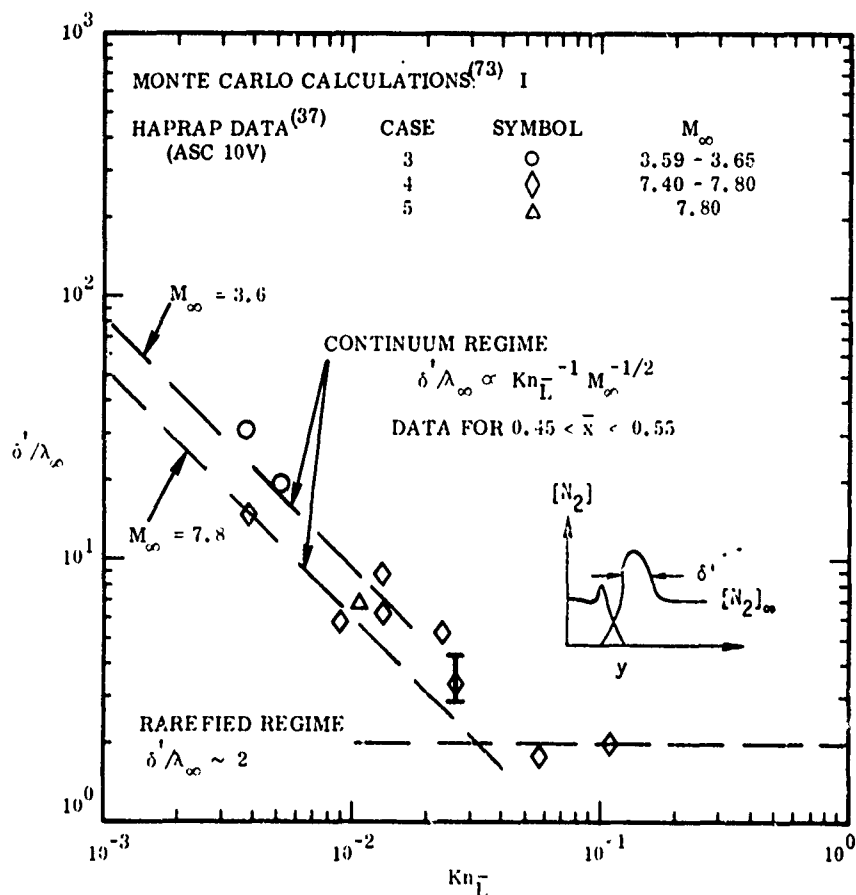


Figure 36. HAPRAP plume small scale structures normalized by the ambient mean free path plotted vs the plume Knudsen number to show transitional scaling of the small scale structures

Before discussing the significance of Figure 36 several details require comment. All of the data were chosen at, or averaged to, axial stations in the interval of $\bar{x} = 0.45$ to 0.55 to insure a constant degree of development of the viscous layer. In order to avoid large model rocket body disturbances, data from large ($\ell_m/\bar{L} > 0.5$) rocket bodies were not included. The freestream mean freepath evaluation was carried out in two ways:

1. Values of λ_∞ were calculated using the expression

$$\lambda_\infty = 6.6 \times 10^{-6} \left[\frac{2.68 \times 10^{19}}{1.67 [N_2]_\infty} \right] \text{ cm} \quad (82)$$

The freestream concentrations $[N_2]_\infty$, measured by the electron beam have been multiplied by 1.67 to account for the freestream calibration shift discussed in Section 2.

2. The values of λ_∞ at the nozzle exit are given in Figures 4 and 5 of Reference (37). As the flow field impact pressure drops about a factor of 2 from the nozzle exit to the middle of the simulated plumes in the ASC(10V) facility the local value of mean free path was approximated by 2 times that tabulated in Reference (37).

The overall agreement between these two methods of data reduction was reasonably good. Detailed differences were probably due to freestream flow perturbations by the plume and scatter in the electron beam $[N_2]$ measurement. The data shown in Figure 36 were obtained using the second method.

A second comment on Figure 36 relates to the limits of the continuum and rarefied regime behavior indicated by the broken lines. The continuum regime behavior is based on Equation (36) of Section 1 and shown by the two diagonal lines on the left of the figure. The lower line has been fitted to the $M_\infty = 7.8$ data for the lowest values of Kn_L . The upper line has been drawn

parallel to the first using the relation $\delta'/\lambda_\infty \propto M_\infty^{-1/2}$ for Kn_L constant and labeled $M_\infty = 3.6$. This second, upper line appears in better agreement with the available low Mach number data than the first line. In the rarefied regime a horizontal line at $\delta'/\lambda_\infty = 2$ has been drawn to suggest the behavior of the mixing layer structure in this limit.

A final comment relates to the Monte Carlo calculations of Vogenitz⁽⁷³⁾ indicated by the short vertical bar in Figure 36. The calculation shown is taken from calculations for a coparallel plume nose region flow at 200 km altitude generated by a rocket of 60,000 lb thrust moving at a speed relative to the ambient of 5 km/sec. Using the standard atmosphere⁽²³⁾ this corresponds to a freestream Mach number of 6.85 which is close to that of the HAPRAP ASC(10V) case No. 4 and 5 data shown in Figure 36. Density profiles from the Monte Carlo calculations are available along a specific cut through the plume nose structure.⁽⁷³⁾ This profile can be treated as a measurement from a "numerical experiment" yielding a value of δ'/λ_∞ . This value of δ'/λ_∞ is obtained at a distance of about a nose radius from the forward point of the nose flow, i.e., $\sim 0.15 \bar{x}$ downstream from the origin of the nose flow. The data in Figure 36 all corresponds to flow at $\sim 0.5 \bar{x}$. To compare the Monte Carlo calculations to the HAPRAP data we make the assumption that $\delta'/\lambda_\infty \propto \bar{x}^{1/2}$ for Kn_L and M_∞ fixed. From Equation (1) we find $\bar{L} \sim 7.5$ km so that $Kn_L \sim 0.026$. This allows the Monte Carlo "data" to be located by the vertical bar on Figure 36 where the vertical range allows for scatter in the calculations and for the effect of range in \bar{x} from 0.4 to 0.6.

For $Kn_L < 1 \times 10^{-2}$ Figure 36 indicates that there are at least 6 to 10 freestream mean free paths in δ' and that the flow is consistent with viscous continuum behavior. For $Kn_L > 3 \times 10^{-2}$ the flow exhibits very thickened shock structures in which viscous effects certainly play some role. However, by $Kn_L \sim 1 \times 10^{-1}$ the δ' structure appears fully rarefied. This condition corresponds to a very weak ambient species compression of a factor of 1.4, another indication of rarefied flow. It appears that by $Kn_L \sim 1 - 3 \times 10^{-2}$ rarefaction effects appear in the HAPRAP data. While $Kn_L \sim 1 - 3 \times 10^{-2}$ may appear to

be a small Knudsen number for rarefaction effects to appear, bear in mind that, for convenience $Kn_{\bar{L}}$ is defined in terms of the hypersonic scale, \bar{L} . In terms of the plume nose radius the "body" Knudsen number is substantially larger, on the order of 0.1-0.2.

The suitable HAPRAP data is of restricted extent, however, it does supply experimental observations about an important fact: the plume Knudsen numbers for which parts of the plume flow show important rarefaction effects. Via the simulation study of Section 3, those plume Knudsen numbers together with rocket trajectories indicate when such rarefaction effects appear in plume flows. The Monte Carlo value of δ'/λ_{∞} fits well into the HAPRAP data. This result will become more important in the next section where another aspect of the appearance of rarefaction phenomena is considered.

Two crucial features of the dimension of δ' are that it increases with distance along the plume (like $\sim \bar{x}^{1/2}$) and that it is ambiguous when we move from the viscous - continuum to the inviscid - continuum regime. The first feature means that the rarefaction criterion will vary (relatively slowly) from location to location in the plume. The second indicates that care must be taken in the definition of δ' . In the inviscid-continuum regime ($Kn_{\bar{L}} \ll 10^{-2}$) if δ' were taken to be the entire shock layer thickness it would be independent of λ_{∞} . This regime is not encountered in the present data body which lies entirely within the viscous-continuum or transitional flow regimes for which the entire shock layer is viscous.

To estimate the approximate values of plume Knudsen numbers for which the small scale (i.e. on the order of δ') and large scale (i.e. on the order of \bar{L}) plume flows will first show rarefaction effects we will assume that when the flow scale of interest approaches three freestream mean free paths then rarefaction effects will set in on that scale.

The plume nose radius, R_s , given by Equation (4), is $\sim R_{\bar{L}}/7$. For the large values of γ_{∞} encountered at high altitudes the shock layer thickness is estimated by $\Delta \sim R_s/10$. The first effects of rarefaction are expected to appear in the plume nose flow shock layer when

$$\lambda_{\infty} \sim \frac{\Delta}{3} \sim \frac{R_s}{30} \sim \frac{\bar{L}}{210} \quad (83)$$

or for,

$$Kn_{\bar{L}} \approx 0.005 \quad \left\{ \begin{array}{l} \text{plume nose flow continuum-transition} \\ \text{boundary} \end{array} \right. \quad (84)$$

Likewise, the overall plume (i.e on the scale of \bar{L}) will "leave" the transition regime when $\bar{L} \sim 2$ to $3 \lambda_{\infty}$ or when

$$Kn_{\bar{L}} \sim 0.3-0.5 \quad \left\{ \begin{array}{l} \text{plume transition-scattering} \\ \text{boundary} \end{array} \right. \quad (85)$$

The data in Figure 36 is applicable at $\bar{x} \sim 0.5$ or about $4R_s$ lengths downstream along the plume. Assuming the merged shear layer structure grows as $x^{1/2}$ then the criterion in Equation (84) applied to $\bar{x} \sim 0.5$ gives

$$Kn_{\bar{L}} \sim 0.010 \quad \left\{ \begin{array}{l} \bar{x} = 0.5 \text{ continuum transition} \\ \text{boundary} \end{array} \right. \quad (86)$$

This is on the order of plume Knudsen number at which the small scale flow structure begins to show local rarefaction effects in the HAPRAP data of Figure 36. The value given in Equation (83) is also in rough agreement with the value Simons⁽⁷¹⁾ quotes for the plume nose.

The HAPRAP data all lie on the continuum-transitional side of the transition-scattering regime boundary which lies in the vicinity of $Kn_{\bar{L}} \sim 0.3-0.5$. They also lie on the viscous-continuum side of the inviscid-viscous boundary which lies in the vicinity of $Kn_{\bar{L}} \sim 5 - 8 \times 10^{-4}$. In sum, the range of plume Knudsen

number characterizing the HAPRAP data, $0.002 \leq Kn_L \leq 0.10$, show that these data lie in the viscous-continuum and transitional density regimes a region important for typical ICBM flight as shown in Figure 21.

5.2.2 Continuum - Transitional Flow Regime Boundary Based Upon Nonthermal Considerations

Beside affecting the flow scaling the onset of the transitional regime will have an important effect on flow chemistry and excitation processes. Moreover, since the rarefaction effect studied above depends on observations of density, the zeroth moment in the Boltzmann equation, its behavior should not be as sensitive an indicator of rarefaction effects as properties related to higher moments, such as particle mean energy. An estimate of rarefaction effects is now made from the point of view of insuring a sufficient number of collisions in the shock layer that the ambient particle kinetic energy is redistributed. Most of the chemical calculations for the continuum flow shock layer excitation and chemical processes carried out using the Arrhenius rate formulation implicitly assume an isotropic Boltzmann distribution of velocities in which the flow kinetic energy is "thermalized." It has been shown by Vogenitz⁽⁷³⁾ that this assumption can lead to errors of orders of magnitude in predicted radiation levels in transition flow regime plumes.

Bow shock layer continuum properties are established via collisions which drive the particles (assumed to be hard spheres here) toward a local translational equilibrium. This equilibrium is quickly established, e.g., within ~ 2 -3 collisions in the interior of a shock wave. Here it will be assumed that the plume bow shock layer will be "fully thermalized" if a particle encounters 10 collisions in one-tenth the flow time through the plume nose stagnation region or a total of 100 collisions in this same region. "Fully thermalized" will be taken to mean that the directed incident flow energy is essentially redistributed into an isotropic Boltzmann velocity distribution and conventional full equilibrium excitation and chemical calculations can be carried out. For fewer collisions it will be assumed that the significant departures from the isotropic Boltzmann velocity distribution will occur.

Thirty to one hundred collisions in the shock layer will be assumed to constitute "partial thermalization" under which conditions the bow shock layer velocity distributions are significantly nonthermal. The velocity distributions may then have a significant cold molecular beam type mode contribution on top of the hot thermalized contribution. Conventional chemical calculations must be regarded with skepticism. Three to thirty collisions will mark the boundary of the full-scattering regime in the nose cap region. It is emphasized that, as there is as yet not experimental evidence for when such nonthermal effects first occur, these statements are conjectures.

The hypersonic plume scale is about an order of magnitude larger than the nose cap scale so the particles leaving a nose cap with only 3-10 collisions still undergo a significant thermalization (i.e. many collisions) further downstream on the plume. However, most of the particles downstream along the plume will not have originated from the stagnation region. They will have entered the interaction region somewhere downstream of the stagnation region with correspondingly fewer collisions to insure thermalization. This lack of collisions for the free-stream species entering the interaction region will be enhanced by the "pumping" of the coparallel jet surface on the freestream, delaying buildup of freestream perturbations in the transition-scattering regime as suggested by Muntz.⁽⁷⁰⁾ It appears that once thermalization fails in the plume nose region it will soon fail downstream along the hypersonic plume structure ($\bar{x} < 1$).

The number of collisions an average particle encounters in traversing the thermalized shock layer is the product of the collision frequency and the flow time. Talbot⁽⁷⁴⁾ has shown that the number of collisions in the stagnation region of a blunt body can be written as:

$$N_s \sim \left(\frac{\rho_s}{\rho_\infty} \right)^{3/2} \frac{Re_\infty, R_s}{M_\infty^2} \left(\frac{T_s}{T_\infty} \right)^{1/2} \quad (87)$$

where Re_{∞, R_s} is the unit Reynolds number based on the body nose radius and upstream conditions. By use of the strong shock relations, Equation (4) and Equation (61) and assuming $\gamma_{\infty} = 1.4$ we can write

$$N_s \sim \frac{3.6 (D/T)^{1/2}}{Kn_L^-}$$

$$\sim \frac{1.5}{Kn_L^-} \quad \text{for } D/T = \frac{1}{6} \quad (88)$$

For typical ICBM missiles ($D/T \sim 1/6$) failure of flow thermalization ($N_s \sim 100$ collisions) will set in by $Kn_L^- \sim 1.5 \times 10^{-2}$. This value of plume Knudsen number falls at approximately the first appearance of rarefaction effects in the small scale structure as determined above.

For larger values of Kn_L^- than 1×10^{-2} chemical calculations assuming full equilibrium of particle energies must be carefully examined to insure meaningful results. Examination of the above mentioned Monte Carlo results⁽⁷³⁾ helps to establish the order of error involved when assuming full translational equilibrium when $Kn_L^- > 1 \times 10^{-1}$. These results have been shown in Figure 36 to lie at $Kn_L^- \sim 0.026$, a region of significant rarefaction on the small scale in the plume flow. This conclusion is underlined when the results for the mean particle energy in the ambient species compression are examined. It is seen (in Figure 2-4 of Reference (73)) that the mean particle energy at the peak of the plume mixing layer freestream species concentration is twice as large in the freestream flow direction as compared to the two orthogonal directions. Thus the available evidence shows that substantial deviations from full thermalization occur in high altitude hypersonic plumes by plume Knudsen numbers of $\sim 3 \times 10^{-2}$.

5.3 RAREFACTION IN HIGH ALTITUDE ROCKET PLUMES

The above results can now be compared with the results of the previous workers in a rarefaction diagram. A rarefaction diagram also shows what implications these results hold for high altitude missile flight. Such a diagram is shown in Figure 37. The three solid curves shown the altitude at which a given thrust vehicle moving at a speed of 4 km/sec reaches three successive plume Knudsen numbers: the value of plume Knudsen number of 1×10^{-2} corresponds (approximately) to a first appearance of rarefaction on the small scale; the value of 1×10^{-1} for fully rarefied small scale flow; and a plume Knudsen number of 3×10^{-1} for the breakdown of the continuum behavior on the large scale. This last curve, for the breakdown of large scale continuum behavior, is itself based on concepts of continuum concepts which are in question as the flow enters the scattering regime. It is therefore of questionable applicability. The first two curves, however, originate from examination of the HAPRAP data and correspond to the continuum and transitional flow regimes which are the principal regions of interest in this analysis.

Also shown by the dotted lines is how the previous work compares with the indications of the HAPRAP data. We have plotted the point at which continuum flow theory fails according to Simons⁽⁷¹⁾ for freestream speeds of 4.56 km/sec. This criterion is itself based on blunt body rarefied flow experiments. Simons' criterion is in substantial agreement with the curve for the first onset of rarefaction effects that has resulted from study of the HAPRAP data. In the scattering regime, Muntz⁽⁷⁰⁾ shows what he terms the scattering high density limit in the region of breakdown of the overall continuum flow. This work is based on concepts suitable to this rarefied regime and his work is the better guide for the actual phenomenology of this region.

The extent of the HAPRAP simulation, corresponding to a range of plume Knudsen numbers from $\sim 2 \times 10^{-3}$ to 1×10^{-1} , is shown in terms of altitudes and thrusts. A very substantial portion of high altitude missile flight is simulated in these measurements. Smaller thrust vehicles are simulated at correspondingly lower altitudes. The altitude range of the simulation range is smaller at lower

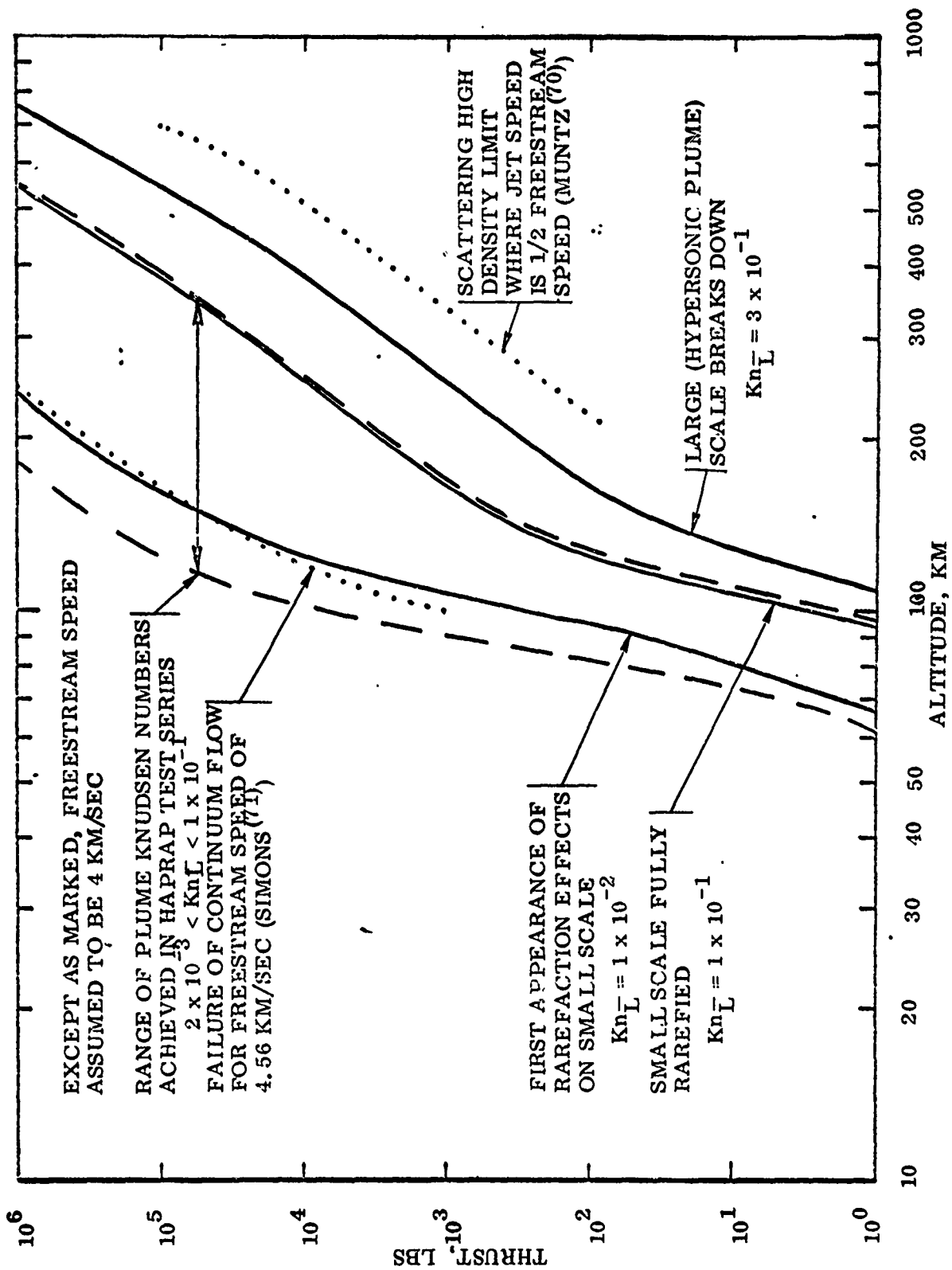


Figure 37. Rarefaction diagram showing density regime boundaries and range of simulation of ICBM flight achieved in HAPRAP flow interaction study.

altitudes due to a smaller atmospheric scale height. It appears that the HAPRAP flow interaction data encompass a very interesting and important range of rocket flight for a very wide variety of thrust levels.

Because the plume hypersonic scale depends on flight speed so will the plume Knudsen number and thus the degree of significance of rarefaction phenomena. The effect of flight speed on the rarefaction diagram is shown in Figures 38 and 39 (neglecting the effect on the rarefaction criteria due to variation in flight Mach number).

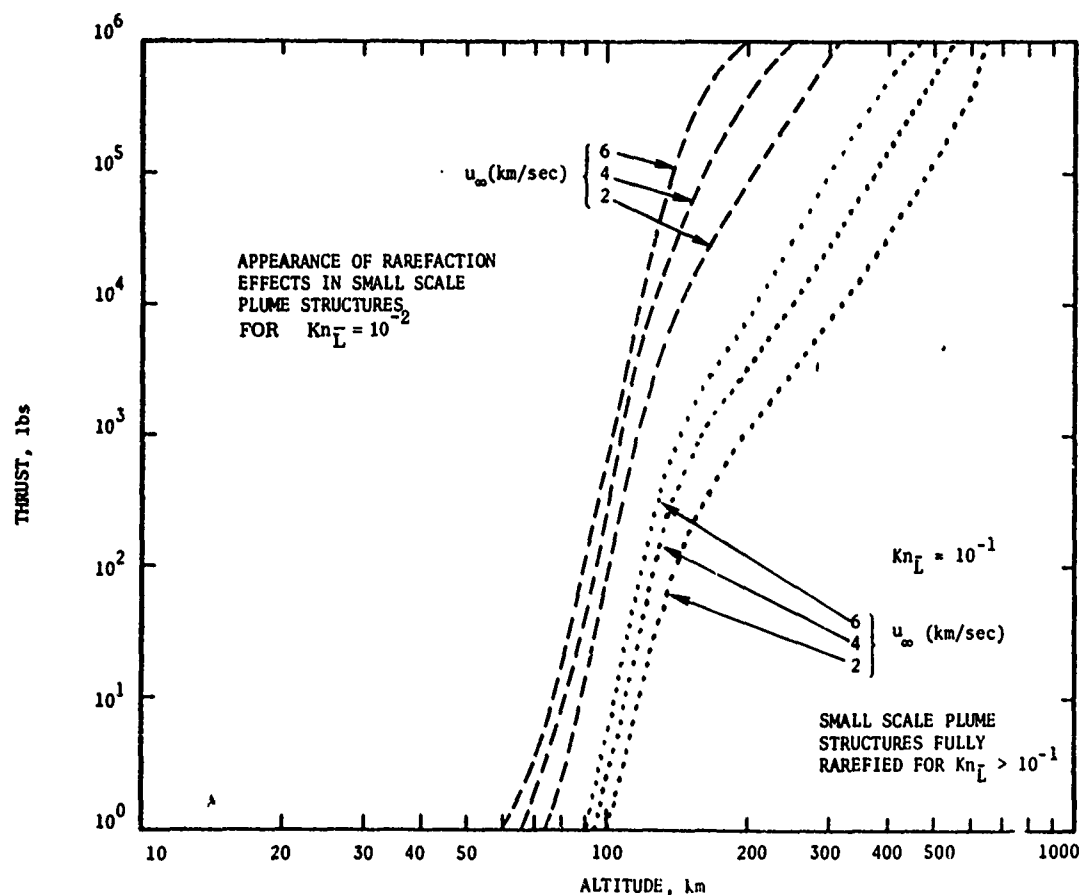


Figure 38. Rarefaction diagram showing velocity dependence for small scale structure rarefaction process.

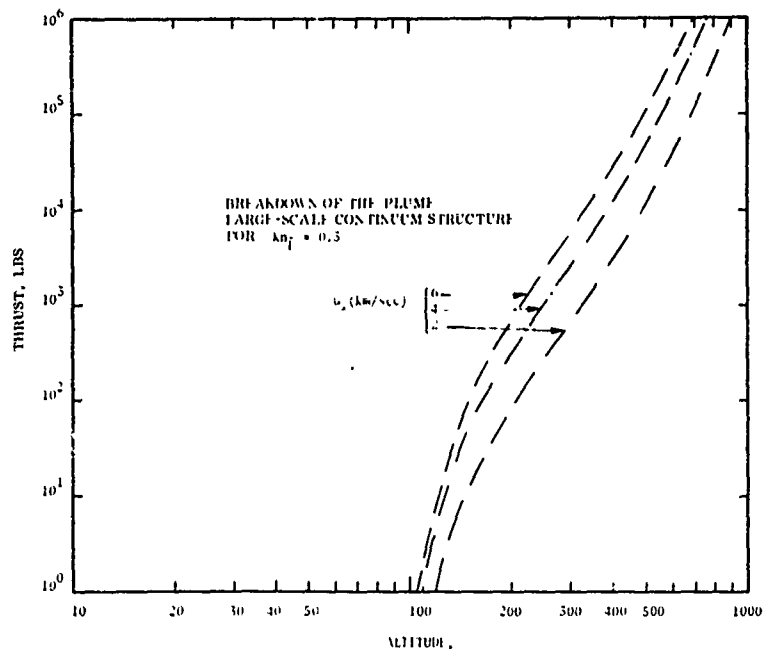
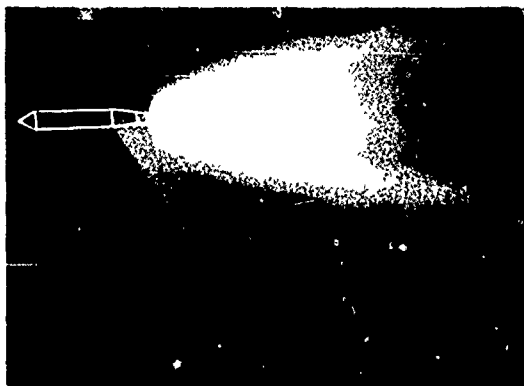


Figure 39. Rarefaction diagram showing the approximate location for rarefaction for the large scale plume structures.

To visually study the appearance of viscous and rarefaction effects we can turn to the electron beam flow visualization photographs and arrange them based on their relative plume Knudsen numbers. In these photographs the model rocket generator is shown by the white outline. The freestream moves parallel to the rocket toward the right at several km/sec. The high pressure jet flow originating from the aft (right-hand end) of the model rocket expands to form the jet freestream interaction region or plume mixing zone shown by the bright region in the electron beam fan.

In the two lower photographs (Figure 40b and 40c) there appears a fairly distinct image of the outer and inner shock layers. In the upper photograph (Figure 40a) is seen only a merged thickened zone that can still be called a mixing layer. The lower flow (40c with the distinct outer and inner shocks and shock layers separated by the somewhat heated mixing layer) corresponds to viscous continuum flow with a plume Knudsen number of $\sim 3.7 \times 10^{-3}$. As the continuum

Reproduced from
best available copy.



TRANSITIONAL FLOW

$$Kn_{\bar{L}} = 1.1 \times 10^{-1}$$

Plume Knudsen Number
Simulation Altitude ~ 320 km
For 60,000 lb Thrust Vehicle

(40a)

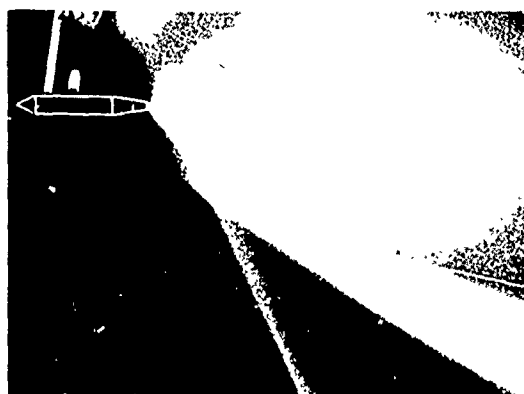


CONTINUUM-TRANSITIONAL BOUNDARY

$$Kn_{\bar{L}} = 1.3 \times 10^{-2}$$

Plume Knudsen Number
Simulation Altitude ~ 170 km
For 60,000 lb Thrust Vehicle

(40b)



VISCOUS-CONTINUUM FLOW

$$Kn_{\bar{L}} = 3.7 \times 10^{-3}$$

Plume Knudsen Number
Simulation Altitude ~ 120 km
For 60,000 lb Thrust Vehicle

(40c)

NOTE: Growth of Hypersonic Scale \bar{L} and Body Size ℓ_m are not Simulated in this Series.

Figure 40. Flow visualization photographs of plume in continuum and transitional flow regimes (n.b. growth of hypersonic scale \bar{L} and body size ℓ_m are not simulated in this photographis series.)

transitional boundary in the region of plume Knudsen number of 10^{-2} is crossed, it is seen(40b) that there are still two shocks which are, however, becoming quite spread out. When transition flow is reached (40a) at a plume Knudsen number of 1×10^{-1} the mixing layer structure, as a compression of jet and freestream species, alone remains.

The full scale missile flight simulated by the plane flows in these photographs is representative of important portions of typical ICBM trajectories. For example, relating these photographs to a rocket of 60,000 lb thrust climbing along a typical trajectory, they would correspond to a series of snapshots of this rocket at 120 km (viscous continuum flow), at 170 km (the continuum-transitional boundary), and 320 km (transitional flow where the small scale flow is fully rarefied). In this simulation series the growth of the plume would require that the upper photograph be enlarged about 45 times and lower photograph while the rocket body size should be reduced by a factor of about 20 to insure it exerts negligible effect on the plume.

5.4 RAREFACTION EFFECTS: SUMMARY

Rarefaction structure scaling effects were observed in the HAPRAP hypersonic plume simulations. The onset of rarefaction has been considered in terms of the ratio of small scale flow dimensions to mean free path, λ_{∞} . It is pointed out that in the "scaling" transitional regime small structures rarefy and vary substantially as λ_{∞} whereas the large structures continue to vary in a continuum flow regime fashion. This double scaling appears in the HAPRAP data in which the most rarefied runs ($Kn_L \sim 10^{-1}$) show the width of the freestream species peak in the mixing layer to be about λ_{∞} whereas the equal concentration surfaces of much larger dimensions still vary as \bar{L} .

It is determined that the plume will be on the continuum-transition regime boundary at $Kn_L \sim 1 \times 10^{-2}$ (for $\bar{x} = 0.5$) and on the transitional-scattering boundary at $Kn_L \sim 0.3$ to 0.5 . From the simulation studies it appears that the HAPRAP data $2 \times 10^{-3} < Kn_L < 1 \times 10^{-1}$ falls in the continuum and transitional regimes which typify much high altitude missile operation. Density regimes

are properly characterized by Kn_L^- for $Kn_L^- < 1 \times 10^{-1}$. For $Kn_L^- > 1 \times 10^{-1}$ Muntz⁽⁷⁰⁾ formulation of plume Knudsen number (Equation (78)) is more suitable. The qualitative results of this section are summarized in Table V.

Because of the requirement to carrying out chemical and excitation process calculations in the transitional plume the question of freestream particle kinetic energy redistribution into a Boltzmann distribution (termed "thermalization") has been considered. It is found that, to the accuracy of the analysis carried out here, that the plume shock layer velocity distribution will exhibit departures from the Boltzmann distribution for $Kn_L^- > 1 \times 10^{-1}$.

The continuum flow theories, which are in question for supplying the plume small details, give the location of this mixing layer through the entire process of rarefaction studied here and thus offer a useful method of estimating the overall scale of the plume throughout these flow regimes (up to $Kn_L^- = 1 \times 10^{-1}$) or to quite high altitudes for ICBM flight. However, if we are interested in radiation/excitation phenomena which strongly depend on the local flow details, such as the particle velocity distribution, then we should take rarefaction effects into account at much lower plume Knudsen numbers altitudes. Certainly by $Kn_L^- = 1 \times 10^{-1}$ the importance of nonthermal effects in these phenomena should be considered for the particular process and/or radiation bandwidth on interest.

TABLE V.

SUMMARY OF HYPERSONIC PLUME FLOW RAREFACTION EFFECTS FOR $M_\infty = 6-10$

$Kn_L = \lambda_\infty / \bar{L}$	Regime	Continuum Formulation	Nonthermal Effects	K_{NP} (Muntz (70))
$< 1 \times 10^{-2}$	continuum	• applicable	nil	not applicable
1×10^{-2} to $- 3 \times 10^{-2}$	continuum- transitional	• applicable for large structures • in some error for small structures and local flow properties	should be evaluated for relative importance	not applicable
3×10^{-2} to $- 1 \times 10^{-1}$	transitional	• in some error for large structures • in large error for small structures and flow properties	significant, must be evaluated	applicability marginal
1×10^{-1} to $- 3 \times 10^{-1}$	transitional-scattering	• in some error for large structures • not applicable to local flow	important	applicable (Kn_L inapplicable)
$> 3 \times 10^{-1}$	scattering	• not applicable	important	applicable (Kn_L inapplicable)

Section VI

SUMMARY AND RECOMMENDATIONS

6.1 SUMMARY

6.1.1 Plume Parameters and the Jarvinen-Hill Plume Model

The present study has reviewed the development of simple, analytic models designed to describe high-altitude coparallel rocket plumes and has assessed their utility based upon analysis of the HAPRAP measurements. The two most important parameters in the description of high-altitude rocket plume structures are

Plume Hypersonic Scale,

$$\bar{L} = \sqrt{\text{Rocket Thrust/Freestream Dynamic Pressure}}$$

Nozzle Thermodynamic Efficiency,

$$C_F/C_{F_{\max}} = \text{Rocket Thrust/Maximum Potential Thrust}$$

An idealized momentum balance applied to the plume relates the nozzle efficiency to the ratio of plume drag to rocket thrust,

$$D/T = C_{F_{\max}}/C_F - 1$$

The simple inviscid flow model which most effectively describes high-altitude, ICBM type plume structures in terms of these parameters is the Jarvinen-Hill⁽¹⁹⁾ model. This model is well suited to analysis of field data and to the design of wind-tunnel and flight experiments.

6.1.2 Applicability of the Jarvinen-Hill Model

A study of the limits of applicability of the Jarvinen-Hill model has indicated the following:

- a. For typical ICBMs the detached plume outer shock assumed in this model can be perturbed by the missile body at altitudes below 100 km and may be seriously disturbed at altitudes below 60 to 70 km. The use of this model at altitudes on the order of 30 km generally appears unwarranted,
- b. For sufficiently large freestream dynamic pressures the plume contact surface becomes rather pointed and the plume outer shock is attached. This violates the assumption implicit in the model of a detached shock. Attached shocks may be expected to occur (for a typical boost phase ICBMs) at altitudes below 70 - 120 km,
- c. A class of high efficiency vehicles is conceivable (with $C_F/C_{F_{\max}} > 0.93$) which will not display a detached plume outer shock at any altitude,
- d. The Jarvinen-Hill scaling of internal jet structure is incorrect in the limit of hypersonic nozzle exit conditions,
- e. This plume model contains no direct information about the viscous phenomena within the high altitude plume structure,
- f. The Jarvinen-Hill model is based on the assumption of strongly hypersonic external flow such that the dynamic pressure term dominates the static pressure term. For typical ICBMs at high altitude (> 120 km), the freestream Mach number is between 6 and 10 and the region of validity for this condition in the plume mixing layer is on the order of within one characteristic length, i.e. \bar{L} , of the missile location. Within the strongly hypersonic exhaust core flow the applicability of this model extends considerably further from the missile, at least $3\bar{L}$, based upon study of the Mach disc locations.

6.1.3 The HAPRAP Flow-Interaction Measurements

Model exhaust plumes in coparellel hypersonic ambient streams were studied by pitot probe surveys, electron-beam flow visualization photographs, and electron-beam concentration surveys of the jet and freestream species in the HAPRAP tests. The present study has shown that, with certain exceptions, the HAPRAP data are quite satisfactory for the study of high-altitude viscous plume behavior. The principal exceptions are (a factor of two) error in the absolute dynamic calibration of jet gas (He) for the tunnel M tests and occurrence of significant image shifts of the plume outer shock in flow visualization photographs, particularly, in the tunnel M tests. On the whole, the HAPRAP measurements are suitable for interpretation of plume behavior in a hypersonic stream. The electron-beam species concentration surveys of the jet-freestream mixing region are of particular importance in the understanding of viscous phenomena in the high altitude plume mixing layer structure.

6.1.4 Simulation of High Altitude Plumes

An evaluation of the HAPRAP wind tunnel plumes was conducted to establish the degree of simulation of high altitude flight conditions. The most important parameter for describing viscous and rarefaction phenomena in high-altitude plume mixing layers is the plume Knudsen number, $Kn_{\bar{L}}$, which is ambient mean free path divided by \bar{L} . Several less important simulation parameters were also considered. It was concluded that

- a. the HAPRAP tests simulated ICBM-class sustainer operation (thrust levels of 10^4 to 10^5 lb) from ~ 120 to 320 km altitude;
- b. these tests simulated smaller engine operation (thrust levels of 10^2 to 10^3 lb) from ~ 80 to 150 km altitude;
- c. the most serious defect in the simulation is caused by the overly-large model rocket bodies.

The overall HAPRAP simulation of high-altitude plumes is quite good and can be improved in future work in existing groundbased facilities principally by reducing the plume generator (model rocket) dimensions.

6.1.5 The Shock Data

Analysis of plume flow field data included examination of the plume outer and inner shocks and the mixing region between jet and ambient gases. The plume outer shocks were significantly disturbed by several effects including overly-long model rocket bodies. The Mach disc locations showed a dependence on D/T in contradiction with the Jarvinen-Hill model. Because of the various disturbances to outer shocks and general weakening the lack of identity of shock structures in the transitional flow regime, the shocks were not analyzed in detail.

6.1.6 The Mixing Layer Structure

The electron beam radial surveys of species concentrations were used to construct a surface of equal concentrations of the jet and freestream species. In the plume mixing layer this surface is easily identifiable even in the transitional flow regime. These surfaces are of interest as they are in the vicinity of a surface of maximum volumetric rates for chemical and excitation processes of a restricted class of reactions involving collisions between the jet and freestream species. This is because these surfaces lie close to the maxima in the transverse profiles of the static temperature and the product of the jet and ambient species concentrations. Specific features of these equal concentration surfaces as seen in the HAPRAP data are:

- a. The locations of these surfaces, for the same value of D/T and ratio of the freestream to jet species masses (m_∞/m_j), lie approximately along a single curve when normalized by \bar{L} ,

- b. For $D/T = 0.135$ and $m_\infty/m_j \approx 1$ the surfaces of equal concentration lie close to the Jarvinen-Hill plume model inviscid contact surfaces for $D/T = 0.135$,
- c. The dependence upon D/T of the locations of these surfaces is in qualitative agreement with the Jarvinen-Hill model,
- d. The surface locations show a strong dependence on m_∞/m_j such that they become broader as m_∞/m_j increases,
- e. Species concentrations along these surfaces are reasonably well correlated by the density normalization of Jarvinen and Hill, however, the magnitudes of these normalized concentrations show a strong dependence on tunnel stagnation temperatures,
- f. Based on a limited amount of data, the local inclination of these surfaces to the freestream, σ_∞ , may be used with the Newtonian pressure coefficient, $2 \sin^2 \sigma_\infty$, to estimate local static pressures along these surfaces.

6.1.7 The Transitional Flow Regime

HAPRAP measurements were made at sufficiently large plume Knudsen numbers to provide information on the initial breakdown of continuum flow. The transitional flow regime was characterized as one in which the large scale structures behaved as though in a continuum fluid while the small scale structures were rarefied or in the process of rarefying. Specifically, the HAPRAP data show the following transitional behavior:

- a. The surfaces of equal concentrations are relatively large (i.e. on the order of \bar{L}) and they display continuum-like behavior over the entire plume Knudsen number range studied ($2 \times 10^{-3} \leq Kn_{\bar{L}} \leq 1 \times 10^{-1}$),

- b. The mixing layer widths (as measured by the compression of free-stream species) are relatively small (i.e. on the order of $\bar{L}/30$) and they begin to depart from continuum-like behavior by $Kn_L^- \sim 10^{-2}$ and proceed to behave in a rarefied flow manner (i.e. to vary directly with freestream mean free path) by $Kn_L^- \sim 10^{-1}$.

It was found that Simons' ⁽⁷¹⁾ continuum flow failure criterion was in approximate agreement with the HAPRAP observations of first breakdown of the continuum flow at $Kn_L^- \sim 1 \times 10^{-2}$ on the small scale of the mixing layer. On the large scale of the entire plume width, the breakdown of the continuum structures was estimated to occur at $Kn_L^- \sim 3 \times 10^{-1}$ in approximate agreement with Muntz' ⁽⁷⁰⁾ criterion for the transitional-scattering regime boundary. The HAPRAP data are applicable to the viscous-continuum and transitional density regimes of plume flow.

An additional aspect of flow rarefaction was explored by investigating the flow conditions in which insufficient collisions occur in the plume nose region to properly redistribute the freestream flow kinetic energy into a thermalized flow with an isotropic Boltzmann velocity distribution. If thermalization is not achieved in the plume flow field, then the use of excitation and chemical production rates based on measurements in gases characterized by isotropic Boltzmann velocity distributions is not warranted. It was found that a thermalization limit criterion could be expressed in terms of plume Knudsen number and that, as a rough estimate, the possibility that thermalization is not achieved must be considered when $Kn_L^- > 1 \times 10^{-2}$. Based on these rarefaction criteria, it was found that, depending upon the missile speed, the altitude above which plume rarefaction effects must be considered is about 140 to 180 kilometers for typical ICBM flight engines (of approximately 10^4 to 10^5 lb thrust) and correspondingly lower altitudes for smaller rocket operation.

6.2 RECOMMENDATIONS

6.2.1 A Plume Nomogram

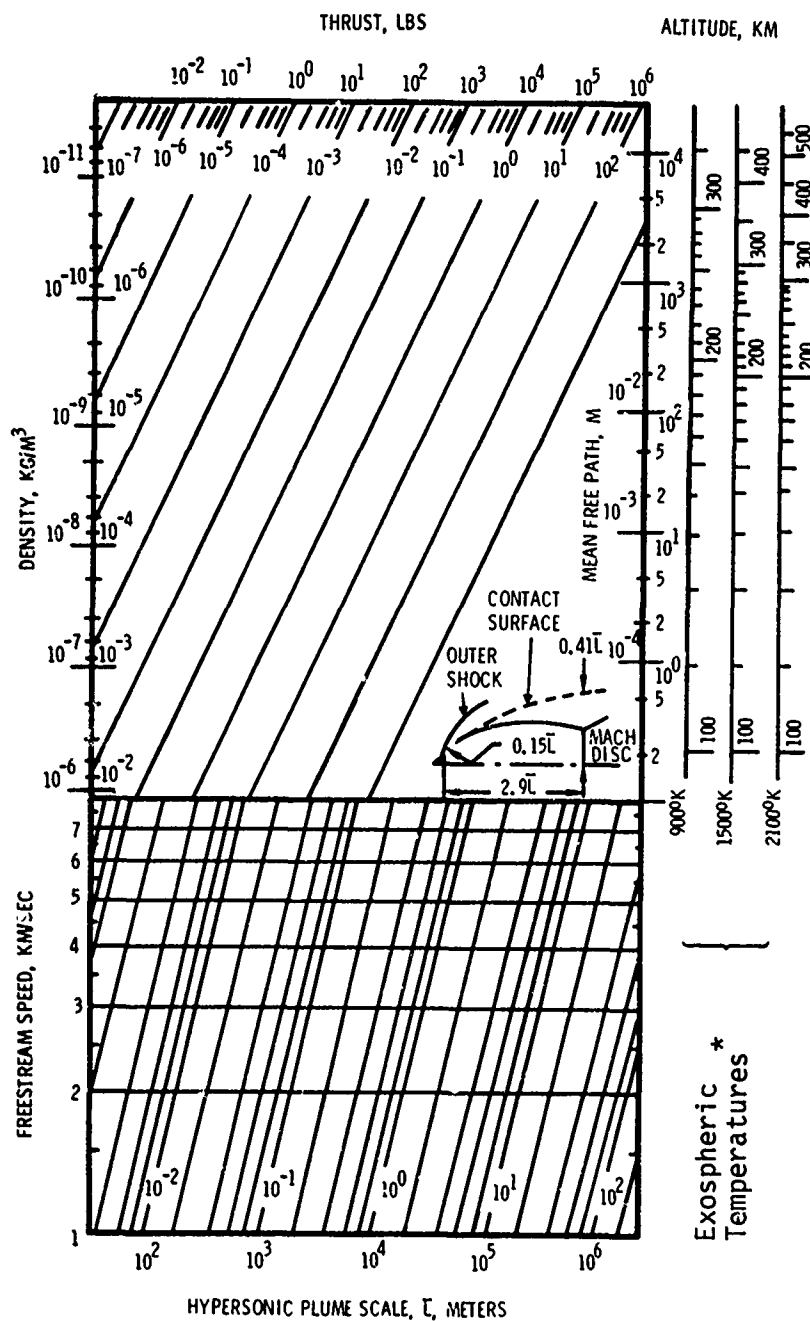
The Jarvinen-Hill model is quite useful in providing plume dimensions for analyzing field data, setting up field measurements, and designing wind tunnel experiments. A simple graphical device for doing such work rapidly is desirable. A nomograph for this purpose, designed by Sutton⁽⁷⁵⁾, has been modified and is shown in Figure 41.

The nomograph is basically a device for calculating the hypersonic scale length, \bar{L} , given that, for the flight vehicle under study, its altitude, thrust, and speed are known. Since the expression for \bar{L} , Equation (1), requires ambient density as an input rather than altitude, the missile altitude must first be related to density through knowledge of the state of the thermosphere (i.e., the atmosphere above 100 km altitude). The thermosphere is strongly affected by the solar radio and geomagnetic activity, and diurnal and semiannual variations. Correlation formulae for estimating the exospheric temperature are given in the U.S. Standard Atmosphere Supplements⁽⁷⁶⁾. These correlation formulae require daily values of the solar flux at 10.7 cm and the geomagnetic planetary index which are available in the Solar-Geophysical Data Prompt and Comprehensive Reports³.

When the exospheric temperature has been estimated, the vertical altitude scales for three different exospheric temperatures on the upper right hand side of Figure 41 can be used to make a best estimate of the atmospheric density at the missile altitude by first interpolating an altitude for the calculated exospheric temperature. This interpolated altitude is then read horizontally across to the exterior density scale markings on the left hand side of the figure. This line also gives the ambient mean freepath on the appropriately labeled exterior scale markings on the right hand side. Notice that the state of the thermosphere, as determined by solar activity, contributes in the first order to the ambient density and so also to the plume dimensions above 300 km altitude.

³These monthly reports are available through the National Geophysical and Solar-Terrestrial Data Center of the National Oceanic and Atmospheric Administration of the U.S. Dept of Commerce, Boulder, Colorado.

⁴Note that the 1962 U.S. Standard Atmosphere exospheric temperature is $\sim 1500^{\circ}\text{K}$.



* Exospheric temperatures from the spring/fall model (30° to 60° N. Lat.) of the U.S. Standard Atmosphere Supplements, 1966.

Figure 41. Nomogram for plume structures.

The missile thrust is entered from the scale exterior to the upper horizontal line of Figure 41. This thrust is read diagonally down toward the left until it intersects the horizontal line just drawn. This is the first intersection. A vertical line is dropped from the first intersection into the lower box of the figure where it intersects a horizontal line labeled on the left hand side with the known missile speed. This is the second intersection. The missile hypersonic plume scale is given by the scale exterior to the lower horizontal line of the figure. The magnitude of the missile plume scale is identified by the diagonal lines nearest the second intersection. Dividing the ambient mean free path by the hypersonic plume scale gives the plume Knudsen number. When done carefully, the results should be accurate to $\pm 10\%$.

The procedure just described can be used to generate a series of points in the lower box, the locus of which shows the history of the plume development. Notice that for full scale missile flight calculations the exterior scale markings are used as just described. For wind tunnel experiment design, different ranges of the variables are used and the same type of calculation procedure is used except that the interior scale markings are used. However, for test limits the nomogram might be used in the reverse manner based on the physical limitations of the uniform wind-tunnel flow region and the amount of mass flow addition from the model which can be accommodated by the tunnel compressors. Accordingly, limiting boundaries of tunnel operation could be laid out on the nomogram and the resulting range in Kn_L , determined.

The proportions of the Jarvinen-Hill analytic model⁽¹⁹⁾ for moderate efficiency engines characterized by blune-noses are shown in Figure 41. These proportions are based on a typical D/T value of 1/6 are,

$$\text{Plume nose radius} = R_s = 0.15\bar{L}$$

$$\text{Contact surface radius at the Mach Disc} = R_b = 0.41\bar{L}$$

$$\text{Distance from missile to Mach Disc} = L_{MD} = 2.9\bar{L}$$

As a sample calculation we determine the hypersonic plume scale for an ICBM with a thrust of 10^5 lb moving at 4 km/second at 180 km altitude in an atmosphere of exospheric temperature 1500°K . A horizontal line is drawn from 180 km on the external right-hand upper scale to make the first intersection with the diagonal thrust line labeled 10^5 lb in the upper box. From this intersection, a vertical line is dropped into the lower box to make the second intersection with the horizontal line indicating a missile speed of 4 km/sec. The hypersonic plume scale is obtained by reading down and to the left along the diagonals to $\bar{L} \sim 8.5$ km. The nose radius is ~ 1.25 km, the contact surface radius at the Mach disc is ~ 4.25 km, and the distance from the missile to the Mach disc is 25.5 km. As $\text{Kn}_{\bar{L}} = 1.3 \times 10^{-2}$, this plume is near the continuum-transitional flow boundary.

6.2.2 The Evaluation of Rarefaction Effects for $\text{Kn}_{\bar{L}} > 1 \times 10^{-2}$

Several plume Knudsen number criteria for estimating when rarefaction effects should be evaluated are recommended. The present analysis indicates that a continuum plume analysis for plume Knudsen number values in excess of 10^{-2} has an increasingly limited validity, particularly for the smaller details of the flow. Continuum prediction of large-scale plume features by continuum formulations should be valid for $\text{Kn}_{\bar{L}} \leq 0.10$ and perhaps up to $\text{Kn}_{\bar{L}} = 0.3$. However for corresponding chemical rate calculations it is necessary to evaluate the importance of nonthermal effects for $\text{Kn}_{\bar{L}} > 1 \times 10^{-2}$. Strong nonthermal effects will make an appearance for $\text{Kn}_{\bar{L}} > 3 \times 10^{-2}$.

6.2.3 Further Development of a Simple High Altitude Mixing Layer Plume Model

The HAPRAP jet-freestream interaction data has allowed exploration of the mixing layer structure well into the transitional flow regime. It has been found that this structure can be usefully (if only partially) specified by an equal concentration surface. It appears that the concentrations along this surface might be expressed as a "universal" curve by a combination of inviscid and viscous parameters, as an extension of the correlation achieved in this work by use of inviscid scaling. The pressures along this surface can be estimated (as demonstrated on the basis of very limited data) through use of Newtonian pressure coefficients.

Then, in principle, it appears feasible to construct a simple, high-altitude plume model which would predict the spatial extent of the equal concentration surface and the mean thermodynamic properties and velocity along this surface for both the viscous continuum and the transitional flow regimes.

It is recommended that investigations be undertaken specifically designed to hasten the development of a simple, viscous, high-altitude plume model. These would include the following tasks:

- a. Theoretical study of the oblique impact of dissimilar (by species), rarefield hypersonic gas streams to establish the effect of parameters, such as mass ratio, on scaling equal concentration surface properties obtained in the wind tunnel to the flight situation,
- b. Exercise of large computer codes capable of handling multispecies diffusion at high altitudes to establish a benchmark set of computer results required for testing model mixing layer behavior,
- c. Exercise of small computer programs capable of calculating only the plume contact surface location for a large range of inviscid conditions to test the variation of this surface with D/T over the range $0.01 < D/T < 2.0$,
- d. Further study of the HAPRAP data to correlate additional features of the transitional flow regime, and to examine the other plume orientations for which there are HAPRAP data. This work should explore mixing layer phenomena to determine to what further extent wind-tunnel testing will be required to verify the resulting model. Final model testing would require:
- e. Selection of a wind-tunnel test matrix to include a broader range of parameters than available from existing data (e.g., jet-to-freestream enthalpy ratio) and a reduction of model rocket disturbances.

By combining the results of the ground-based test program with field observations, it should be possible to adequately test the resulting viscous plume model. In this effort, certain failings of the Jarvinen-Hill model, particularly the scaling of internal shock structure and the exclusion of attached outer shocks for very high-efficiency engines, should be treated. The resultant high-altitude plume model would encompass all engine designs and flight conditions from the inviscid continuum through to the transitional flow regime.

REFERENCES

1. Love, E.S., and Grigsby, C.E., "Some Studies of Axisymmetric Free Jets Exhausting from Sonic and Supersonic Nozzles into Still Air and Supersonic Streams, " RML54L3, 1955.
2. Love, F.S., "An Approximation of the Boundary of a Supersonic Axisymmetric Jet Exhausting into a Supersonic Stream, " JAS, Feb. 1958.
3. Adamson, T.C., Jr., and Nicholls, J.A., "On the Structure of Jets from Highly Underexpanded Nozzles into Still Air, " JAS, 26, 1, Jan. 1959.
4. Latvala, E.K., "Spreading of Rocket Exhaust Jets at High Altitudes, " AEDC AEDC-TR-59-11, June 1959.
5. Love, E.S., Grigsby, C.E., Lee, L.P., and Woodling, M.J., "Experimental and Theoretical Studies of Axisymmetric Free Jets, " NASA TR R-6, 1959.
6. Latvala, E.K., and Anderson, T.P., "Studies of the Spreading of Rocket Exhaust Jets at High Altitudes, " Planetary and Space Science, Vol. 4, pp. 77-91, 1961.
7. Vick, A.R., et al., "Comparisons of Experimental Free-Jet Boundaries with Theoretical Results Obtained with the Method of Characteristics, " NASA TN-D-2327, 1964.
8. Rosenberg, N.W., Hamilton, W.M., Lovell, D.J., and Bang, R.A., "High Altitude Visible Missile Trails(U), " Project Firefly 1960, Volume III: Missile Trail Mechanisms, AFCRL 256 (III), 1961.
9. Thompson, A., and Harshbarger, F., "Some Comments on the Fluid Dynamics of Missile Trails(U), " Project Firefly 1960, Vol. III, Missile Trail Mechanisms, AFCRL 256 (III), 1961.
10. Hill, J.A.F., and Habert, R.H., "Gasdynamics of High-Altitude Missile Trails, " MITHRAS Report MC-61-18-R1, January 1963.
11. Lees, L., "Inviscid Hypersonic Flow Over Blunt-Nosed Slender Bodies, " GALCIT Hypersonic Research Memorandum No. 31.

REFERENCES (Continued)

12. Jarvinen, P.O., and Dyner, H.B., "Rocket Exhaust Plume Dimensions, " Journal of Spacecraft and Rockets, 6, 11, November 1969.
13. Alden, H.L., and Habert, R.H., "Gasdynamics of High Altitude Rocket Plumes, " MITHRAS Report MC-63-80-R1, July 1964.
14. Moran, J.P., "Similarity in High Altitude Jets, " AIAA Journal, 5, 7, July 1967.
15. Albin, F.A., "Approximate Computation of Underexpanded Jet Structure, " AIAA Journal, 3, 8, August 1965.
16. Hubbard, E.W., "Approximate Calculation of Highly Underexpanded Jets, " AIAA Journal, 4, 10, Oct. 1966.
17. Boynton, F.P., "Highly Underexpanded Jet Structure: Exact and Approximate Calculations, " AIAA Journal, 5, 9, Sept. 1967.
18. Thomson, J.A.L., Barthel, J.R., Brainerd, J.J., Janda, R.S., and Schoonover, M.R., "High Altitude Rocket Plume Structure, " General Dynamics, GD/C-DBE65-023, September 1965.
19. Jarvinen, P.O., and Hill, J.A.F., "Universal Model for Underexpanded Rocket Plumes in Hypersonic Flow, " Proceedings of the 12th HANNAF Liquid Propulsion Meeting, 17-19 Nov. 1970, Las Vegas, Nevada.
20. Sibulkin, M., and Gallaher, W.H., "Farfield Approximation for a Nozzle Exhausting into a Vacuum, " AIAA Journal, 1, 6, June 1966.
21. Norman, W., Kinslow, M., and Lewis, J.W., "Experimental Study of Simulated High Altitude Rocket Exhaust Plumes, " AEDC-TR-71-25, July 1971.
22. Lighthill, M.J., "Dynamics of a Dissociating Gas, Part I Equilibrium Flow, " Jour. Fluid Mech., 2, Part 1, p. 2, 1957.
23. 1962 U.S. Standard Atmosphere, Washington, 1962.

REFERENCES (Continued)

24. Ehrlich, C.F., Jr., and Fong, M.C., "Propulsion Effects on Aerodynamic Characteristics of Lifting Reentry Vehicles," Lockheed Missiles and Space Company, Technical Report AFFDL-TR-70-12, March 1970.
25. "Equations, Tables and Charts for Compressible Flow," Ames Research Staff NASA Report 1135, 1953.
26. Plotkin, K.J., and Draper, J.S., "Detachment of the Outer Shock from Underexpanded Rocket Plumes," AIAA Journal, Vol. 10, No. 12, Dec. 1972.
27. Boynton, F.P., "Exhaust Plumes from Nozzles with Wall Boundary Layers," Jour. Spacecraft and Rockets, 5, 10, October 1968.
28. Sedov, L.I., Similarity and Dimensional Methods in Mechanics, Academic Press, New York, 1959.
29. Taylor, G.I., "The Formation of a Blast Wave by a Very Intense Explosion," Proc. Roy. Soc. Ser. A, 201, p. 159, 1950.
30. Van Dyke, M.D., "A Study of Hypersonic Small Disturbance Theory," NACA Rep. 1194, 1954.
31. Vasiliu, J., "Turbulent Mixing of a Rocket Exhaust Jet with a Supersonic Stream Including Chemical Reactions," Jour. Aero. Sci., 29, 1, January 1962.
32. Tannehill, J.C., "Numerical Computation of Intermediate Altitude Rocket Exhaust Plumes, Including Nonequilibrium Chemical Reactions and Diffusion," Ph.D. thesis, 1969, Dept. of Aerospace Engineering, Iowa State Univ., Ames, Iowa.
33. Tannehill, J.C., and Anderson, E.W., "Intermediate Altitude Rocket Exhaust Plumes," AIAA Journal, 8, 10, Oct. 1971.
34. Boynton, F.P., "The MULTIPLE Supersonic Flow Computer Code," Convair Division of General Dynamics Report GD/C-DBE67-003, February 1967.

REFERENCES (Continued)

35. Boynton, F.P., private communication.
36. Hayes, W.D., and Probstein, R.F., Hypersonic Flow Theory, Academic Press, New York, 1959.
37. Smithson, H.K., Price, L.L., and Whitfield, D.L., "Wind Tunnel Testing of Interactions of High Altitude Rocket Plumes with the Free Stream, " AEDC-TR-71-118, July 1971.
38. Price, L.L., Powell, H.M., and Moskalik, R.S., "Species Number Density Measurements in Plume Interactions with Free Stream Using an Electron Beam Technique, " AEDC-TR-71-226, Nov. 1971.
39. Gilles, S.E., and Stewart, J.D., "AFRPL High-Altitude Plume Radiation Program, Part I: Test Plan, " Aerospace Corp. Rept. No. TR-0066 (5360-01)-2, 13 April 1970.
40. Frenkel, J.F., Kinetic Theory of Liquids, Oxford University Press, 1946.
41. Duff, K., "Non-Equilibrium Condensation of Carbon Dioxide in Supersonic Nozzles, " MIT Gas Turbine Laboratory Rept. 84, Jan. 1966.
42. Golomb, D., Good, R.E., Bailey, A.B., Busby, M.R., and Dawbarn, R., "Dimers, Clusters, and Condensation in Free Jets, II, " J. Chem. Phys. Vol. 57, No. 9, 1 Nov. 1972.
43. Beylich, A.E., "Experimental Investigation of Carbon Dioxide Jet Plumes, " Phys. Fluids, 14, 5, May 1971.
44. Thomas, D.D., and Stewart, J.D., "AFRPL High Altitude Plume Radiation Program, Part IV: Pre-Test Vacuum Plume and Flow-Interaction Analyses, " Aerospace Corp. Rept. No. TOR-0172(2366)-1, 12 Jan. 1972.
45. Whitfield, D.L., private communication.
46. Prozan, R.J., "Development of a Method of Characteristics Solution for Supersonic Flow of an Ideal, Frozen, or Equilibrium Reacting Gas Mixture, " TR LMSC/HREC A782535, April 1966.

REFERENCES (Continued)

47. Butler, H.W., "Description of a Digital Computer Program for Nozzle and Plume Analysis by the Method of Characteristics, " TR LMSC, HREC A783573, December 1966.
48. Ratliff, A.W., "Comparisons of Experimental Supersonic Flow Fields with Results Obtained by Using a Method of Characteristics Solution, " TR LMSC/HREC A782592, April 1966.
49. Hill, J.A.F., and Draper, J.S., "Analytical Approximation for the Flow from a Nozzle into a Vacuum, " Jour. Spacecraft and Rockets, 3, 10, Oct. 1966.
50. Ratliff, A.W., Smith, S.D., and Perry, M.M., "Summary Volume, Method of Characteristics Nozzle and Plume Program, " TR LMSC/HREC D162220-1, January 1972.
51. Smith, S.D., and Perry, M.M., "Users Manual Method of Characteristics Plot Program, " TR LMSC/HREC D162220-2, July 1971.
52. Prozan, R.J., "Solution of Nonisoenergetic Supersonic Flows by Method of Characteristics, " TR LMSC/HREC D162220-3.
53. Smith, S.D., and Ratliff, A.W., "Users Manual Variable O/F Ratio Method of Characteristics Program for Nozzle and Plume Analysis, " TR LMSC/HREC D162220-4, June 1971.
54. Seifert, H.S., ed., Space Technology, J. Wiley and Sons, New York, 1959.
55. Lewis, J.W., private communication.
56. Wiese, W.L., Smith, M.W., and Glennon, B.M., Atomic Transition Probabilities, Vol. I, Hydrogen Through Neon, NSRDS-NBS4, 20 May 1966.
57. Heron, S., McWhirter, R.W.P., and Rhoderick, E.H., "Measurements of Lifetimes of Excited States in Helium, " Proc. Roy. Soc., A234, 565, 1956.
58. Holstein, T., "Imprisonment of Resonance Radiation in Gases, II, " Phys. Rev., 83, 6, 15 Sept. 1951.

REFERENCES (Continued)

59. Mitchell, A.G.G., and Zemansky, M.W., Resonance Radiation and Excited Atoms, Cambridge University Press, 1961.
60. Anderson, R., "A Compilation of Measured Lifetimes of Gaseous Diatomic Molecules," Atomic Data 3, 227-240, 1971.
61. Center, R.E., "Plural and Multiple Scattering of Fast Electrons in Gases," AVCO Everett Research Report 329, July 1969.
62. Champion, K.S.W., and Schweinfurth, R.A., "The Mean COSPAR International Reference Atmosphere," presented at 14th COSPAR Meeting, June 1971, Seattle, Wash.
63. Vincenti, W.G., and Kriger, C.H., Jr., Introduction to Physical Gas Dynamics, J. Wiley and Sons, 1965.
64. Lock, R.C., "The Velocity Distribution in the Laminar Boundary Layer Between Parallel Streams," Quar. Jour. Mech. and Appl. Math., 4, Part 1, 1951.
65. Hirshfelder, J.O., Curtiss, C.F., and Bird, R.B., Molecular Theory of Gases and Liquids, J. Wiley and Sons, New York, 1954.
66. Adams, R.C., and Holland, A.C., "Wind Tunnel Investigation of the LID Phenomenon," Mithras Rept. MC65-115-R4, Dec. 1965.
67. Camac, M., "Argon and Nitrogen Shock Thicknesses," AIAA Aerospace Sciences Meeting, Preprint 64-35, New York, New York, 20-22 Jan. 1964.
68. Stupochenko, Ye.V., Losev, S.A., and Osipov, A.I., Relaxation in Shock Waves, Springer-Verlag, New York Inc., 1967.
69. Muntz, E.P., Hamel, B.B., and McGuire, B.L., "Some Characteristics of Exhaust Plume Rarefaction," AIAA Jour., 8, 9, Sept. 1970.
70. Muntz, E.P., "Rarefaction of Very-High-Altitude Plumes with External Flow," Aerodynamics and Propulsion Research Laboratory, The Aerospace Corporation, Rept. No. TR-0172(2240-10)-2, 15 June 1971.

REFERENCES (Concluded)

71. Simons, G., "Rarefaction Effects in High Altitude Rocket Plumes, " AIAA Jour., 10, 3, March 1972.
72. Ahouse, D.R., and Bogdonoff, S.M., "An Experimental Flow Field Study of the Rarefield Blunt Body Problem, " AIAA Paper 69-656, San Francisco, Calif., 1969.
73. Vogenitz, F.W., "Low Density Fluid Mechanics, " in Penetration Systems Studies III, Final Report, TRW Systems Group 18117-6014-R0-00, 31 March 1972.
74. Talbot, L., "Survey of the Shock Structure Problem, " American Rocket Society Jour., 32, 7, July 1962.
75. Sutton, E.A., private communication.
76. U.S. Standard Atmosphere Supplements, 1966, Washington, D.C., 1966.

ACKNOWLEDGMENTS

The authors wish to acknowledge the valuable aid of the following: Dr. Morton Camac of Aerodyne Research for his assistance with the electron beam investigation; Prof. Jack Kerrebrock of the MIT Gas Turbine Laboratory and Dr. Howard Baum of Aerodyne Research for their help with the condensation, simulation, and rarefaction studies; Dr. David L. Whitfield of ARO, Inc., of the Arnold Engineering Development Center for his advice and calculations in connection with nozzle boundary-layer growth and inviscid nozzle flow fields, and for the very useful liaison he established with ARO, Inc; and Messrs. Peter Gregory and John Corcoran of Aerodyne Research in connection with processing the data, carrying out calculations, and preparing the figures.

The authors also wish to express their particular appreciation for the support and cooperation extended by Capt. Samuel B. Thompson, the contract monitor, of the Air Force Rocket Propulsion Laboratory, Edwards, Air Force Base, California.